Addressing Stability Robustness, Period Uncertainties, and Startup of Multiple-Period Repetitive Control for Spacecraft Jitter Mitigation

Edwin S. Ahn

Submitted in partial fulfillment of the
requirements for the degree of
Doctor of Philosophy
in the Graduate School of Arts and Sciences

COLUMBIA UNIVERSITY

2013

ABSTRACT

Addressing Stability Robustness, Period Uncertainties, and Startup of Multiple-Period Repetitive Control for Jitter Mitigation in Spacecraft

Edwin S. Ahn

Repetitive Control (RC) is a relatively new form of control that seeks to converge to zero tracking error when executing a periodic command, or when executing a constant command in the presence of a periodic disturbance. The design makes use of knowledge of the period of the disturbance or command, and makes use of the error observed in the previous period to update the command in the present period. The usual RC approaches address one period, and this means that potentially they can simultaneously address DC or constant error, the fundamental frequency for that period, and all harmonics up to Nyquist frequency. Spacecraft often have multiple sources of periodic excitation. Slight imbalance in reaction wheels used for attitude control creates three disturbance periods. A special RC structure was developed to allow one to address multiple unrelated periods which is referred to as Multiple-Period Repetitive Control (MPRC).

MPRC in practice faces three main challenges for hardware implementation. One is instability due to model errors or parasitic high frequency modes, the second is degradation of the final error level due to period uncertainties or fluctuations, and the third is bad transients due to issues in startup. Regarding these three challenges, the thesis develops a series of methods to enhance the performance of MPRC or to assist in analyzing its performance for mitigating

optical jitter induced by mechanical vibration within the structure of a spacecraft testbed. Experimental analysis of MPRC shows contrasting advantages over existing adaptive control algorithms, such as Filtered-X LMS, Adaptive Model Predictive Control, and Adaptive Basis Method, for mitigating jitter within the transmitting beam of Laser Communication (LaserCom) satellites.

TABLE OF CONTENTS

LIST OF FIGURES

LIST OF TABLES

LIST OF ALGORITHMS

ACKNOWLEDGMENT

"If we knew what it was we were doing, it would not be called research, would it?" - Albert Einstein. This famous quote was pretty much the story of my PhD life. As much as I have been initially determined to pursue a doctoral degree in control engineering, I was without any notion on where my research was heading toward and how it could be accomplished. As for most starters the first step of this endeavor was quite crucial, and yet overwhelming. I consider myself most fortunate to have met my thesis advisor, Professor Richard Longman from Columbia University, who courteously held my hand past through these initial steps by showing me how to evaluate control systems from a researcher's perspective. Professor Longman's generosity continued by introducing me to Professor Brij Agrawal from the Naval Postgraduate School (NPS) where I was able to work with optical beam control systems as a research engineer at the Adaptive Optics Center of Excellence (AOCoE). Professor Agrawal showed me the importance of practicality when it comes to implementing control algorithms in hardware, which is now a valuable asset to my skill set. Professor Jae Jun Kim from NPS greatly aided me in both my professional and personal life at NPS. He essentially played the role of a second thesis advisor. Once again I thank Professor Longman, Agrawal, and Kim for all their continuous efforts for preparing me to be an expert within the professional society. My thanks are given out to the many unmentioned people who have helped me throughout this venture as well. At last I thank my mom and dad for their everlasting love and moral support for their somewhat immature son, and my loving wife, Yujin, who was able to bear with a poor PhD student and raise our daughter, Kate, to be a happy and healthy toddler despite her husband's shortcomings. I love you all.

To my wife,

daughter,

and my parents

CHAPTER 1

INTRODUCTION

1.1 MOTIVATION

The error reduction capabilities of conventional feedback control systems are limited by the bandwidth of the closed-loop frequency response of the system. To illustrate this one can consider the frequency response of a control system and calculate the change in magnitude and the change in phase from command to response. There should be no such change if the bandwidth was to be infinitely high or the feedback system was perfect. Repetitive Control (RC) is a relatively new form of control that seeks to converge to zero tracking error when executing a periodic command, or when executing a constant command in the presence of a periodic disturbance. The RC law looks at the error measured in the previous period and adjusts the command in the present period. In the past three decades, a considerable body of literature has appeared, building theoretical frameworks for the field. While RC theory has flourished in the academic world, it is only recent that they are starting to be used in engineering practice. Some of the reason for this is the need for developing stability robustness to model error, and there are now methods for handling this issue. The main purpose of the proposed research is to acknowledge and address issues related to implementation of Multiple-Period Repetitive Control (MPRC) in hardware under complex disturbance environments such as optical jitter induced by mechanical vibration in spacecraft.

1.2 CONCEPTS OF REPETITIVE CONTROL

Repetitive Control (RC) is a relatively new field within control theory. The usual RC problem handles three situations. The RC modifies a feedback control system with the aim of

converging to zero error: (1) When the objective is to track with zero error a periodic command. (2) Or when the desired output is a constant but there is a periodic disturbance, and then the aim is to cancel the influence of the periodic disturbance and get the desired constant output. (3) Or it aims to get zero tracking error to a periodic command in the presence of a periodic disturbance, both with same period. This latter situation often occurs because the observed disturbance is correlated with commanded periodic trajectory and hence exhibits the same period. In practice, one usually must compromise and ask for zero error up to some chosen frequency cutoff. Any periodic command can be written as a sum of a fundamental frequency and all harmonics up to Nyquist frequency. Anyone who has studied classical control theory knows how to compute the steady state frequency response to each of these frequencies, and knows to expect the amplitude and the phase to be different than that of the command. RC aims to fix these errors in response to commands. And similarly periodic disturbances produces a periodic component to the output, and RC aims to modify the command or the error signal going into the controller such that the effect on the output is minus that of the effect of the disturbance.

1.3 LITERATURE REVIEW

People often cite T. Inoue, Nakano, and Iwai [1] at the beginning of the 1980's as originating the field of RC, and these publications were motivated by the desire to eliminate ripple in rectified voltage running magnets in a particle accelerator. Early papers in the field include Hara, Yamamoto, and Omata, [3], [4], and Tomizuka [5], [6] with research towards applications in tracking within hard disk drives. Motivated by robotics, Middleton, Goodwin, and Longman [2] submitted in 1984 with independent development in RC. References [8], [9] give a general overview of RC.

CHAPTER 2

MATHEMATICAL DEVELOPMENT OF VARIOUS TYPES OF REPETITIVE CONTROL ALGORITHMS

2.1 INTRODUCTION

Repetitive control (RC) is a relatively new form of control that seeks to converge to zero tracking error when executing a periodic command, or when executing a constant command in the presence of a periodic disturbance [1-8]. The designs make use of knowledge of the period of the disturbance or command, and makes use of the error observed in the previous period to update the command in the present period. The usual repetitive control approaches address one period, and this means that potentially they can simultaneously address DC or constant error, the fundamental frequency for that period, and all harmonics up to Nyquist frequency. Motivated by the problem of isolating fine pointing equipment on spacecraft from one dominant disturbance source such as a momentum wheel or a cryogenic pump, Reference [9] developed a theory for RC for multiple-input, multiple-output systems. Competing methods for active vibration isolation on spacecraft include the methods of Reference [10], the multiple error LMS algorithm of References [11] and [12], and the matched basis function RC of Reference [13]. Unlike the usual RC design, all of these methods require that the fundamental and each harmonic be addressed individually.

Reference [8] presents the author's preferred approach to designing RC systems. This requires the de-sign of a compensator according to Reference [14] or [15], the design of a zero-phase low-pass filter for stability robustness using the methods of Reference [16] or [17], and the design of an interpolator using Reference [18].

Spacecraft often have multiple sources of periodic excitation. Slight imbalance in reaction wheels used for attitude control creates three disturbance periods. Slight imbalance in control moment gyros introduces four disturbance periods. And these periods might be in addition to a cryogenic pump. References [19] and [20] develop a special repetitive control structure that allows one to address multiple unrelated periods. References [21] and [22] further develop the approach making use of the preferred design approach described above.

Period uncertainties or fluctuations can degrade the error rejection performance of typical RC. Reference [23] addresses this issue by looking multiple periods back at the error history, and was studied in detail by two different approaches in [24, 25].

2.2 BASIC FORM REPETITIVE CONTROL

This section gives a quick presentation of the design process for single period repetitive control favored by the authors and detailed in Reference [8] and references therein. The presentation here is tailored to elucidate the parallel structures of the multiple period repetitive control results presented in later sections. The block diagram for the RC system is given in Figure 2-1 where $G(z)$ represents a closed loop transfer function of a feedback control system, and $R(z)F(z)$ represents the repetitive controller that examines the error $E(z)$ and adjusts the command to the feedback controller. The $Y_D(z)$ is the desired output given as a command to the RC system. Feedback control systems can be subject to deterministic disturbances that enter somewhere around the feedback loop. But wherever they occur there is an equivalent disturbance to the output of the feedback control system, and this is represented by $V(z)$. For single period RC, both $Y_D(z)$ and $V(z)$ are considered periodic with the same period. Initially this period is considered to be p time steps, where p is an integer, and later interpolation is used to handle situations where it is not an integer.

The simplest form of the repetitive control law is written in the time domain in terms of time steps *k*, then in the *z*-transform domain, and finally as a *z*-transfer function as

$$u(k) = u(k-p) + \phi e(k-p+1)$$

$$U(z) = z^{-p}[u(z) + \phi z E(z)] \tag{2.1}$$

$$U(z) = [\phi z / (z^p - 1)]E(z)$$

In words this RC law says, if one period back the output was for example 2 units too low, add 2 units times a gain ϕ to the command at the current step. The +1 time step in the error is introduced assuming that there is a one time step delay from change in command to the first time step a resulting change in the output is observed. The logic of this RC law is appealing, but it is too simple.

2.2.1 General RC Law

Many feedback control systems can exhibit a 180 deg phase lag from command to response at some frequency. If the 2 unit error above was a sample of a signal at this frequency, the phase lag would have the effect of changing the sign on the resulting change in the output, resulting in increasing the error. Hence we introduce a compensator $R(z)$ whose main purpose is to adjust the phase of the error signal in anticipation of the phase lag it will experience going through the system. Also, at high frequencies it is difficult to have a good model, and hence we introduce a zero-phase low-pass filter $H(z)$ whose purpose is to stop learning above some frequency cutoff for which the model error is sufficiently large that one cannot successfully learn. Finally, because the number of time steps in a period may not be an integer number, we introduce $I(z)$ that can be a linear or cubic interpolation between data taken at time steps in order to compute the signal

between time steps at the desired time in the previous period. The resulting RC law can be written as

$$U(z) = H(z)I(z)z^{-p}[U(z) + \phi F(z)E(z)] \tag{2.2}$$

$$U(z) = [\phi H(z)I(z)/(z^p - H(z)I(z))]F(z)E(z) = [R(z)F(z)]E(z) \tag{2.3}$$

$$R(z) = [\phi H(z)I(z)/(z^p - H(z)I(z))] \tag{2.4}$$

2.2.2 Difference Equation for the Error

The $G(z)$ in the block diagram is the true world feedback control system transfer function. For convenience, we define $\bar{G}(z) = F(z)G(z)$. When our model of the feedback control system is used instead of the true world model we will denote the corresponding product by $\hat{G}(z)$. From Figure 2-1, the error satisfies the following equation that can be considered a difference equation when converted back to the time domain

$$[1 + R(z)\bar{G}(z)]E(z) = Y_D(z) - V(z) \tag{2.5}$$

$$[z^p - H(z)I(z)(1 - \phi\bar{G}(z))]E(z) = [z^p - H(z)I(z)][Y_D(z) - V(z)] \tag{2.6}$$

2.2.3 The Design Process

The $H(z)$ filter is likely to be designed after observing behavior of the hardware implementation. The cutoff is based on what is wrong with our model and we do not know this in the design stage. We also do not want a design that is very specialized to exactly one period, so we ignore the interpolator $I(z)$ in the initial design stage. We note that it behaves as a low pass filter, so ignoring it does not cause trouble. Also we will make an optimized design for the

compensator $F(z)$ which makes an optimized choice of the DC gain, and hence we will usually set the gain ϕ to unity. Then the right hand side of Eq. (2.6) has $z^p - 1$ operating on the command and disturbance which are of period *p* time steps. This makes the right hand side zero, forming an homogeneous equation. And the characteristic equation of the homogeneous equation is $[z^p - (1 - \bar{G}(z))] = 0$. This equation suggests that we would like to pick the compensator $F(z)$ to be equal to $G^{-1}(z)$, but this is usually not possible because the inverse of most *z*-transfer functions is unstable. Instead we design $F(z)$ to look like the inverse of the steady state frequency response of the system. The connection between this objective and stability is seen below. Thus, we pick it as an FIR filter that minimizes a cost function *J*

$$F(z) = a_1 z^{m-1} + a_2 z^{m-2} + \cdots + a_m z^0 + \cdots a_{n-1} z^{-(n-m-1)} + a_n z^{-(n-m)} \tag{2.7}$$

$$J = \sum_{j=0}^{N} [1 - G(e^{i\omega_j T}) F(e^{i\omega_j T})][1 - G(e^{i\omega_j T}) F(e^{i\omega_j T})]^* + V(a_1^2 + a_2^2 + \cdots + a_n^2) \tag{2.8}$$

Normally *V* is set to zero. It can be used to prevent the gains from becoming too large and alternating in sign. The summation is taken over a suitably chosen set of frequencies between zero and Nyquist, and superscript asterisk indicates complex conjugation. The resulting design can be very effective. For the third order system used below for numerical examples, use of 12 gains made a $\hat{G}(z)$ that differs from unity only in the 3rd decimal place as shown in References [14] and [8]. Design of $H(z)$ is similar as an FIR filter with $a_k = a_{-k}$ and minimizing J_H

$$H(z) = \sum_{k=-n}^{n} a_k z^k \tag{2.9}$$

$$J_H = \alpha \sum_{j=0}^{j_p} [1 - H(e^{i\omega_j T})][1 - H(e^{i\omega_j T})]^* + \sum_{j=j_s}^{N-1} [H(e^{i\omega_j T})][H(e^{i\omega_j T})]^* \tag{2.10}$$

The first summation is over the passband and the second over the stopband, perhaps with a transition band gap between them. A first order interpolator takes to form $I(z) = az + (1-a)$ when p is chosen as the nearest integer larger than the true period.

2.2.4 Characteristic Polynomial

The characteristic polynomial can be very high degree since it is greater than the number of time steps in a period. If it is not too large, one can determine stability by finding the roots. After clearing fractions, they are the roots of the numerator of

$$1 + R(z)\bar{G}(z) = 0 \tag{2.11}$$

2.2.5 Nonstandard Nyquist Criterion for Stability

Normally one sets the open loop transfer function to -1 when applying the Nyquist stability criterion, i.e. $R(z)\bar{G}(z) = -1$. However, the Nyquist contour for a digital system must go around the unit circle, and at least when $H(z)I(z)$ are not included there are p roots on this contour, and the contour must be modified to go around every such root. This is not practical. References [7] and [8] modify the approach to avoid the problem. The characteristic equation can be rewritten in the form

$$z^{-p} H(z) I(z)[\phi \bar{G}(z) - 1] = -1 \tag{2.12}$$

$$A_1(z) H(z) I(z)[\phi \bar{G}(z) - 1] = -1 \tag{2.13}$$

$$P_1(z) = -1 \tag{2.14}$$

The $A_1(z) = z^{-p}$ is introduced for comparison to multiple period RC results below. There are more poles than zeros in $P_1(z)$ if one does not make the FIR filters too large for the given value of p (and if this is a problem, one can use $2p$ in place of p). Hence, one only needs to let z go around the unit circle. If the resulting plot of $P_1(z)$ does not encircle the point -1, then the RC system is asymptotically stable. This is a necessary and sufficient condition for asymptotic stability for a given value of period p.

2.2.6 Sufficient Conditions for Asymptotic Stability

If the magnitude of the left hand side of Eq. (2.12) is always smaller than one in magnitude as z goes around the unit circle, then the image of the Nyquist contour cannot encircle the point -1 and therefore this is a sufficient condition for asymptotic stability

$$\left|A_1(z)H(z)I(z)[\phi\bar{G}(z)-1]\right| = \left|H(z)I(z)[\phi\bar{G}(z)-1]\right| < 1 \ \forall \ z = e^{i\omega T} \tag{2.15}$$

This is only a sufficient condition, but for the single period case it is usually very close to the necessary and sufficient condition boundary, because p is likely to be a large number. And if inequality (2.15) is violated at some frequency, then the z^{-p} term will spin the phase of that point and very likely make the point -1 encircled in the image of the Nyquist contour used in Eq. (2.14). Unfortunately, the analogous condition for multiple periods will not have this property. During the design process one will aim to satisfy the condition

$$\left|\phi\bar{G}(z)-1\right| < 1 \ \forall \ z = e^{i\omega T} \tag{2.16}$$

If one ensures this condition is satisfied, then re-introducing the interpolator $I(z)$ will not cause trouble because it is a low pass filter with magnitude less than or equal to one. And one can ensure that the zero-phase low-pass filter $H(z)$ does not amplify using Reference [17]. Of course in design one can only aim to satisfy Eq. (2.16) using one's model. Hence, when one applies the resulting control law to the real world, model error can make the condition violated. Based on data one can then tune the cutoff so that the $H(z)$ attenuates enough that the inequality (2.15) is satisfied.

2.2.7 Necessary and Sufficient Conditions for Asymptotic Stability for All Possible Periods

As noted above, if inequality (2.15) is violated for some frequency, then there will always be a value of p for which the z^{-p} in Eq. (2.12) will make the point -1 encircled. Therefore, Eq. (2.15) can also be considered as a necessary and sufficient condition for asymptotic stability for all possible periods p. Furthermore, in the design process when one sets $H(z)I(z)=1$, then inequality (2.16) is a necessary and sufficient condition for asymptotic stability for all possible periods.

2.2.8 Heuristic Monotonic Decay Condition

Stability is a property of the homogeneous equation. Setting the forcing function to zero, one can rewrite Eq. (2.6) as

$$z^p E(z) = [H(z)I(z)(1-\phi\bar{G}(z))]E(z) \tag{2.17}$$

This thinking is heuristic, but the square bracket term appears to be a transfer function from the error in one period to the error in the next period. And in that case, satisfying the inequality in Eq. (2.15) implies that every frequency component of the error will decay every period.

2.2.9 The Design Process

Normally one sets $\phi = 1$, and replaces $H(z)I(z)$ by unity. Then using one's model of $G(z)$ one seeks to design $F(z)$ to satisfy

$$\left|\hat{G}(z) - 1\right| < 1 \;\forall\;\; z = e^{i\omega T} \tag{2.18}$$

Introducing $H(z)$ and $I(z)$ will only help in the sense that they are low pass filters (using the $H(z)$ design method of Reference [17] ensures that its magnitude never exceeds unity). Then one can examine how much model error $\Delta\hat{G}(z)$ one can tolerate and still have stability, by examining the inequality

$$\left|\hat{G}(z) + \Delta\hat{G}(z) - 1\right| = \left|\hat{G}(z) + (\overline{G}(z) - \hat{G}(z)) - 1\right| < 1 \;\forall\;\; z = e^{i\omega T} \tag{2.19}$$

2.3 THREE-PERIOD REPETITIVE CONTROL

This section develops the analogous theory for repetitive control that deals with three periods simultaneously. By doing so we make it obvious how to generalize to any number of periods. The next section treats two independent periods and most of the numerical examples deal with this case. Figure 2-2 gives the structure of the repetitive controller following References [19, 20, 21]. We now need a separate $R_j(z)$ as in Eq. (2.4) for each period p_j. We can allow a different gain ϕ_j for each period. The zero-phase low-pass filter should use the same cutoff for each

period, but the interpolator will be different for each period, and for simplicity we use the notation $H_j(z) = H(z)I_j(z)$. Then

$$R_j(z) = \frac{\phi_j H_j(z)}{z^{p_j} - H_j(z)} \tag{2.20}$$

2.3.1 General RC Law for Three Periods

From the block diagram the transfer function of the RC controller analogous to Eq. (2.3) is given by

$$U(z) = [\hat{R}(z)F(z)]E(z) \tag{2.21}$$

$$\hat{R}(z) = [(R_1 + R_2 + R_3) + (R_1R_2 + R_2R_3 + R_3R_1)\hat{G}(z) + R_1R_2R_3\hat{G}^2(z)] \tag{2.22}$$

As in the single period case, the $F(z)$ is designed making use of our model of the world in $\hat{G}(z)$. But this time $\hat{R}(z)$ is an explicit function of $\hat{G}(z)$. It will be convenient to also define

$$\overline{R}(z) = [(R_1 + R_2 + R_3) + (R_1R_2 + R_2R_3 + R_3R_1)\overline{G}(z) + R_1R_2R_3\overline{G}^2(z)] \tag{2.23}$$

2.3.2 The Difference Equation for the Error Time History When There is no Model Error

The design process must use our model, and hence the design proceeds based on assuming that $\overline{G}(z) = \hat{G}(z)$. Analogous to Eq. (2.5) we then have

$$[1 + \hat{R}(z)\hat{G}(z)]E(z) = Y_D(z) - V(z) \tag{2.24}$$

2.3.3 The Design Process

The numerator of the square bracket term gives the characteristic polynomial, and this bracket term can be factored as follows

$$[1+\hat{R}(z)\hat{G}(z)] = 1+(R_1+R_2+R_3)\hat{G}(z)+(R_1R_2+R_2R_3+R_3R_1)\hat{G}^2(z)+R_1R_2R_3\hat{G}^3(z)$$
$$= [1+R_1\hat{G}(z)][1+R_2\hat{G}(z)][1+R_3\hat{G}(z)] \tag{2.25}$$

Because of the special structure of the RC in Figure 2-2, introduced in References [19] and [20], the characteristic polynomial for three periods is just the product of the characteristic polynomials for independent RC designs made for single periods. Hence, one can design $F(z), H(z), I_j(z)$ (and set $\phi_j = 1$ to use the gain that is optimized when finding $F(z)$ from Eq. (2.8)) independently for each period, and then combine the results as in Eq. (2.22) to create the multi-period repetitive controller.

2.3.4 The Characteristic Polynomial

Allowing for error in our model compared to the real world behavior, the characteristic polynomial is the numerator of the term in square brackets in the following equations, and this is rewritten in forms that show dependence on model error

$$[1+\hat{R}(z)\overline{G}(z)]E(z) = Y_D(z)-V(z)$$

$$[(1+R_1\overline{G}(z))(1+R_2\overline{G}(z))(1+R_3\overline{G}(z))+(\hat{R}(z)-\overline{R}(z))\overline{G}(z)]E(z) = Y_D(z)-V(z)$$

$$[(1+R_1\overline{G})(1+R_2\overline{G})(1+R_3\overline{G})+(R_1R_2+R_2R_3+R_3R_1)\overline{G}(\hat{G}-\overline{G})+R_1R_2R_3\overline{G}(\hat{G}^2-\overline{G}^2)]E = Y_D-V \tag{2.26}$$

The design using Eq. (2.25) will not place the roots quite where they were intended because of the difference between $\hat{G}(z)$ and $\overline{G}(z)$, so the first 3 terms in the square brackets in the last two

equations do not have the roots quite where the design intended. But the remaining terms in the square brackets represent a new way in which model error will disturb the root locations we design. And it will be seen that this reduces the robustness to model error when one goes from one period to multiple periods.

2.3.5 The Difference Equation for the Error Time History When There is Model Error

Substitute $\hat{R}(z)$ into the first of equations (2.26). Then multiply by three factors that appear in its denominator to obtain

$$(z^{p_1}-H_1)(z^{p_2}-H_2)(z^{p_3}-H_3)[1+\hat{R}\overline{G}]E=(z^{p_1}-H_1)(z^{p_2}-H_2)(z^{p_3}-H_3)[Y_D-V] \tag{2.27}$$

$$[z^{p_1+p_2+p_3}+(A+B+C+D)]E=(z^{p_1}-H_1)(z^{p_2}-H_2)(z^{p_3}-H_3)[Y_D-V] \tag{2.28}$$

$$\begin{aligned}
A&=[\phi_1H_1(z^{p_2}-H_2)(z^{p_3}-H_3)+\phi_2H_2(z^{p_3}-H_3)(z^{p_1}-H_1)+\phi_3H_3(z^{p_1}-H_1)(z^{p_2}-H_2)]\overline{G}\\
B&=[\phi_1H_1\phi_2H_2(z^{p_3}-H_3)+\phi_2H_2\phi_3H_3(z^{p_1}-H_1)+\phi_3H_3\phi_1H_1(z^{p_2}-H_2)]\hat{G}\overline{G}\\
C&=[\phi_1H_1\phi_2H_2\phi_3H_3]\hat{G}^2\overline{G}\\
D&=-(z^{p_1+p_2}H_3+z^{p_2+p_3}H_1+z^{p_3+p_1}H_2)+(z^{p_1}H_2H_3+z^{p_2}H_3H_1+z^{p_2}H_1H_2)-H_1H_2H_3
\end{aligned} \tag{2.29}$$

When there is no cutoff filter and there is no interpolation, and the command and disturbance are periodic with the prescribed periods, the right hand side of the difference equation is zero, making a homogeneous difference equation for the error. Otherwise, there is a forcing function, and a particular solution response. But stability and decay of the error is governed by the homogeneous equation.

2.3.6 The Heuristic Monotonic Decay Condition for the Error for Three Periods

Decay of the error (and asymptotic stability) is a property of the homogeneous difference equation. Setting the right hand side to zero, one can write the homogeneous difference equation in the form

$$z^{p_1+p_2+p_3}E = [A+B+C+D]E \tag{2.30}$$

The square bracket term on the right appears to be a transfer function from the error in the current "period" to the error in the next "period", where the period involved is now $p_1 + p_2 + p_3$. This suggests that if the magnitude frequency response of the square bracket term is less than unity for all frequencies up to Nyquist, then every frequency component of the error will decay every period. This thinking is heuristic. See Reference [8] for a discussion of the assumptions and a discussion of how accurately it predicts the decay for the one period case.

2.3.7 Nonstandard Nyquist Criterion for Stability

As in the single period RC case, one cannot easily directly apply Nyquist criterion using the open loop transfer function $\hat{R}(z)\overline{G}(z) = -1$. In the case when the $H_j(z) = 1$, there would be $p_1 + p_2 + p_3$ roots on the unit circle, and one would have to modify the Nyquist contour to go around every one of them in order to make stability conclusions. But the above development has rearranged the characteristic polynomial into a form for which this problem is gone. We can write this polynomial in the form

$$\begin{gathered} z^{-(p_1+p_2+p_3)}[A+B+C+D] = -1 \\ P_3(z) = -1 \end{gathered} \tag{2.31}$$

Given the periods, a necessary and sufficient condition for asymptotic stability of the three period repetitive control design is that the $P_3(z)$ image of the unit circle $z = e^{i\omega T}$ not encircle the point -1. Note that every term in $[A + B + C + D]$ is at least linear in the cutoff filter $H(z)$. Therefore, just as in the single period case, we can produce stability by introducing such a cutoff of the learning process. Of course we pay for this stability by no longer addressing the periodic error components about the cutoff frequency.

2.3.8 A Sufficient Condition for Asymptotic Stability

If the square bracket term has magnitude less than unity for all frequencies, then the plot cannot encircle the point -1

$$\left|A(z) + B(z) + C(z) + D(z)\right| < 1 \ \ \forall \ z = e^{i\omega T} \tag{2.32}$$

2.3.9 A Specialized Sufficient Condition for Asymptotic Stability

Consider the usual problem during the design process where we consider the $H_j(z)$ to be unity. Also consider that the design of the compensator aims to produce a good approximation of the inverse of the frequency response using Eq. (2.8). Recall that this approximation can often be very good, so let us consider that the result is to create a $\hat{G}(z) \approx 1$. Then Eq. (2.31) becomes

$$P_3(z) = A_3(z)(\bar{G}(z) - 1) = -1 \tag{2.33}$$

$$A_3(z) = (z^{-p_1} + z^{-p_2} + z^{-p_3}) - (z^{-(p_1+p_2)} + z^{-(p_2+p_3)} + z^{-(p_3+p_1)}) + z^{-(p_1+p_2+p_3)} \tag{2.34}$$

This is a specialized Nyquist criterion for the three period case analogous to Eq. (2.13). In the one period case it was easy to find a necessary and sufficient condition for stability for all possible periods, Eq. (2.16). The three period case is more complicated.

2.3.10 A Specialized Sufficient Condition for Stability for All Possible Periods

But Eq. (2.33) suggests a sufficient condition that

$$\left|\overline{G}(z)-1\right|<1/\max_{w,p_1,p_2,p_3}\left|A_3(e^{iwT})\right| \;\forall\; z=e^{i\omega T} \tag{2.35}$$

The maximization will produce a number that cannot be larger than 9 which corresponds to succeeding in making every term equal +1. But it is clear that one will have to restrict the magnitude of $\overline{G}(z)-1$ to be much less than unity in order to guarantee stability for all possible period, whereas in the single period case keeping it less than unity was sufficient.

2.4 TWO-PERIOD REPETITIVE CONTROL

This section presents the RC for the two period case which will be used for numerical investigations in a later section. Sometimes it is clear how to make the reduction from three to two periods, but it is not always obvious. The two period versions of equations (2.21) through (2.30) are as follows:

$$U(z)=[\hat{R}^*(z)F(z)]E(z) \tag{2.36}$$

$$\hat{R}^*(z)=[R_1+R_2+R_1R_2\hat{G}(z)] \tag{2.37}$$

$$\overline{R}^*(z)=[R_1+R_2+R_1R_2\overline{G}(z)] \tag{2.38}$$

$$[1+\hat{R}^*(z)\hat{G}(z)]E(z)=Y_D(z)-V(z) \tag{2.39}$$

$$[1+\hat{R}^*(z)\hat{G}(z)] = 1+(R_1+R_2)\hat{G}(z)+R_1R_2\hat{G}^2(z) = [1+R_1\hat{G}(z)][1+R_2\hat{G}(z)] \tag{2.40}$$

$$[1+\hat{R}^*(z)\overline{G}(z)]E(z) = Y_D(z)-V(z)$$

$$[(1+R_1\overline{G}(z))(1+R_2\overline{G}(z))+(\hat{R}(z)-\overline{R}(z))\overline{G}(z)]E(z) = Y_D(z)-V(z) \tag{2.41}$$

$$[(1+R_1\overline{G})(1+R_2\overline{G})+R_1R_2\overline{G}(\hat{G}-\overline{G})]E = Y_D-V$$

$$(z^{p_1}-H_1)(z^{p_2}-H_2)[1+\hat{R}^*\overline{G}]E = (z^{p_1}-H_1)(z^{p_2}-H_2)[Y_D-V] \tag{2.42}$$

$$[z^{p_1+p_2}+(A^*+C^*+D^*)]E = (z^{p_1}-H_1)(z^{p_2}-H_2)[Y_D-V] \tag{2.43}$$

$$A^* = [\phi_1H_1(z^{p_2}-H_2)+\phi_2H_2(z^{p_1}-H_1)]\overline{G}$$

$$C^* = [\phi_1H_1\phi_2H_2]\hat{G}\overline{G} \tag{2.44}$$

$$D^* = -z^{p_2}H_1-z^{p_1}H_2+H_1H_2$$

$$z^{p_1+p_2}E = [A^*+C^*+D^*]E \tag{2.45}$$

2.4.1 Nonstandard if and only if Nyquist Criterion for Stability

The two period RC law Eq. (2.36) produces an asymptotically stable repetitive control system if and only if the plot of

$$z^{-(p_1+p_2)}[A^*+C^*+D^*] = -1$$

$$P_2(z) = -1 \tag{2.46}$$

as $z = e^{i\omega T}$ goes around the unit circle, does not encircle the point -1. If one sets $H_j = 1$ as one normally does in the design process, Eq. (2.46) can be written as

$$P_2(z) = (z^{-p_1} + z^{-p_2})[\phi\bar{G}(z) - 1] - (z^{-(p_1+p_2)})\{2[\phi\bar{G}(z) - 1] - [\phi^2\hat{G}(z)\bar{G}(z) - 1]\} = -1 \tag{2.47}$$

It can also be written as

$$P_2(z) = \hat{A}_2(z)[\phi\bar{G}(z) - 1] = -1 \tag{2.48}$$

$$\hat{A}_2(z) = \left\{ A_2(z) + (z^{-p_1} + z^{-p_2}) \left[\phi^2 \left(\frac{\hat{G}(z)\bar{G}(z) - 1}{\phi\bar{G}(z) - 1} \right) - 1 \right] \right\} \tag{2.49}$$

$$A_2(z) = z^{-p_1} + z^{-p_2} - z^{-(p_1+p_2)} = z^{-p_1}[1 + z^{-(p_2-p_1)} - z^{-p_2}] \tag{2.50}$$

2.4.2 Sufficient Conditions for Stability for All Possible Periods

The large powers of z involved in the stability conditions creates difficulty performing numerical evaluations. One can create a sufficient condition for stability that is independent of the periods by asking that for the $P_2(z)$ in Eq. (2.47), $|P_2(z)| < 1 \forall z = e^{i\omega T}$, and then using the triangle inequality on the two terms. This results in the sufficient condition

$$2|\phi\bar{G}(z) - 1| + |2[\phi\bar{G}(z) - 1] - [\phi^2\hat{G}(z)\bar{G}(z) - 1]| < 1 \forall z = e^{i\omega T} \tag{2.51}$$

One can specialize further to the case where $F(z)$ has been designed by the optimization in Eq. (2.8) using $V = 0$, and done with enough gains in $F(z)$ that we can consider that $\hat{G}(z) = 1$, and that we use the gain obtained by the optimization so that ϕ is set to unity. The sufficient condition becomes

$$3\left|\bar{G}(z)-1\right|<1\,\forall\, z=e^{i\omega T} \tag{2.52}$$

Comparing to Eq. (2.16) with $\phi=1$, we see the price we may have to pay to go from one period to two periods. This is the two period version of Eq. (2.35).

2.4.3 Sufficient Condition for Given Periods p_1, p_2 and $\hat{G}(z)=1$, $\phi=1$

Starting from Eq. (2.48) a sufficient condition for asymptotic stability is

$$\left|A_2(z)[\bar{G}(z)-1]\right|<1\,\forall\, z=e^{i\omega T} \tag{2.53}$$

The corresponding equation for a single period had $A_1(z)=z^{-p}$ whose magnitude is always one. The magnitude of $A_2(z)$ can be greater than one or less than one. One expects that one could make it equal to zero. The square bracket term in Eq. (2.50) becomes $1+e^{-i\omega T(p_2-p_1)}-e^{-i\omega Tp_2}$. If one can pick ω, p_1, p_2 to make the second and third terms conjugates of each other but with opposite sign, and make the real part of each equal to -0.5, then the sum is zero. For frequencies when $\left|A_2(e^{-i\omega T})\right|<1$, condition (2.53) is less restrictive than the single period case, allowing $\bar{G}(z)-1$ to go outside the unit circle. On the other hand, a particularly bad case occurs when we set $p_1=p_2$ and then the square bracket term equals $[2-e^{-i\omega Tp_2}]$. In this case the magnitude never gets less than unity, and by choice of ωTp_2 the value can reach the upper bound of 3. Figure 2-3 plots $A_2(z)$ for this case. The common period was set to $p_1=p_2=20$, in which case the plot goes around the contour 10 times. For comparison, Figure 2-4 gives the corresponding plot of $A_3(z)$ from Eq. (2.34) setting $p_1=p_2=p_3$.

2.5 HIGHER ORDER REPETITIVE CONTROL

Typical RC adjusts the command to a control system based on the error observed one period back in the disturbance. Various publications have suggested using data from multiple previous periods when making updates to the command each time step, and this is referred to as higher order RC (HORC). HORC considers the error not only one period back, but also includes the corresponding errors at multiple periods back. The form for the *N*th order HORC is

$$u(k) = \sum_{j=1}^{N} \alpha_j [u(k - jp) + \phi e(k - jp + 1)] \tag{2.54}$$

The generalized HORC law of Eq. (2.54) with RC compensator $F(z)$ and zero-phase low-pass filter $H(z)$ is

$$R_N(z) = \frac{\phi H(z) F(z)[\alpha_1 z^{(N-1)p} + \alpha_2 z^{(N-2)p} + \cdots + \alpha_N]}{z^{Np} - H(z)[\alpha_1 z^{(N-1)p} + \alpha_2 z^{(N-2)p} + \cdots + \alpha_N]} \tag{2.55}$$

It is also necessary to restrict the choice of the coefficient α_j to satisfy

$$\alpha_1 + \alpha_2 + \cdots + \alpha_N = 1 \tag{2.56}$$

From previous publications it was determined that when negative weights were allowed the control law would display an increase in robustness to period uncertainties. A popular choice for demonstrating such robustness is using a 3rd order HORC law with weights assigned as 3, -3, and 1 for α_1, α_2, and α_3 respectively. The design scheme is the same of the generic structure of RC shown in Figure 2-1. We replace $R(z)$ with $R_N(z)$ for the specific case of HORC.

2.5.1 Nonstandard Nyquist Criterion for Stability of HORC allowing Negative Weights

As it was the case of MPRC the characteristic polynomial must be rearranged so that problem of having poles on the unit circle is resolved. We can rewrite the polynomial as

$$z^{-Np}H(z)[1-\phi F(z)G(z)][\alpha_1 z^{(N-1)p}+\alpha_2 z^{(N-2)p}+\cdots+\alpha_N]=1$$

$$P_{NHORC}(z)=1 \tag{2.57}$$

The system is asymptotically stable if the $P_{NHORC}(z)$ image of the unit circle $z=e^{i\omega T}$ does not encircle the point +1.

2.6 FIGURES

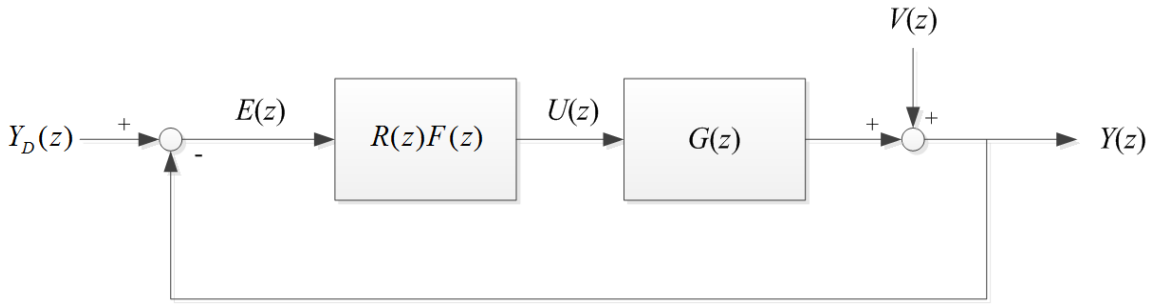

Figure 2-1. Block diagram of single-period repetitive control with periodic output disturbance

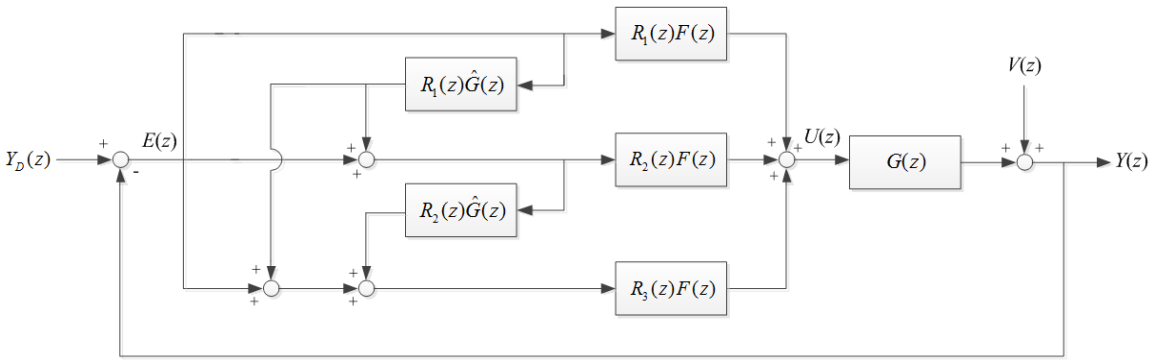

Figure 2-2. Block diagram of three-period repetitive control with periodic output disturbance

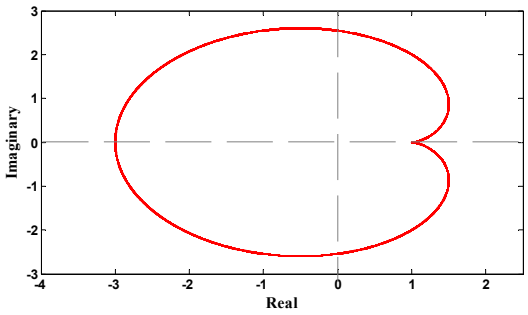

Figure 2-3. Polar plot of the coefficient A_2

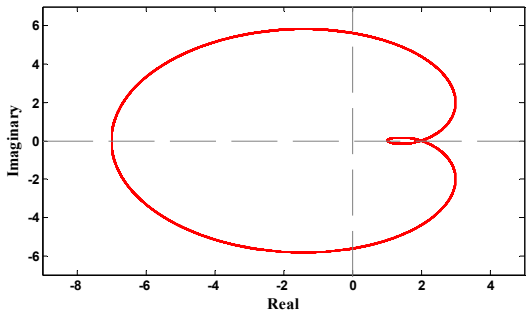

Figure 2-4. Polar plot of coefficient A_3

CHAPTER 3

EVALUATING THE STABILITY ROBUSTNESS TO MODEL ERRORS WITHIN MULTIPLE-PERIOD REPETITIVE CONTROL

3.1 INTRODUCTION

Stability of Repetitive Control (RC) is ensured when the RC compensator designed based on Eq. (2.7) and Eq. (2.8) represents the inverse of the frequency response of the feedback control system or plant. Model errors due to incorrect identification of the feedback control system or plant will deteriorate the function of the RC compensator and potentially cause instability within the RC system. From a control system perspective system identification relates to estimating the poles of the system. Any mismatch between the identified poles and true poles of the systems will be referred to as model errors. Poles within the system can be single or complex conjugate pairs. The complex conjugate poles consist of an undamped natural frequency mode ω_n and damping ratio ς such as $-\varsigma\omega_n \pm j\omega_n\sqrt{1-\varsigma^2}$. The two terms ω_n and ς equally contribute to the conjugate poles of the system. However, from a frequency response perspective it is the undamped natural frequency ω_n that is the initiating point of the decent within the magnitude of the frequency response, and gives us more intuition on the system bandwidth. For such reasons this chapter will focus on model error due to incorrect identification of the undamped natural frequency mode. Enough insight regarding the issue will be provided so that results can be generalized to the damping ratio and single pole case as well.

The main purpose of this chapter is to study the effect on stability robustness of introducing additional periods to be addressed by the RC law. As an addition to the existing method of the non-standard Nyquist criterion shown in Chapter 2, a sufficient and necessary condition of stability for all periods in Multiple-Period Repetitive Control (MPRC) is introduced as an

attempt to provide more convenience and usefulness for using hardware data when determining stability. The small gain stability theory for MPRC [26] is introduced to address model errors in MPRC by stabilizing the MPRC system with a small gain. The chapter concludes by showing numerical results to analyze stability robustness to model error of MPRC and provide insight for avoiding instability issue within hardware.

3.2 SUFFICIENT AND NECESSARY CONDITION FOR ALL PERIOD IN MULTIPLE-PERIOD REPETITIVE CONTROL

A sufficient and necessary condition of stability for all periods in Multiple-Period Repetitive Control (MPRC) is introduced as an attempt to provide more convenience and usefulness for using hardware data when determining stability. Three-period RC will be introduced first, followed by the stability condition of two-period RC.

3.2.1 Sufficient and Necessary Condition for All Periods in Three-Period Repetitive Control

The derivation starts off with the characteristic equation of Eq. (2.26) replace both p_1, p_2, and p_3 with p such as

$$z^{-3p}\{3\phi H[z^p - H]^2\bar{G} + 3\phi^2 H^2[z^p - H]\hat{G}\bar{G} + \phi^3 H^3\hat{G}^2\bar{G} - 3z^{2p}H + 3z^p H^2 - H^3\} = -1 \qquad (3.1)$$

The equation is packaged into the following equation as

$$z^{3p} + Az^{2p} + Bz^{p} + C = 0$$

$$A = 3[\phi\overline{G} - 1]H$$

$$B = 3\{-2[\phi\overline{G} - 1] + [\phi^2\hat{G}\overline{G} - 1]\}H^2 \tag{3.2}$$

$$C = \{3[\phi\overline{G} - 1] - 3[\phi^2\hat{G}\overline{G} - 1] + [\phi^3\hat{G}^2\overline{G} - 1]\}H^3$$

where the equation is a cubic polynomial with respect to the parameter z^p. We solve for z^p so that

$$z^p = \begin{cases} -\dfrac{A}{3} + R - Q \\ -\dfrac{A}{3} - \dfrac{1}{2}[R - Q] \pm \dfrac{\sqrt{3}}{2}[R + Q]j \end{cases}$$

$$R = \frac{\sqrt[3]{-2A^3 + 9AB - 27C + 3\sqrt{3}\sqrt{-A^2B^2 + 4B^3 + 4A^3C - 18ABC + 27C^2}}}{3\sqrt[3]{2}} \tag{3.3}$$

$$Q = \frac{-A^2 + 3B}{9R}$$

z^p is now isolated from the other terms and is able to represent the closed-loop roots of the RC system raised to p^{th} power. Reference [8] shows that within the root locus plot of an RC system the roots stay close to the unit circle for a large enough p value for any RC gain ϕ while the system is stable. From this we are now able to estimate the root decay rate per period $|z_i^p|$ by calculating the frequency response of the right hand side of the top equation in Eq. (3.3) such as

$$|z_i^p| \approx \begin{cases} \left| -\frac{A(e^{j\omega T})}{3} + R(e^{j\omega T}) - Q(e^{j\omega T}) \right| \\ \left| -\frac{A(e^{j\omega T})}{3} - \frac{1}{2}[R(e^{j\omega T}) - Q(e^{j\omega T})] \pm \frac{\sqrt{3}}{2}[R(e^{j\omega T}) + Q(e^{j\omega T})]j \right| \end{cases} \tag{3.4}$$

and stability is guaranteed when periods are large and identical for three-period RC by keeping Eq. (3.4) smaller than 1. Although it is yet to be shown within this item, later items show that an MPRC system is guaranteed to be stable for small periods being identical when stability has been determined for large period being identical in MPRC. Furthermore, the analyses will show that if MPRC is proved to be stable for identical periods, than any MPRC that includes any of those periods can be considered stable as well. Therefore the stability condition can be generalized to a necessary and sufficient condition for all periods in Three-Period RC such as

$$\begin{gathered} \left| -\frac{A(e^{j\omega T})}{3} + R(e^{j\omega T}) - Q(e^{j\omega T}) \right| < 1 \quad \& \\ \left| -\frac{A(e^{j\omega T})}{3} - \frac{1}{2}[R(e^{j\omega T}) - Q(e^{j\omega T})] \pm \frac{\sqrt{3}}{2}[R(e^{j\omega T}) + Q(e^{j\omega T})]j \right| < 1 \end{gathered} \tag{3.5}$$

The relationship within Eq. (3.6) can be further simplified by setting $\phi = 1$, $\hat{G} = 1$, and $H = 1$ such as

$$\begin{gathered} \left| \left[\sqrt[3]{\frac{\bar{G}}{1-\bar{G}}} + 1 \right]^{-1} \right| < 1 \quad \& \\ \left| \left[\left(-\frac{1}{2} \pm \frac{\sqrt{3}}{2} j \right) \sqrt[3]{\frac{\bar{G}}{1-\bar{G}}} + 1 \right]^{-1} \right| < 1 \end{gathered} \tag{3.6}$$

The condition has been substantially simplified without the RC gain ϕ and cutoff filter H.

3.2.2 Sufficient and Necessary Condition for All Periods in Two-Period Repetitive Control

The approach is analogous to the three-period case where we start off with the characteristic equation for two-period RC and replace both p_1 and p_2 with p.

$$2z^{-p}H[\phi\bar{G}-1]-z^{-2p}H^2\{2[\phi\bar{G}-1]-[\phi^2\hat{G}\bar{G}-1]\}=-1 \tag{3.7}$$

By setting $x=z^p$ we get

$$2Ax^{-1}-Bx^{-2}+1=0$$

$$A=H[\phi\bar{G}-1] \tag{3.8}$$

$$B=H^2\{2[\phi\bar{G}-1]-[\phi^2\hat{G}\bar{G}-1]\}$$

where we can analytically solve for x by solving the quadratic polynomial equation and thus find z^p such as

$$z^p=\pm\sqrt{A^2+B}-A \tag{3.9}$$

z^p is now isolated from the other terms and is able to represent the closed-loop roots of the RC system raised to p^{th} power. By the same logic of the previous case, the root decay rate per period $|z_i^p|$ can be estimated by calculating the frequency response of the right hand side of the top equation in Eq. (3.9)

$$z_i^{\,p}\approx\pm\sqrt{A(e^{j\omega T})^2+B(e^{j\omega T})}-A(e^{j\omega T})\quad\forall\quad\omega\subset[0\quad\omega_{Nyquist}] \tag{3.10}$$

$$\left|\pm\sqrt{A(e^{j\omega T})^2 + B(e^{j\omega T})} - A(e^{j\omega T})\right| < 1 \quad \forall \quad \omega \subset [0 \quad \omega_{Nyquist}] \tag{3.11}$$

The equation above is the sufficient and necessary condition for all periods regarding two-period RC. For the simple case when ϕ = 1 and $\hat{G}$ = 1, the relationship of Eq. (3.9) can be reduced to

$$z^p = \left(\pm\sqrt{\frac{\bar{G}}{\bar{G}-1}} + 1\right)^{-1} \tag{3.12}$$

and the sufficient and necessary condition for all periods is now

$$\left|\left(\pm\sqrt{\frac{\bar{G}}{\bar{G}-1}} + 1\right)^{-1}\right| < 1 \quad \forall \quad \omega \subset [0 \quad \omega_{Nyquist}] \tag{3.13}$$

By mere comparison between Eq. (3.13) and Eq. (3.6), one can see that inversion of the cubic root term of Eq. (3.6) will make the overall value larger than the inversion of the square root in Eq. (3.13). Thus, three-period RC will be less robust to model errors in terms of stability when compared to two-period RC. This statement will be proved in a different way in later items with stability boundary analysis.

3.3 SMALL GAIN STABILITY THEORY FOR MULTIPLE-PERIOD REPETITIVE CONTROL

Establishing the stability of multiple period repetitive control systems is hampered by the fact that the periods are usually a large number of time steps, and this can easily create very high degree polynomials which can cause trouble to root finding algorithms. For the single period repetitive control, the necessary and sufficient condition for all possible periods, Eq. (2.16), is

close to being the stability boundary for all periods except ones that only have a few time steps. MPRC is not so lucky. The Nyquist based stability conditions developed here helps address the difficulty of determining stability, but can be frustrating in that the plots can be complicated making it difficult to determine if the point -1 has been encircled or not. Normally we use gain $\phi = 1$ since the design process optimizes the gain. Following Reference [27], another approach is to make use of root locus departure angle thinking. If we can show that as this gain is turned up from zero, all of the roots on the unit circle depart with an inward component toward the center of the circle, then we know that there exists a range of nonzero gains ϕ for which the multiple period repetitive control system is asymptotically stable. We do such an analysis for the three period RC with the $H_j(z)$ set to unity, and we allow three different gains ϕ_j, one for each period. Define numerators and denominators $\overline{G}(z) = \overline{G}_N(z) / \overline{G}_D(z)$ and $\hat{G}(z) = \hat{G}_N(z) / \hat{G}_D(z)$. Substitute $\hat{R}(z)$ into $1 + \hat{R}(z)\overline{G}(z) = 0$, put everything over a common denominator, and then examine the characteristic polynomial of the RC system in the numerator. We examine the departure angles for the roots of $z^{p_1} = 1$, but the results for other periods are analogous. The characteristic equation can be written as

$$(z^{p_1} - 1)\alpha(z) + \beta(z) + \gamma(z) + \delta(z) = 0 \tag{3.14}$$

$$\begin{aligned}
\alpha(z) &= (z^{p_2} - 1)(z^{p_3} - 1)\hat{G}_D^2(z)\overline{G}_D(z) \\
\beta(z) &= [\phi_1(z^{p_2} - 1)(z^{p_3} - 1) + \phi_2(z^{p_3} - 1)(z^{p_1} - 1) + \phi_3(z^{p_1} - 1)(z^{p_2} - 1)]\hat{G}_D^2(z)\overline{G}_N(z) \\
\gamma(z) &= [\phi_1\phi_2(z^{p_3} - 1) + \phi_2\phi_3(z^{p_1} - 1) + \phi_3\phi_1(z^{p_2} - 1)]\hat{G}_D(z)\hat{G}_N(z)\overline{G}_N(z) \\
\delta(z) &= \phi_1\phi_2\phi_3\hat{G}_N^2(z)\overline{G}_N(z)
\end{aligned} \tag{3.15}$$

There is explicit dependence on ϕ_1, and of course, the roots are functions of this gain $z = z(\phi_1)$. We assume that we are turning up all gains at the same time, but not necessarily at the same rate, all starting from zero gain. To find departure direction in the complex plane for the roots of $z^{p_1} = 1$ and also the departure velocity, we differentiate the characteristic equation with respect to ϕ_1, and evaluate at what we call condition *c*, i.e. $z^{p_1} = 1$, $\phi_1 = \phi_2 = \phi_3 = 0$. Note, the result will be the same, if instead, we were to make all ϕ_j equal, and turn them up all at the same time.

The derivatives $d\delta(z)/d\phi_1\big|_c = 0$ and $d\gamma(z)/d\phi_1\big|_c = 0$ are zero after evaluating at *c*. Differentiate the other two terms and evaluate at *c*, $d\beta(z)/d\phi_1\big|_c = (z^{p_2}-1)(z^{p_3}-1)\hat{G}_D^2(z)\bar{G}_N(z)\Big|_c$ and $d((z^{p_1}-1)\alpha(z))/dz\Big|_c\, dz/d\phi_1\big|_c = 2p_1 z^{p_1-1}\alpha(z)\Big|_c\, dz/d\phi_1\big|_c$. Adding these together, using the fact that $z^{p_1} = 1$, and equating to zero produces

$$(z^{p_2}-1)(z^{p_3}-1)\Big|_c \frac{dz}{d\phi_1}\Big|_c = -\frac{z}{p_1}\bar{G}(z)\Big|_c (z^{p_2}-1)(z^{p_3}-1)\Big|_c \tag{3.16}$$

For any root under consideration for $z^{p_1} = 1$, if that root is not also a root of either $z^{p_2} = 1$ or $z^{p_2} = 1$, then the associated factors can be cancelled on each side of the equation, and the complex vector velocity of departure from the roots of $z^{p_1} = 1$ as the gain ϕ_1 is increased from zero, is

$$\frac{dz}{d\phi_1}\Big|_c = -\frac{z}{p_1}\bar{G}(z)\Big|_c \tag{3.17}$$

Common roots can occur. For example, all factors have a root at +1. Use of L'Hopital's rule can establish that Eq. (3.17) still holds in this case.

The z in Eq. (3.17) is the root location of interest, and can be considered as a vector from the origin to the root on the unit circle. Then $-z$ is a unit vector in the opposite direction, pointing radially inward. If one succeeds in designing the compensator $F(z)$ such that $\bar{G}(z)$ is unity, as cost function Eq. (2.8) aims to do (when V is zero), then we conclude that all p_1 roots depart radially inward, and similarly for the p_2 and p_3 roots. Equation (3.17) then defines the amount of model error that can be tolerated and still have a region of convergence for sufficiently small gain. Provided the phase angle of the product $\bar{G}(z) = F(z)G(z)$ is not greater than +90 degrees nor smaller than -90 degrees at any frequency, then the RC law is stable for sufficiently small gain. Finding the root with the largest deviation in departure angle from radially inward can be helpful in pointing out what frequency range is most critical in the polar Nyquist plot, when trying to determine whether -1 is encircled.

3.4 NUMERICAL INVESTIGATION OF STABILITY ROBUSTNESS OF MULTIPLE-PERIOD REPETITIVE CONTROL

Robustness to model error is investigated numerically in this section for two period repetitive control of a third order system that is a reasonably good model of the feedback controllers for each link of a Robotics Research Corporation robot

$$G(s) = \left(\frac{a}{s+a} \right) \left(\frac{\omega_n^2}{s^2 + 2\zeta\omega_n s + \omega_n^2} \right) \tag{3.18}$$

where $a = 8.8\,(1.4\ \text{Hz})$, $\omega_n = 37\,(5.9\ \text{Hz})$, and $\zeta = 0.5$. Unless otherwise indicated, the compensator is designed using Eqs. (2.7) and (2.8) with $n = 12, m = 7, V = 0$, and we set $\phi = 1$. We consider that the input comes through a zero order hold sampling at 100 Hz. We consider model error of the form of either a positive change in the value of ω_n or a negative change, prescribed as a percentage change. Changes in a create similar results but are less sensitive. We also consider model error that is a positive or negative change in the DC gain. Figure 3-1 shows a detail of the departure of the root locus from poles on the unit circle with a positive model error of 40%, with $p_1 = p_2 = 20$ which makes the poles on the unit circle repeated. One of the poles departs with largest deviation from radially inward, and then goes unstable when $\phi = 0.81$.

3.4.1 Robustness Limits for a Range of Periods

We consider periods p_1 and p_2 in the range from 12 to 200. These values are small enough that we can directly find the roots of the characteristic polynomial as our method of finding the stability boundary to model error. But they are big enough to see the behaviors of Nyquist plots. The procedure followed first sets p_1 to 12, and incrementally sets p_2 to values from 12 to 200, for each combination sampling positive and negative errors in the value of ω_n to find the stability boundaries in each direction. Then the value of p_1 is incremented and the process repeated until it reaches 200. The positive and negative stability boundaries for $p_1 = 26$ and 67 for all p_2 are given in Figures 3-2 and 3-3. Phase error is the main driver in producing instability, and for error in ω_n and also a, this suggests that more positive model error than negative model error is allowed. The phase Bode plot for a first order term, is approximately linear from one decade below to one decade above the break frequency, when plotted on a log

frequency scale, and this implies the same amount of phase error magnitude corresponds to a much larger percent change in positive break frequency than for negative break frequency. A second order factor with critical damping just doubles the effect, and with less damping similar behavior is observed. Figure 3-4 plots the phase of a second order system with undamped natural frequency at 4 rad/sec, and a damping ratio of 0.5. Also shown are phase plots for +50% model error (i.e. the new ω_n is 1.5 times the old) and for -50% model error. The plot shows that the negative change in the undamped natural frequency produces much larger changes in phase than the corresponding change in phase for the same percent change in the positive direction. Note that the positive error curves in Figures 3-2 and 3-3 have many minima each appearing to reach the same minimum value, but this minimum value changes as we change p_1.

3.4.2 Comparison of Robustness of Single Period and Two Period RC

The top curve in Figure 3-5 gives the stability boundary for positive error for a single period p (or p_i on the plot), corresponding to satisfying the modified Nyquist condition Eq. (2.14). The next curve down is a straight line corresponding to the necessary and sufficient condition for all possible p given by Eq. (2.15). If Eq. (2.15) is not satisfied for an interval of frequencies, then multiplying by $A_1(z) = e^{-i\omega Tp}$ as in Eq. (2.13) will rotate and amplify the phase difference from start to end of the interval. And then for large enough p the plot will encircle -1. This explains the sawtooth nature of the top plot, and the fact that the peaks decay as the period gets larger. The negative error limit for the undamped natural frequency for the single period case is the bottom most curve. This plot does not vary significantly, but it also has a straight line that goes through the minimum error points on the curve. Also on the plot in the middle are positive error and negative error curves for the two period case. These are computed as follows. For each value

of p_1 (which is now the p_i of the horizontal axis) a plot as in Figures 3-2 and 3-3 is made, and the minimum distance to the stability boundary in each direction is determined for all p_2, and this is plotted in Figure 3-5. We observe the same properties as in the single period case, but now the stability boundary in each direction is significantly tighter. The necessary and sufficient condition for asymptotic stability for all periods is then determined to be +28.65% and -11.67% error in the undamped natural frequency. Note that the sufficient condition Eq. (2.51) produces limits +16.90% and -11.37%. The former is far from the real stability boundary presented here, while the negative error limit is similar for both. Equation (2.51) aims to keep the magnitude of the Nyquist polar plot less than unity, and it will become clear that unlike the single period case, the two period case can very easily be stable with a magnitude going greater than unity.

3.4.3 Understanding Stability With Positive Error in Undamped Natural Frequency

Figure 3-6 examines the plot of $P_2(z) = A_2(z)[\bar{G}(z) - 1]$ with the model error set at +28.65% with z going around the top half of the unit circle ($\phi = 1$, $\hat{G} = 1$, $p_1 = p_2 = 20$). Figure 3-7 gives the phase of the plot relative to the point -1, and we see that there is a very sharp phase change at 6.16Hz, but it does not produce an encirclement. Hence, this value is very slightly below the actual stability boundary. To understand this plot we look at the components. The $A_2(z)$ was plotted in Figure 2-3. We can describe this plot as an apple. The indentation of the apple is at distance one from the origin, but the opposite end of the apple is three units from the origin. Figure 3-8 is a plot of the complex values $[\bar{G}(e^{i\omega T}) - 1]$, while Figure 3-9 gives its magnitude and Figure 3-10 its phase angle as a function of frequency. Because of the phase approaching -180 degrees for much of the frequency range, the product of these terms reverses the image of the apple making the indentation face the point -1. The fact that the magnitude is about 0.4 for this

range of frequencies means that there is no danger of encircling the point -1 at these frequencies. The situation is different for negative model error. The plot nearly encircles -1 for a low frequency, for which the phase has not yet approached -180 degrees. We see the first of the 10 images of the indentation of the apple somewhere near -90 degrees. We observe that a large percentage of the plot is outside the unit circle for this plot that is essentially on the stability boundary. This could not happen in the single period case, and we will see that it does not happen in the negative error case either.

3.4.4 The Common Minima and the Decaying Maxima in the Positive Error Boundary

Consider a hypothetical case where the marginally stable situation is encountered when $p_1 = p_2 = 4$ (we use the fact that one can reach minima using repeated frequencies). Figure 3-11 plots $A_2(z)$ for this value and also for $p_1 = p_2 = 10$. Also indicated is a point at 8Hz where the plot goes through -1. Increasing the value of $p_1 = p_2$ will make more and more peaks in the plot, and one can find infinitely many periods that give marginal stability. These correspond to minima in Figure 3-5. The fact that the peaks in Figure 3-11 become arbitrarily close together suggests that the heights of the peaks in the positive error of the stability boundary will decay as the period increases. This suggests that one can find the common minimum values of the valleys in the positive error plot of Figure 3-5 for two periods by simply using a very large value of $p_1 = p_2$ in Eq. (2.47) with $z = e^{i\omega T}$. Figure 3-12 illustrates the decaying property of the peaks and the common value of the minima.

3.4.5 Understanding Stability With Negative Error in Undamped Natural Frequency

Figures 3-13, 3-14, 3-15, and 3-16 are plots using -11.67% error in undamped natural frequency, analogous to Figures 3-6, 3-8, 3-9, and 3-10 above for positive model error. The important property is that the phase angle of $[\bar{G}(z)-1]$ tends toward zero instead of -180 degrees. And the result is that the product with $A_2(z)$ preserves the direction of the indentation of the apple. Thus, the side of the apple that reaches radius 3 is facing the point -1. One implication is that for stable systems the polar plot does not go far outside the unit circle, unlike the positive error case. The smooth curve reaching radius 3 in comparison to having the indentation approaching -1, means that there is little fluctuation in the stability boundary as we change the periods involved. Furthermore requiring the plot to stay less than unity is much closer to the stability boundary for negative error.

3.4.6 Examining Error in the DC Gain of the Model

The above analysis examined model error in the value of the undamped natural frequency. Equation (2.58) automatically adjusts the DC gain when we change this value, so the approach has separated the effects of changing the frequency from the effects of changing the DC gain. Now consider that we multiply the transfer function in Eq. (3.18) by a gain that is nominally unity, but can be under or over estimated. Figure 3-17 is a polar plot of $[\bar{G}(e^{i\omega T})-1]$ including both +28.65% error and -11.64% error in the undamped natural frequency, and considering various values of error in this overall DC gain. Smaller gains shrink the plot toward -1. Figure 3-18 gives the corresponding Nyquist plot with +100% error in the model DC gain. This situation is asymptotically stable, whereas 30% error in the undamped natural frequency was unstable without the DC error. Hence, overestimating the model error can improve the robustness of the repetitive control system. Figures 3-19 and 3-20 present the stability boundaries for positive and

negative error of the DC gain, and for positive error it is possible to have the robustness decrease if there is too much DC error. The robustification that results from overestimating DC gain is similar to decreasing the value of ϕ which is discussed below, but decreasing ϕ should not be able to decrease the stability robustness.

3.4.7 Using a Less Perfect Compensator

All of the above computations were made using a 12 gain design for the compensator $F(z)$. Consider what happens when we use fewer gains meaning that $\hat{G}(z)$ is not as close to being equal to one. Figure 3-21 presents the positive and negative stability boundaries when using 12, 10, and 8 gain designs, computed by finding roots of the characteristic equation. We note that there is rather little change in the stability boundaries. One can also set $\phi = 1$ and use Eq. (2.49) to study the effects of imperfect $\hat{G}(z)$. The $\hat{A}_2(z)$ of Eq. (2.49) is plotted in Figure 3-22 for an 6 gain design and +28.65% model error. The plot is fairly strongly affected, and it now goes out beyond -3. Note that the extra term on the right in Eq. (2.49) could exhibit ill conditioning because use of a good approximation of the model can make the ratio in the round brackets look much like zero over zero. Figure 3-23 presents a detailed view of Figure 3-21, and it is interesting to note that the 8 gain design is actually the most robust of the 8, 10, and 12 gain designs. It may be possible that model error can be in a direction that is helpful to robustness, as happened with overestimating DC gain.

3.4.8 Improved Robustness By Decreasing Repetitive Control Gain

The small gain stability theory based on departure angle information suggests that one can have model phase error approaching ± 90 degrees. In single period RC this is the maximum

possible model phase error as well, and it is also achieved as the repetitive control gain tends to zero. The result produced here says that this small gain error tolerance appears to be unaffected by how many periods are being addressed. Of course, one pays for this robustness by having slow learning rates. Figure 3-24 gives the positive and negative error stability boundaries for the undamped natural frequency, using a range of different values of ϕ. The effect is somewhat similar to that of overestimating the DC gain discussed above.

3.4.9 The Effect of Introducing a Penalty on Compensator Gain Size

The cost function Eq. (2.8) allows one to use a weight factor V penalizing the size of the gains in the compensator. This can avoid having successive gains be large and of opposite sign, which could be sensitive to noise in data. As one turns on this penalty, the restriction of the size of the gains makes learning at high frequencies more difficult, and gives the compensator a low pass filter characteristic. And the cost functional no longer aims to make $\hat{G}(z)$ as close to one as possible for all frequencies. Using a perfect model, the plot of $[\bar{G}(e^{i\omega T})-1]$ becomes a straight line on the real axis going toward -1 from zero. With a big enough V, the high frequencies can become sufficiently ignored that the plot can go past -1 producing instability. Figure 3-25 plots the magnitude of $[\bar{G}(e^{i\omega T})-1]$ for different values of V. Figure 3-26 presents the positive and negative stability boundaries for error in the undamped natural frequency as a function of the value of V. It is not clear that there is any particular trend in the result, but the sudden onset of instability of the design is evident when the value of V reaches a critical value.

3.5 CONCLUSIONS

This chapter analyzes stability robustness characteristics to investigate how the model error can harm stability in MPRC. The results provide intuition to the designer for avoiding instability

in MPRC or assessing the cause for a currently unstable MPRC system. Some conclusions are provided within the following. Addressing more frequencies in MPRC decreases stability robustness to model error. In other words, it is vital to have an accurate model when addressing a multiple of frequency components in order to avoid instability. Stability is much more sensitive to underestimating the undamped natural frequency than it is to overestimating it. Using a small penalty factor in designing the RC compensator can make MPRC unstable.

The results above show that model error can make MPRC unstable. The issue could be addressed by stabilizing the system with a small RC gain complying with the small gain stability theory for MPRC. Simpler methods for determining stability of MPRC using hardware data were derived using results from stability boundary analysis.

3.6 FIGURES

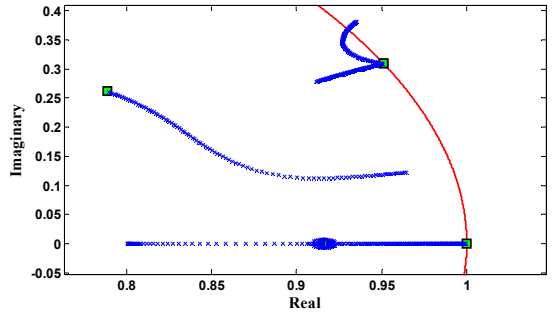

Figure 3-1. Root locus plot of two-period RC with + 40 % model error in ω_n when $p_1 = p_2 = 20$

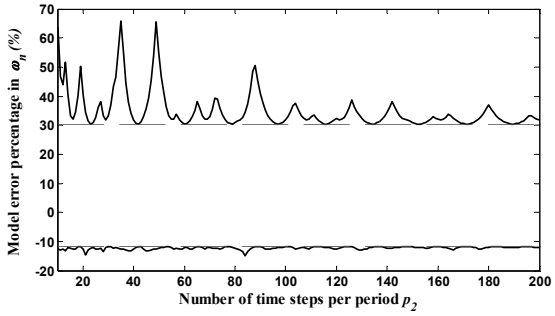

Figure 3-2. Stability boundary of two-period RC with model error in ω_n when $p_1 = 20$

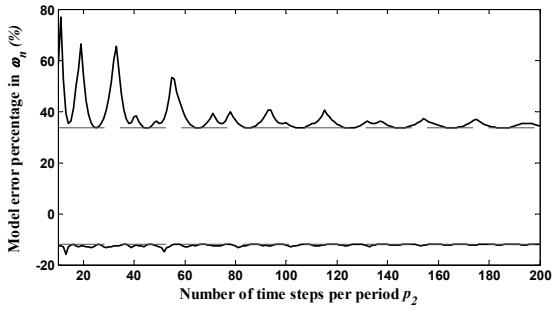

Figure 3-3. Stability boundary of two-period RC

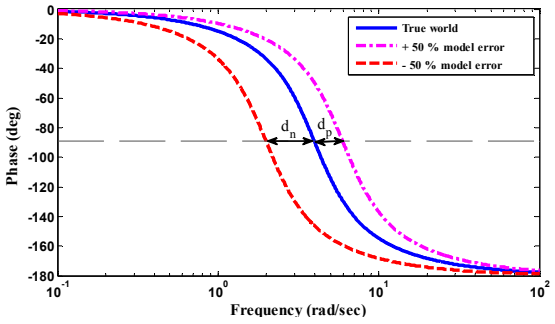

Figure 3-4. Difference in phase error with

with model error in ω_n when p_1=67

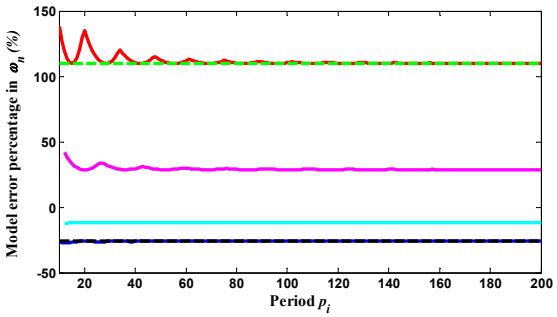

Figure 3-5. Sufficient and necessary stability boundary of two-period RC for all periods

respect to positive and negative model error

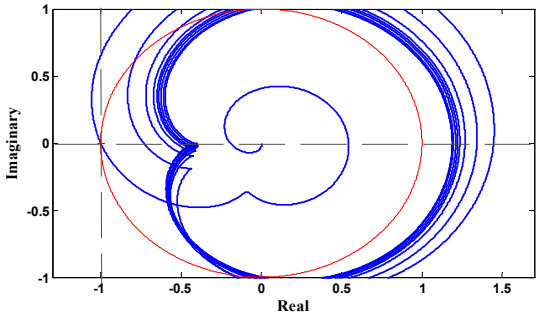

Figure 3-6. Polar plot of P_2 ,+ 28.65 % error

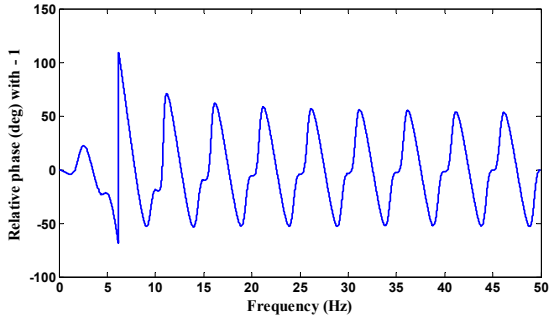

Figure 3-7. Relative phase of P_2 with respect to -1

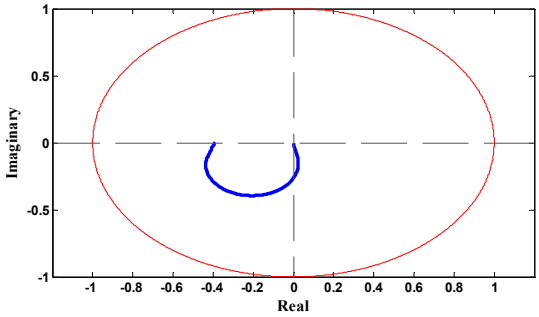

Figure 3-8. Polar plot of $[\overline{G}(e^{i\omega T})-1]$

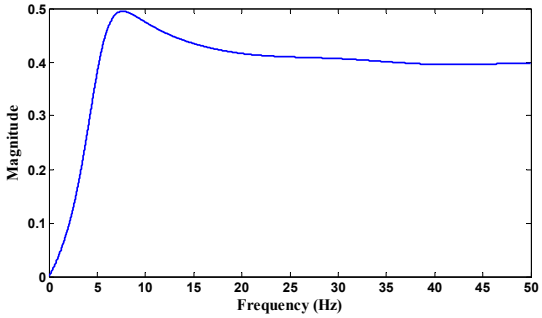

Figure 3-9. $\left|\overline{G}(e^{i\omega T})-1\right|$ plot

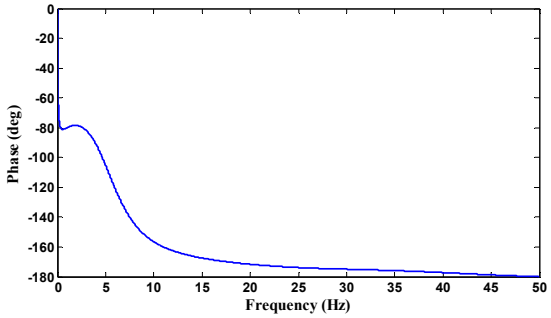

Figure 3-10. $\measuredangle[\overline{G}(e^{i\omega T})-1]$ plot

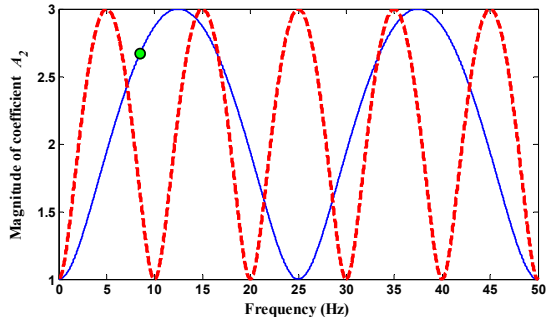

Figure 3-11. The magnitude of A_2 and marker for frequency component that crosses -1

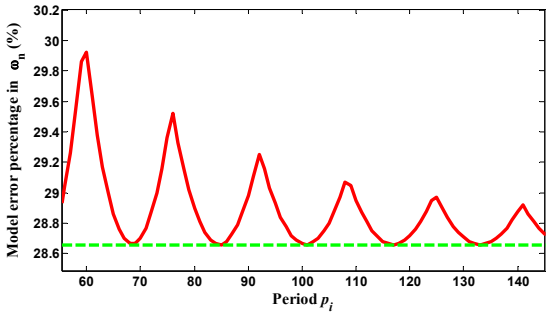

Figure 3-12. Enhanced view of the stability boundary and sufficient condition

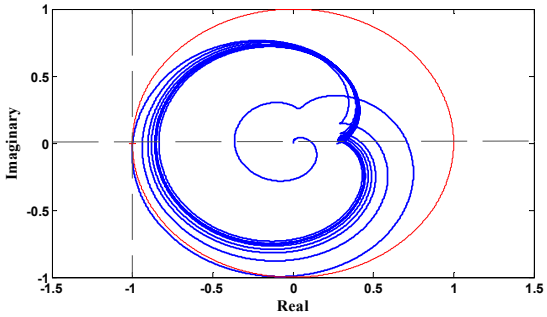

Figure 3-13. Polar plot of P_2 ,- 11.67 % error

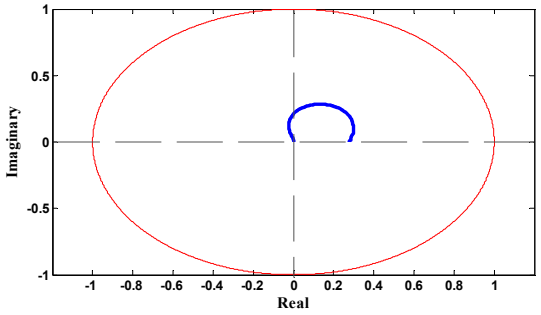

Figure 3-14. Polar plot of $[\overline{G}(e^{i\omega T})-1]$

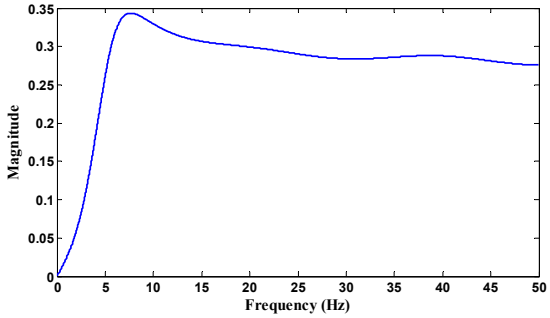

Figure 3-15. $\left|\overline{G}(e^{i\omega T})-1\right|$ plot

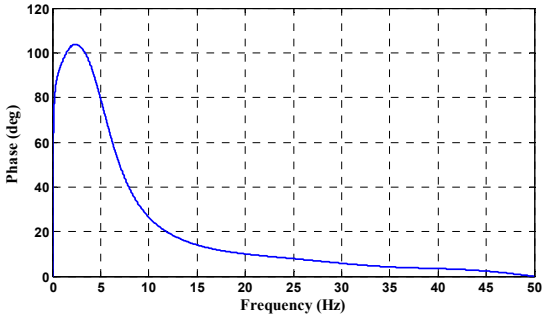

Figure 3-16. $\measuredangle[\overline{G}(e^{i\omega T})-1]$ plot

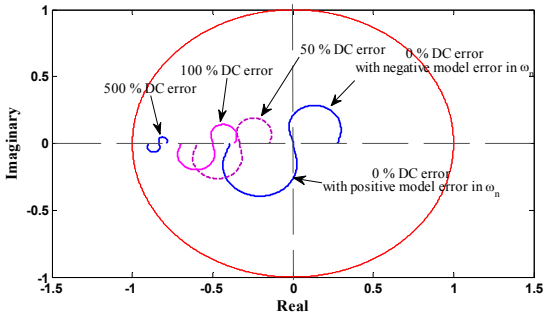

Figure 3-17. Various polar plots of $[\overline{G}(e^{i\omega T})-1]$ each associated with positive DC error

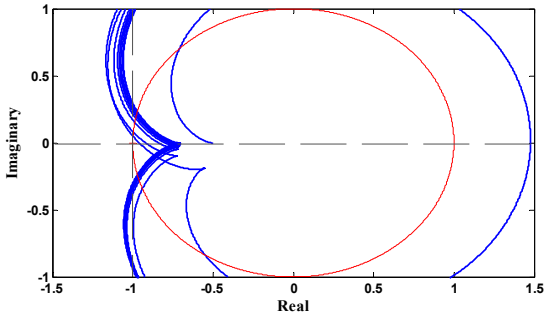

Figure 3-18. Polar plot of P_2 for two-period RC with 100 % DC error and + 30 % model error

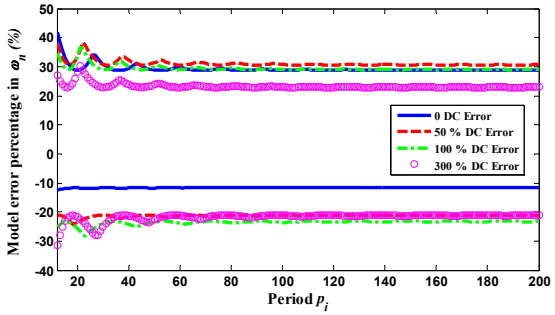

Figure 3-19. Stability boundary plots associated with different positive DC errors

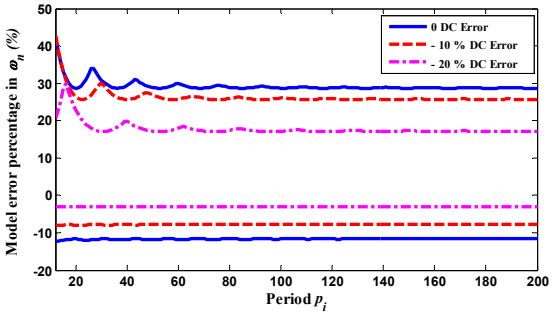

Figure 3-20. Stability boundary plots associated with different negative DC errors

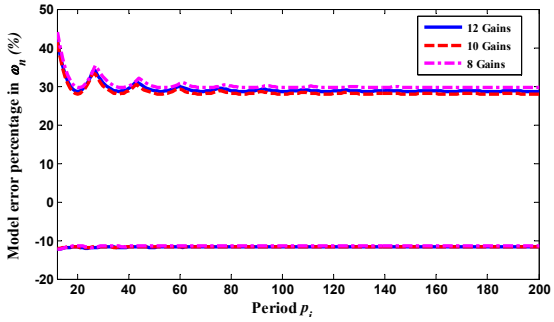

Figure 3-21. Stability boundary plots associated with different number of RC compensator gains

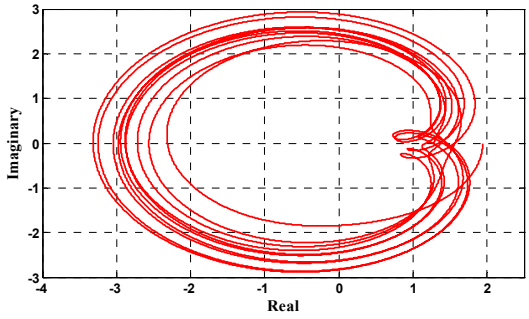

Figure 3-22. Polar plot of $\hat{A}_2$ with 6 gains for the RC compensator, + 28.65 % error

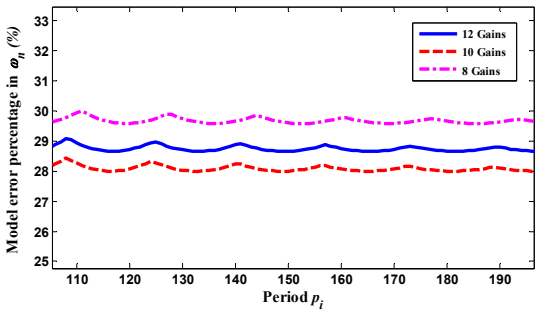

Figure 3-23. Enhanced view of the stability boundaries in Figure 3-21

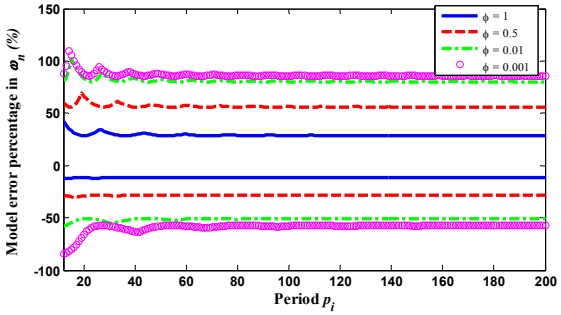

Figure 3-24. Stability boundary plots associated with different RC gains

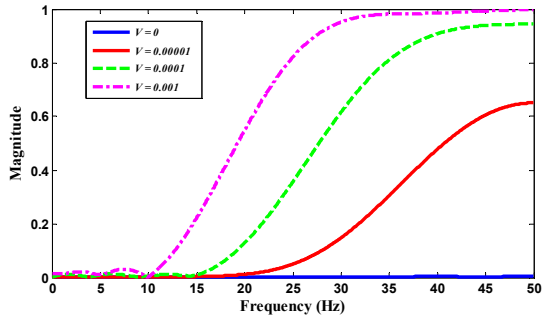

Figure 3-25. $\left|\overline{G}(e^{i\omega T})-1\right|$ with different *V*'s

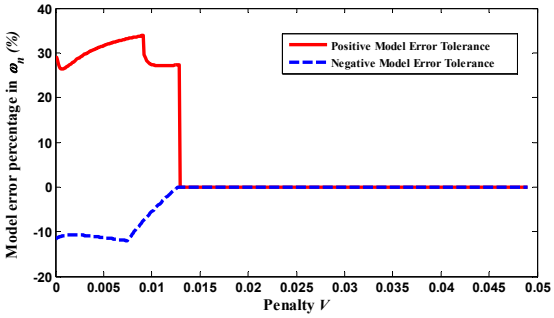

Figure 3-26. The sufficient and necessary condition for all periods with respect to varying *V*'s

CHAPTER 4

INCREASING ROBUSTNESS TO PERIOD UNCERTAINTIES OR FLUCTUATIONS WITH MULTIPLE-PERIOD REPETITIVE CONTROL

4.1 INTRODUCTION

Spacecraft often have multiple rotating parts such as CMG's, reaction wheels and momentum wheels. Slight imbalance within any of these devices will cause vibration of the spacecraft structure that can impair the functioning of fine pointing equipment. Imbalances can occur for multiple devices and the vibrations can have multiple periods correspondingly. In previous studies an improved method for designing repetitive controllers to handle multiple unrelated periods was introduced (Refs. [19], [20], [21], [22]) and referred to as Multiple Period Repetitive Control (MPRC). In a more recent paper (Ref. [28]) the theory was tested on the Naval Postgraduate School (NPS) Three-Axis Spacecraft Simulator 2 (TAS2) along with four other candidate methods that were implemented to address CMG induced optical jitter within a laser beam. Among various experimental results that were conducted on the TAS2, MPRC displayed capabilities of not only getting rid of the period of interest, but rejecting the neighboring frequencies as well when all three control components of the MPRC law were addressing identical periods. From the view point of the experiments, this method was very effective for the given situation where uncertainties laid within the disturbance period information that was given by the CMG Hall Effect sensors due to numeric truncation error of the sampled data. The previously existing method to address fluctuations and uncertainty in the disturbance period is Higher Order Repetitive Control (HORC) with negative weights. It was originally developed by Steinbuch (Ref. [23]), and was studied in detail by two different approaches in (Refs. [24], [25]).

It is the purpose of this chapter to investigate the relationship between the two methods while comparing various features of each method when adjusting different design parameters. Among the two methods, MPRC will be shown to have advantages.

4.2 THE REQUIRED ACCURATENESS ON THE KNOWLEDGE OF THE DISTURBANCE PERIOD WHEN ADDRESSING LOW FREQUENCY COMPONENTS RELATIVE TO NYQUIST FREQUENCY

Accurate identification of the disturbance period is essential for typical RC systems in order to completely eliminate the frequency component within the disturbance signal. In RC practice, it is possible to have small uncertainties within the disturbance addressed by the RC law. Small errors in identifying the disturbance period can drastically degrade the performance of RC.

Accepting the fact that such uncertainties do exist, another view is taken on the matter with respect to the speed of the disturbance frequency relative to Nyquist. Figure 4-1 below shows a numeric simulation on how sensitive the single-period repetitive controller is in terms of disturbance period accurateness where the goal is to reduce the error by at least a factor of 100. It is assumed within the simulation that one can design a perfect RC compensator so that the dynamics of the plant can be completely nullified, thus $\bar{G} = 1$ within the frequency domain. The sample rate of the digital system is 100 Hz.

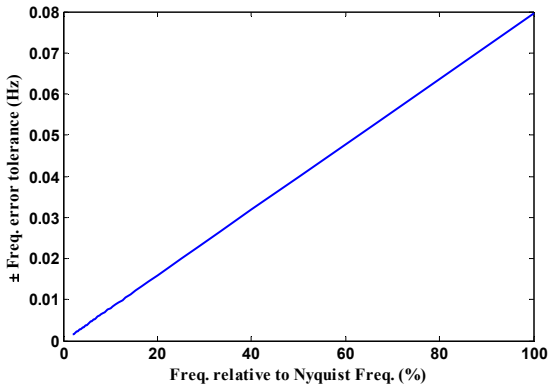

Figure 4-1. Frequency error tolerance of single period RC for factor of 100 error reduction

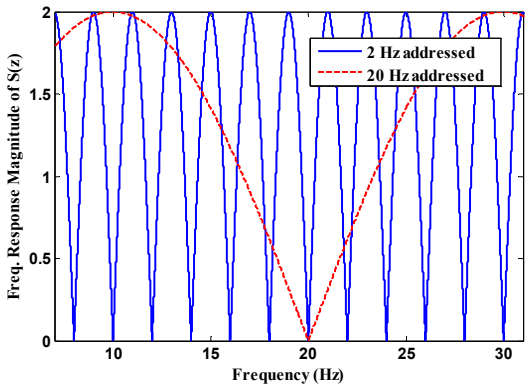

Figure 4-2. Sensitivity transfer function for 2 Hz and 20 Hz at 100 Hz sample rate

Figure 4-1 describes that more accurateness of the disturbance period is required when the frequency component being addressed is low compared to Nyquist frequency. Such accurateness can become unfeasible at low frequencies close to DC when practicing RC on hardware. The issue gives rise to the need of HORC to completely reject the low frequencies components within the disturbance signal despite having these uncertainties or fluctuations. Some intuition on this phenomenon is provided within Figure 4-2 where the slope around each notch gets less steep as a higher frequency is addressed for a fixed sample rate. The next simulation is performed by increasing the sample rate of the digital system.

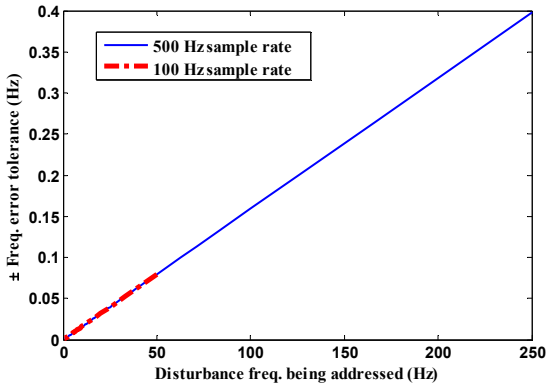

Figure 4-3. Frequency error tolerance for different sample rates with single period RC

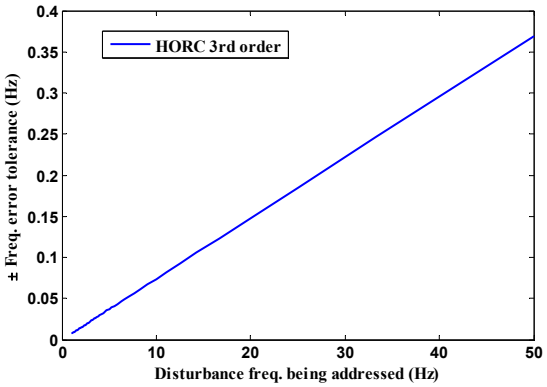

Figure 4-4. Frequency error tolerance of (3,-3,1) HORC for factor of 10000 error reduction

Figure 4-3 shows that the sample rate itself has no effect on the frequency error tolerance of a specific frequency component being addressed by single period RC. It can also be seen that the frequency error tolerance increases with respect to an increase of the disturbance frequency component being addressed. This relationship looks somewhat linear and it is gives basis to the thought that the frequency component being addressed will be more tolerate to period uncertainties and fluctuations as the addressed frequency becomes higher regardless of the sample rate being used. By curve fitting Figure 4-3 into a linear equation one can gain a general idea on how accurate the indentified disturbance period has to be in order to achieve at least a factor of 100 error reduction for single period RC. A linearized relationship such as Eq. (4.1) can be deduced from Figure 4-3 so that one can roughly estimate the frequency tolerance of all frequencies at any sample rate for single period RC.

$$\Delta F_{tol} = 0.00159 F_{disturbance} - 1.75 \times 10^{-5} \tag{4.1}$$

In RC practice this relationship will be less accurate due to model errors when designing the RC compensator, in which case deters $\bar{G}$ from being equal to 1. Above all, whatever disturbance period uncertainties there may be, the need for HORC will become larger as one addresses disturbance frequencies that are relatively low compared to Nyquist frequency.

4.2.1 Implementing HORC for increasing tolerance to disturbance period uncertainties

A similar numeric simulation to that of the single period RC case was performed in order to determine the frequency error tolerance of a 3rd order (3, -3, 1) HORC law that achieves the goal of reducing the error by at least a factor of 10000 shown in Figure 3-4. Despite the increased effort of a factor of 10000 error reduction, the frequency error tolerance is substantially larger than that of the single period RC case for any frequency component being addressed. Even if

model errors were to be taken into account within the simulation, it is still certain that HORC will demonstrate superior capabilities of addressing a disturbance period with uncertainties.

4.2.2 Issues in synchronizing with CMG period through the Hall effect sensor readings in a spacecraft testbed

The NPS TAS2 was able to provide information on the rotor speed of each CMG through Hall sensor readings. The Hall sensor will output a pulse signal used for indicating the current position of the rotor within the CMG. In order to calculate the period of the CMG rotation, the number of time steps is calculated between the pulse signals indicating one complete revolution. Since the Hall effect sensor reading is acquired through a sample and hold device, the calculated period of the CMG will always be an integer number regardless of the actual speed of the rotor. For rotation speeds that correspond to a non-integer number of periods, there will always be a deviation error from the actual non-integer disturbance period and the integer period being addressed by RC. This issue poses the problem of having period uncertainties in RC. However, instead of using HORC to resolve this issue, MPRC was capable of resolving this issue by addressing multiple identical periods for the particular case of having the three CMGs of the spacecraft testbed rotating at the same speed.

4.3 IDENTICAL TRANSFER FUNCTION REPRESENTATION FOR MPRC AND HORC

As mentioned previously, experimental results with NPS's TAS2 testbed showed that MPRC had capabilities of increasing the robustness to period uncertainties when addressing multiple periods that were identical. This particular configuration for MPRC will be referred to as MPRC*i* from now on. The functionality of MPRC is very similar to that of the 3rd order HORC with 3, -

3, and 1 as weights. It is developed here to show that when certain conditions are met for both methods, MPRC*i* and HORC will have the same digital transfer function representation.

The transfer function relationship between error $E(z)$ and the control input $U(z)$ is stated in Eq. (2.21). The idea of MPRC*i* is to address multiple identical periods so that all periods p_j are equal to p accordingly. By setting both the cutoff $H_j(z)$ and RC gain ϕ_j to 1, one is able to rewrite the equation as

$$\left[\frac{U(z)}{E(z)}\right]_{\text{MPRC}i,\hat{G}\neq 1} = \frac{3z^{2p} + (-6 + 3\hat{G}(z))z^{p} + (3 - 3\hat{G}(z) + \hat{G}^2(z))}{(z^{p} - 1)^3} F(z) \tag{4.2}$$

When assuming one can design a perfect RC compensator so that $\hat{G} = 1$, the equation is presented as follows

$$\left[\frac{U(z)}{E(z)}\right]_{\text{MPRC}i,\hat{G}=1} = \frac{3z^{2p} - 3z^{p} + 1}{(z^{p} - 1)^3} F(z) \tag{4.3}$$

We now go back to the 3rd order HORC with 3, -3, and 1 as weights, which will now be referred to as HORC throughout the paper with these weight configurations. The same conditions are used for that of the MPRC*i* case where both the cutoff $H(z)$ and RC gain ϕ are set to 1 in Eq. (2.55).

$$\left[\frac{U(z)}{E(z)}\right]_{\text{HORC}} = \frac{3z^{2p} - 3z^{p} + 1}{(z^{p} - 1)^3} F(z) \tag{4.4}$$

Eq. (4-4) is exactly identical to Eq. (4-3) despite having a completely different design structure provided that $H(z)$, ϕ, and $\hat{G}$ are all set equal to 1. Therefore it is clear that MPRC*i* will function so that it increases the robustness to period uncertainties as it was the intent for

HORC. Now it is possible that each method can have different characteristics depending on how the fixed conditions are changed. The study will progress by investigating the ramifications of altering each design parameter.

4.4 COMPARISON ON THE RAMIFICATION OF DECREASING THE GAIN FOR MPRC*i* AND HORC

4.4.1 Stability Robustness to Model Error

For the typical repetitive controller, decreasing the gain will increase stability robustness to model errors. However, this is not always true for the more recently developed repetitive control laws, namely HORC. Maintaining the same conditions so that $H = 1$ and $\hat{G} = 1$, HORC and MPRC*i* will have different stability characteristics when decreasing the RC gain ϕ. The following plots display the stability boundaries with model error in ω_n with respect to different RC gains being used.

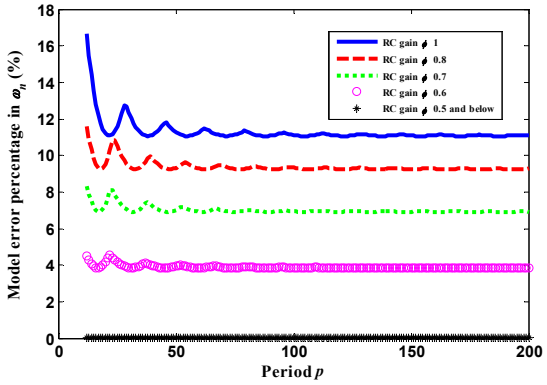

Figure 4-5. Stability boundary plots of HORC with various RC gains

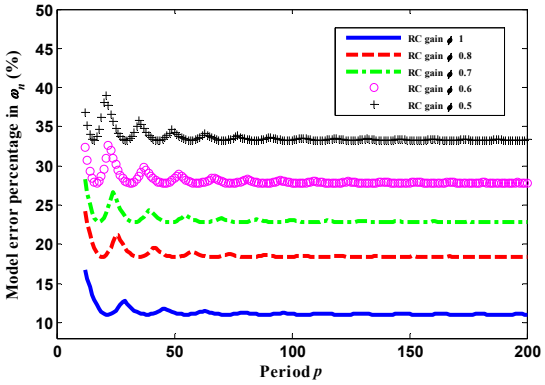

Figure 4-6. Stability boundary plots of MPRC*i* with various RC gains

Oppose to Figure 4-6 of the MPRC*i* case, Figure 4-5 of HORC does not show an increase in stability robustness to model errors when the RC gain is decreased. Instead, HORC decides to become unstable beyond a certain point when decreasing the gain. As previous work related to

HORC demonstrates stability analysis within the frequency domain and root locus methods, a more elaborate explanation is shown here to understand the underlying phenomena of the instability for small gains in HORC.

For better understanding, $P_{N\text{HORC}}(z)$ of Eq. (2.57) with $N = 3$ is divided into two parts such as

$$P_{N\text{HORC}}(z)\big|_{N=3} = A_{3rd}(z)[1-\phi F(z)G(z)]$$
$$A_{3rd} = z^{-3p}[3z^{2p} - 3z^{p} + 1] \tag{4.5}$$

The polar plot of A_{3rd} is depicted below in Figure 4-7.

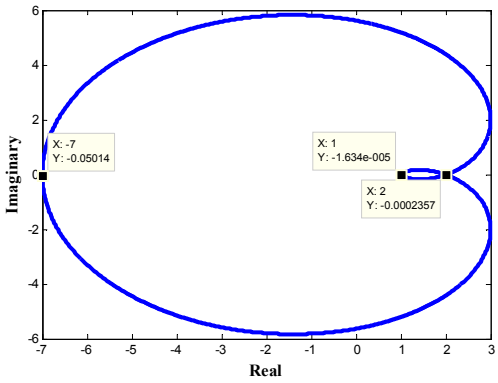

Figure 4-7. Polar plot of A_{3rd} with $p = 40$

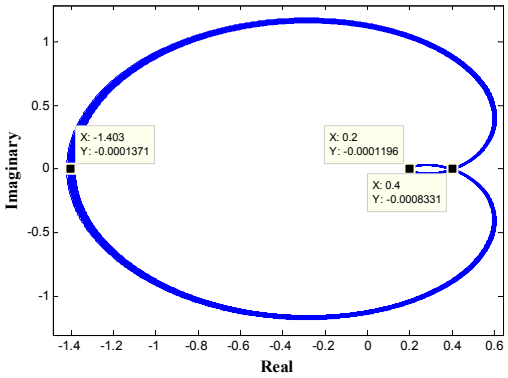

Figure 4-8. Polar plot of $P_{N\text{HORC}}(z)\big|_{N=3}$ with ϕ =0.8

This heart shape plot is maintained for all p's larger than 2 for HORC. Empirical numeric results of the polar plot of A_{3rd} show that increasing p will merely produce duplicated images of the same heart shape shown previously. By using basic triangle inequality relationships we can deduce the magnitude range of A_{3rd} such as

$$1 \le \left|A_{3rd}(z)\right| \le 7 \quad \forall \quad z = e^{i\omega T} \tag{4.6}$$

where this relationship agrees with Figure 4-7. In order to easily understand the implication of reducing the gains of Eq. (4-5), the equation is simplified by making the assumption that the RC compensator $F(z)$ is able to nullify the dynamics of the real world, thus $F(z)G(z)=1$ within the frequency domain. In this case, Eq. (4-5) is simplified to

$$P_{N\text{HORC}}(z)\big|_{N=3,\bar{G}=1} = A_{3rd}(z)[1-\phi] \tag{4.7}$$

which permits a straight forward understanding on how the RC gain influences the stability of HORC. Eq. (4.7) shows the RC gain will merely contribute to the size of the polar plot in Figure 9 while preserving the same heart shape. The idea is demonstrated with a numerical result shown above in Figure 4-8. The polar plot of $P_{N\text{HORC}}(z)\big|_{N=3}$ in Eq. (4-5) is depicted with a 12 gain compensator $F(z)$, in which case $F(z)G(z)\approx 1$, with ϕ = 0.8 and p = 40. According to the simplified Eq. (4-7), the 3 points marked within Figure 4-7 should be mapped onto Figure 10 by multiplying 1-ϕ, which is 0.2. Despite the fact that the compensator does not exactly produce $F(z)G(z)=1$, the relationship given by Eq. (4.7) still roughly holds. Now that the simplified relationship of Eq. (4.7) has been well established, it is easy to estimate that HORC will go unstable when the RC gain is decreased below 0.5.

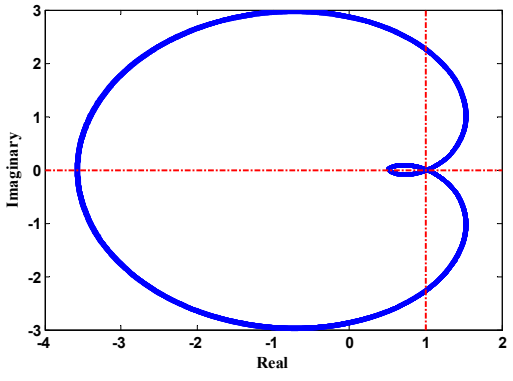

Figure 4-9. Polar plot of $P_{N\text{HORC}}(z)\big|_{N=3}$ with ϕ =0.49

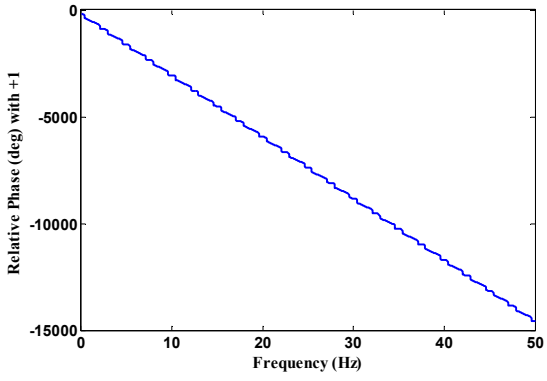

Figure 4-10. Relative Phase with respect to +1

Figure 4-9 above numerically verifies the results by showing an unstable HORC system with ϕ=0.49 and no model error. The phase angle of the polar plot $P_{N\text{HORC}}(z)\big|_{N=3}$ with respect to +1 in Figure 4-10 shows that the phase unravels up to 14400 deg, which means that the polar plot makes 40 encirclements around + 1. This further implies that +1 is located within the small loop of the heart in Figure 4-9.

As observed within the stability boundary plot of Figure 4-6, MPRC*i* increases stability robustness to model errors when reducing the RC gain. This was well explained within previous work by providing numerical results based on frequency domain analysis and also analytical derivation of the small gain stability theory for repetitive control (Ref. [26]). Therefore, it can be said that MPRC can be stabilized by using a sufficiently small gain, opposed to the case of HORC where one must pay attention on how much the RC gain is being reduced.

4.4.2 Increasing the RC Gain Above 1

The previous item investigated stability robust to model error when decreasing the RC gain for HORC. The conclusion was that decreasing the RC gain was in favor of MPRC*i* over HORC in terms of stability. However, the analysis did not see what happens when increasing the RC gain above 1. For typical RC, increasing the gain above 1 would let the control law overcompensate for the error, thus it would not make much sense in doing so. On other hand, this idea of overcompensation is not so straight forward for HORC with negative weights. It is further studied here to see how the stability of HORC responds to increasing the RC gain above 1. The same method is used here by evoking Eq. (4-17). When the RC gain ϕ is larger than 1, the constant term that is multiplied to A_{3rd} in Eq. (4-17) becomes negative. This results in flipping the heart shape plot with respect to its imaginary axis. After the plot has been flipped over, the

magnitude of the constant term will determine the size of the heart shaped plot. Figure 13 shows the polar plot of $P_{NHORC}(z)\big|_{N=3}$ with ϕ = 1.15 for p = 30. By using the same mapping method as the previous item, -7 in Figure 4-7 will be mapped into 1.05 in Figure 4-11, thus encircling +1. Figure 4-12 verifies that the polar plot does indeed encircle +1. Increasing the RC gain more will ensure instability by making the heart shape plot even larger. Therefore, it can be well understood that increasing the RC gain above 1 by only a small amount can make HORC unstable and should not be considered for control design purposes.

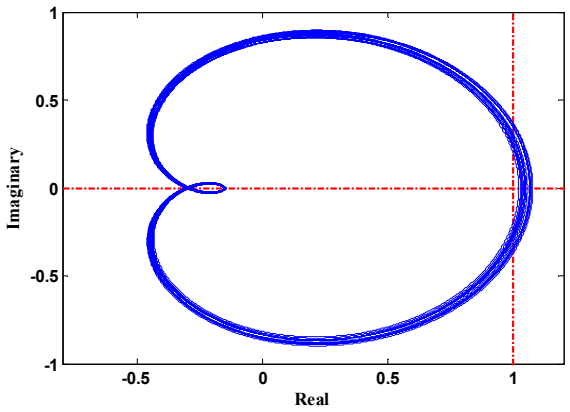

Figure 4-11. Polar plot of $P_{NHORC}(z)\big|_{N=3}$ with ϕ =1.15

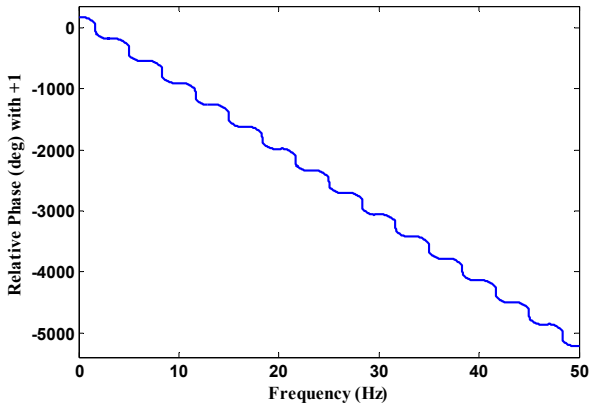

Figure 4-12. Relative Phase with respect to +1

4.4.3 Sensitivity Transfer Function Frequency Response Analysis

Previous work show that by reducing the RC gain within the sensitivity transfer function, the notches located at each frequency being addressed by the repetitive controller will become narrower, thus requiring more accurate information of the period being addressed. On the bright side, due to the waterbed effect, this permits less amplification at the frequency components that are located between the periods being addressed. This has the effect of making the repetitive controller less sensitive to unaddressed frequencies. Previous work shows that the sensitivity

transfer functions for HORC and MPRC have similar characteristics of that of a typical repetitive controller when adjusting the RC gain. It is shown here to better understand how this occurs through frequency response analysis.

The sensitivity transfer function is the relationship between $Y_D(z)-V(z)$ and the error $E(z)$, which is the inverse of the square-bracketed term of Eq. (2.26) for MPRCi. For the sake of simplicity let's assume that the RC compensator $F(z)$ does a good job in nullifying the dynamics of the system so that $\overline{G}=1$ and $\hat{G}=1$. The sensitivity transfer function of MPRCi is simplified as

$$S_{\mathrm{MPRC}i}(z)=\frac{(z^p-1)^3}{(z^p-[1-\phi])^3} \tag{4.8}$$

Notice that the frequency response of Eq. (4.8) will go to zero when ω of $z=e^{i\omega T}$ is equal to the disturbance period being addressed due to the numerator term. Figure 4-13 displays the magnitude of the frequency response of the numerator term of Eq. (4.8). This is also equivalent to the case when ϕ = 1 for Eq. (4.8). It will be shown that this is true for HORC as well later on. Now by simply investigating what is left, it is plausible to think that the denominator term should be responsible for changing the profile of the sensitivity transfer function when reducing the RC gain. When looking at a sensitivity transfer function, it is the magnitude of this term that we are interested in since it is the goal to find out how the profile is reduced or magnified depending on the frequency. The denominator term is isolated from Eq. (4.8) and the magnitude range of the denominator term is determined as

$$\phi^3 \le \left|z^p-[1-\phi]\right|^3 \le (2-\phi)^3 \quad \forall\, z=e^{i\omega T} \tag{4.9}$$

Eq. (4.9) shows that for an RC gain ϕ smaller than 1 the denominator term of Eq. (4.8) will amplify the magnitude of the sensitivity transfer function when the magnitude gets near the lower bound of Eq. (4.9) and will attenuate it near the upper bound. Now, it must be determined at what frequency will the sensitivity transfer function get attenuated or amplified by the upper bound and lower bound magnitudes of the denominator in Eq. (4.9). We first express the period p in terms of frequency, denoted as ω_p, with units of rad/s such as

$$p = \frac{2\pi}{\omega_p T} \tag{4.10}$$

This is substituted into the denominator term of Eq. (4.8) so that the denominator is expressed in terms of frequency.

$$\gamma(\omega) = (e^{2\pi i(\omega/\omega_p)} - 1 + \phi)^3 \tag{4.11}$$

when ω is an integer multiple of the disturbance frequency ω_p, the magnitude of Eq. (4.11), $|\gamma(\omega)|$, is equivalent to the lower bound ϕ^3 of Eq. (4.9). When $\omega = \omega_p(k+1/2), k = 1,2,3\ldots$, which is the frequency between each disturbance frequency component that is being addressed by MPRC*i*, $|\gamma(\omega)|$ is equivalent to the upper bound $(2-\phi)^3$. Therefore when $\phi < 1$, it can be understood that the sensitivity transfer function profile of Eq. (4.8) will get amplified near the addressed frequency component, thus degrading the ability of attenuating the error at neighboring frequencies located near the disturbance period being addressed. On the other hand, in between frequency components of the sensitivity transfer function will be attenuated by the upper bound of the denominator, thus providing less amplification of the error at these frequencies as shown in Figure 4-14.

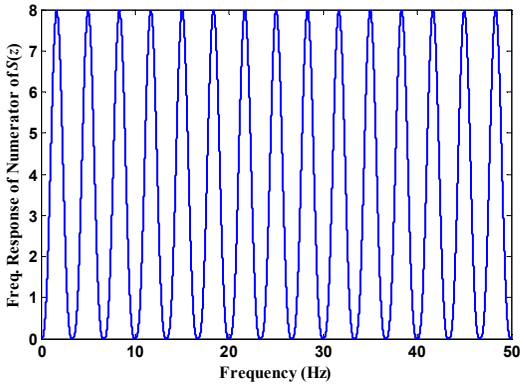

Figure 4-13. Frequency response magnitude of $(z^p-1)^3$

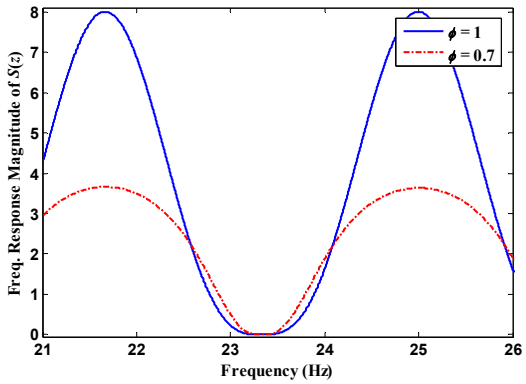

Figure 4-14. Different RC gains used for MPRC*i* addressing multiple identical periods

The effect of the RC gain on the sensitivity transfer function of HORC will be described using a similar approach. The same assumptions are made by setting $F(z)G(z)=1$. The sensitivity transfer function of HORC is simplified to

$$S_{\text{HORC}}(z)=\frac{(z^p-1)^3}{z^{3p}-B_{3rd}[1-\phi]} \qquad (4.12)$$

$$B_{3rd}=3z^{2p}-3z^p+1$$

Notice that only the B_{3rd} term is what makes a difference from the sensitivity transfer function of MPRC*i* in Eq. (4.8). Unfortunately the B_{3rd} makes it less straight forward to derive the magnitude range of the denominator term of Eq. (4.12) using the triangle inequality. From that regard, only the upper bound is calculated for the magnitude range of the denominator term of Eq. (4.12).

$$\left|z^{3p}-B_{3rd}[1-\phi]\right|\le 8-7\phi \qquad (4.13)$$

By using the same approach from Eq. (4.10) and Eq. (4.11), the denominator term of Eq. (4.12) is equal to ϕ when the frequency is an integer multiple of the disturbance frequency being addressed. For frequencies that are located in between the middle of the addressed frequency and associated harmonics, the denominator term equals to $8-7\phi$. With this information alone, one can understand that for any RC gain that is smaller than 1, the sensitivity transfer function of Eq. (4.12) is amplified near the addressed frequencies and attenuated near the frequencies in between the addressed ones. However, this information is insufficient for characterizing the entire frequency response of the sensitivity transfer function of HORC due to the interconnections of the B_{3rd} term and the open bound relationship of Eq. (4.13). This issue will be revisited in the next item. Figure 4-15 shows high peaking side lobes occurring repetitively throughout the frequency response that are a result of the B_{3rd} term. Figure 4-16 shows an enlarged view. It is still under question whether one would want the decreases the RC gain to reduce sensitivity to noise in HORC due to the high peaking side lobes mentioned earlier. This is investigated in later items as well.

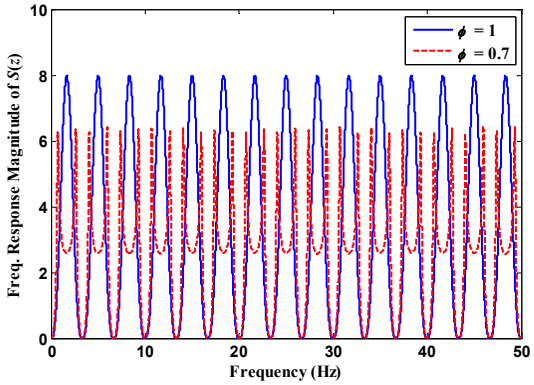

Figure 4-15. Different RC gains used for HORC

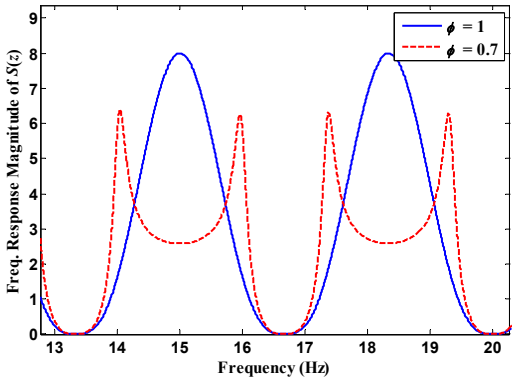

Figure 4-16. Enlarged view of Figure 4-15

4.4.4 Reason for side lobes within sensitivity transfer function plot of HORC when decreasing the RC gain

Previous simulations showed that when the RC gain is decreased, HORC displays high peaking side lobes on each side of the notch of the sensitivity transfer function. A possible cause may be due to the instance where the denominator term of Eq. (4.12) becomes equal to zero for a certain frequency component. The denominator term of Eq. (4.12) is reexamined by setting it to zero such as the following

$$z^{3p} - B_{3rd}[1-\phi] = 0 \tag{4.14}$$

which is further rearranged as

$$z^{-3p} B_{3rd}[1-\phi F(z)G(z)] = 1 \tag{4.15}$$

where the $F(z)G(z)$ has been reinserted into Eq. (4.15) opposed to the case where it was assumed equal to 1. The left hand side of Eq. (4.15) is identical to $P_{N\text{HORC}}(z)\big|_{N=3}$ of Eq. (4.15). This implies that the peak of the side lobes become maximum when $P_{N\text{HORC}}(\omega^*)\big|_{N=3}$ crosses +1 at the frequency component ω^* that is between DC and Nyquist frequency within the polar plot. It also means that the maximum side lobes can occur for an HORC that is marginally stable or unstable. Now let us consider a system with an imperfect compensator where $F(z)G(z)$ does not equal 1. From the stability boundary plot of Figure 4-5, it was shown that regardless of any existing model error that may exist, there will always be a RC gain ϕ that makes HORC marginally stable or unstable. Therefore, for any model error, HORC will have a sensitivity transfer function with high peaking side lobes for a specific RC gain ϕ.

4.4.5 Comparison of the final error level for HORC and MPRCi due to broadband disturbance when decreasing the RC gain

Repetitive control can in theory converge to zero error, provided that one has accurate information on the disturbance period. The benefit of using MPRC*i* and HORC is that the repetitive controller can be less sensitive to period accuracy. Although this may seem as an immediate benefit, previous items show that the error between addressed frequencies will be amplified due to the waterbed effect. One candidate method of trying to reduce this amplification is done by decreasing the RC gain. Both MPRC and HORC show flattening effects on the amplification between addressed frequencies. However, HORC display high-peaking side lobes for each flattened section of the sensitivity transfer function that brings concern with regards to amplifying the error of non-addressed frequencies near these peaks. Optical setups that require precision pointing of laser beams use very sensitive sensors such a position sensing device (PSD). Jitter within a beam can be detected down to the nano-radian level. Within this range of magnitude, broadband disturbance becomes less negligible and can become potential risk for degrading the overall disturbance rejection performance if amplified too much.

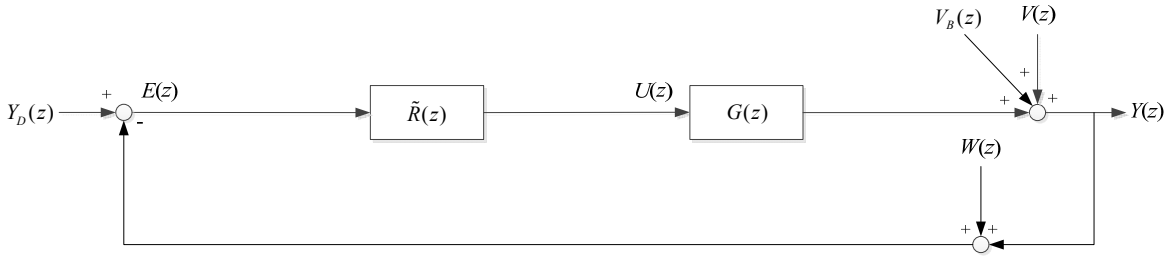

Figure 4-17. Block diagram of a generic RC system $\tilde{R}(z)$ with broadband disturbance and measurement noise

From Figure 4-17 the true error $E_T(z) = Y_D(z) - Y(z)$ can be expressed in terms of the command, the output disturbance, and the measurement noise such as

$$E_T(z) = \tilde{S}(z)[Y_D(z) - V(z) - V_B] + \tilde{S}_w(z)W(z) \quad ; \quad \tilde{S}(z) = \frac{1}{1 + \tilde{R}(z)G(z)} \quad ; \quad \tilde{S}_w(z) = 1 - \tilde{S}(z) \tag{4.16}$$

where $\tilde{S}(z)$ is the generic sensitivity transfer function for a RC system with a generic RC law $\tilde{R}(z)$, $\tilde{S}_w(z)$ is the complementary sensitivity transfer function, and $\tilde{R}(z)$ is either $\hat{R}(z)F(z)$ for MPRC*i* and $R_N(z)\big|_{N=3}$ for HORC within this item. For now let us assume that the narrowband disturbance V and desired output $Y_D(z)$ is zero, and that there is only broadband disturbance V_B to consider. The first term on the right of the first equation of Eq. (4.16) gives the true error due to broadband disturbance and will be studied here. Ref. [29] gives an elaborate explanation on how to calculate the final error level due to disturbance or measurement noise. The formula is evoked here as

$$\sigma_e^2 = \frac{1}{2\pi}\int_0^{2\pi} \sigma_b^2 \tilde{S}(e^{-i\theta})\tilde{S}(e^{i\theta})d\theta \tag{4.17}$$

where the broadband disturbance is white and Gaussian with variance σ_b^2 which is set to unity within the following computation. A numeric simulation is conducted in order to compute the variance of the broadband disturbance amplified by the waterbed effect. Perfect model and perfect compensator assumptions are made so that $\bar{G} = 1$ and $\hat{G} = 1$. Computational results of Eq. (4.17) show that for an RC gain of 0.7, HORC has a covariance of 9.3547, which is 3 time larger than the RMS solely due to the broadband disturbance. MPRC has a covariance of 7.2529, which is slightly smaller than the covariance of HORC using the same RC gain. Despite demonstrating larger efforts of flattening the amplification between addressed frequencies, HORC has larger overall amplification of broadband disturbance due to the high-peaking side lobes as mentioned within previous items. The investigation goes further as the RC gain is tuned

down while calculating the final error level due to broadband disturbance for both HORC and MPRC.

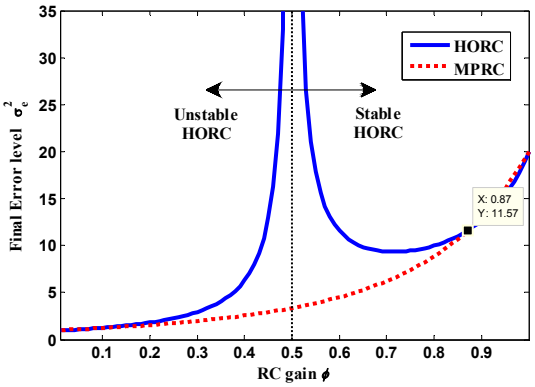

Figure 4-18. Final error due to broadband disturbance

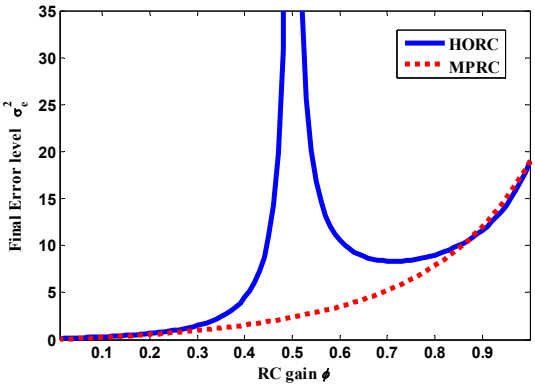

Figure 4-19. Final error due to measurement noise

Figure 4-18 above shows that HORC and MPRC show similar results down to an RC gain of 0.87. However, the final error level tends to increase drastically beyond a certain RC gain for HORC. This is due to the fact that the denominator term of Eq. (4.12) gets close to zero as the RC gain approaches 0.5, which is also when HORC gets close to instability as mentioned within the previous item. Opposed to MPRC*i*, reducing the RC gain in HORC in order to reduce amplification of broadband disturbance is not preferred due to the peaking phenomenon that occurs and the possibility of becoming unstable.

4.4.6 Comparison of the final error level for HORC and MPRC*i* due to measurement noise when decreasing the RC gain

Other than concerns about the broadband disturbance being amplified by the waterbed effect, one may be concerned about sensitivity to measurement noise. From the second term on the right of the first equation of Eq. (4.16), one can calculate the final error level due to measurement noise by the following

$$\sigma_e^2 = \frac{1}{2\pi}\int_0^{2\pi} \sigma_w^2 S_w(e^{-i\theta}) S_w(e^{i\theta}) d\theta \tag{4.18}$$

A numerical simulation is performed with $\hat{G} = 1$, $\overline{G} = 1$, and p = 30. Figure 4-19 above shows that the final error due to measurement noise is not much different from that due to broadband disturbance. The results are further analyzed by looking at the complementary sensitivity transfer functions for both control laws. With the assumption of $\hat{G} = 1$ and $\overline{G} = 1$, the complementary sensitivity transfer functions for respectively HORC and MPRC are

$$S_{w,\mathrm{HORC}}(z) = \frac{B_{3rd}\phi}{z^{3p} - B_{3rd}[1-\phi]} \tag{4.19}$$

and

$$S_{w,\mathrm{MPRC}i}(z) = \frac{3(z^p - 1)^2\phi + 3(z^p - 1)\phi^2 + \phi^3}{(z^p - [1-\phi])^3} \tag{4.20}$$

By observing both equations one is able to see that a smaller RC gain will reduce the frequency response magnitude of the numerator terms for both equations, and therefore it would be desirable to reduce the RC gain if one would want to decrease the error due to noise, provided that the denominator terms do not go to zero for all ϕ's. Now it is obvious that the denominator terms of both Eq. (4.19) and Eq. (4.20) are no different from their respective sensitivity transfer functions. So based on previous analysis of the sensitivity transfer function, the magnitude of the complementary sensitivity transfer function of MPRC will get reduced with a small RC gain shown in Figure 4-20 while this is detrimental to HORC in which case the magnitude can possibly blow up (see Figure 4-21).

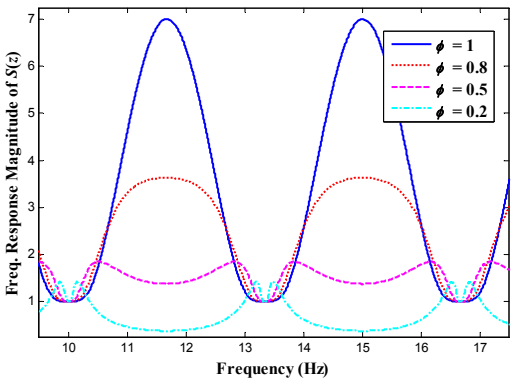

Figure 4-20. Complimentary sensitivity transfer function with various RC gains for MPRC*i* with *p* = 30

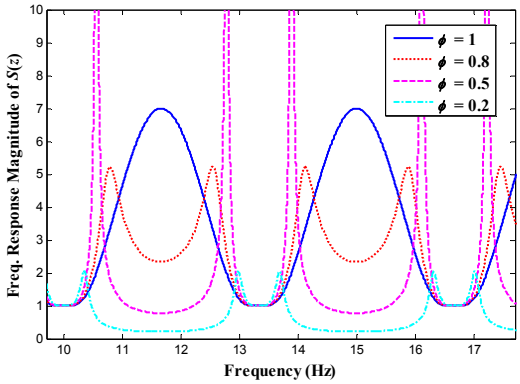

Figure 4-21. Complimentary sensitivity transfer function with various RC gains for HORC with *p* = 30

4.4.7 Comparison of frequency error tolerance for MPRC*i* and HORC when decreasing the RC gain

In previous items it has been shown that the slopes around each notch within the sensitivity transfer function get narrower as the RC gain decreases. One may want to know how each method gets less tolerant to deviation errors from the actual disturbance frequency and the frequency addressed by each control law when reducing the RC gain. A numeric simulation is conducted with $\hat{G}=1$ and $\overline{G}=1$. The frequency error tolerance is calculated to have at least a factor of 10000 error reduction. Past experiments on the NPS's TAS2 addressed optical jitter due to CMG induced vibration. The jitter was correlated to the rotor speed of the CMG, which was around 33 to 35 Hz. Numeric errors prevailed due to non-integer number of time steps corresponding to the true speed of the rotor, in which case resulted in having deviation error from the addressed and real disturbance frequency. The simulation here will address a 33.3 Hz disturbance signal with a 100 Hz sample rate for simplicity.

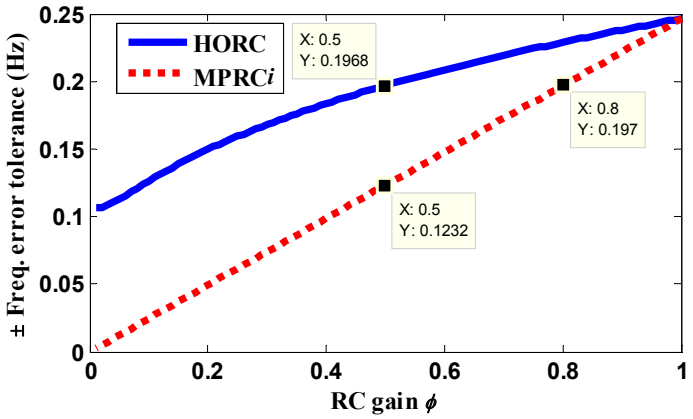

Figure 4-22. Frequency error tolerance for HORC and MPRC*i* with respect to decreasing RC gain

Figure 4-22 above shows that HORC can tolerate more frequency error than that of MPRC*i* as the RC gain gets smaller. However, it must be taken into account that HORC will become unstable beyond an RC gain of 0.5. Disregarding any error due to the measurement noise and broadband disturbance, for an RC gain of 0.5 the HORC is in favor of frequency error tolerance over MPRC by a relatively small amount of 0.073 Hz when addressing a 33.3 Hz disturbance signal. Nevertheless, the choice of an RC gain of 0.5 is unfeasible for a system where measurement noise and broadband disturbance is non-negligible due to massive amplifications of these errors, and destroys a major purpose of decreasing the RC gain. Although HORC compared to MPRC can cope with more frequency error when reducing the RC gain within the stable range, it is somewhat of a tricky task to idealize the performance when one needs to be concerned about becoming unstable or increasing the error due to broadband disturbance or noise. From a short range of an RC gain of 1 down to 0.87, based on Figure 4-19 HORC can tolerate more frequency error and amplify less error due to measurement and broadband disturbance, and the designer may be tempted to fine tune the performance within this short range. However, the difference of final error level due to noise for the two methods is meager

and no method shows significant advantage over the other within this short range. Above all, it is important to understand the uncertainties of the disturbance period by trying to define the variation range when deciding what controller to use.

When the frequency uncertainty variation is well-defined and not as large, MPRC*i* has the upper hand by being able to fine tune the performance so that the narrowband frequency is within range of the desired reduction and that the final error level due to noise is minimized. Figure 4-23 below shows that MPRC*i* with a RC gain of 0.1 can tolerate more frequency error and is able to amplify less error between the addressed frequencies, when compared to single period RC with a gain of 1 (see enlarged view in Figure 4-24). It is meaningless to compare with the HORC case, as it becomes unstable for a RC gain 0.1.

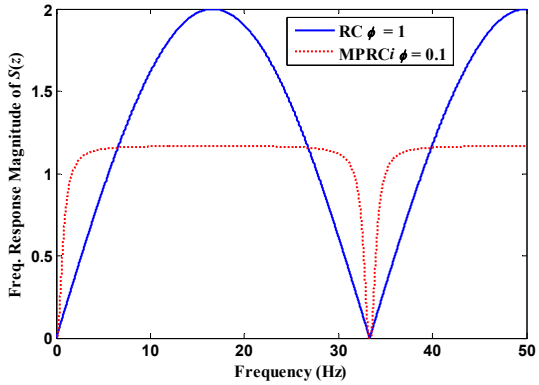

Figure 4-23. Sensitivity transfer function of RC and MPRC*i*

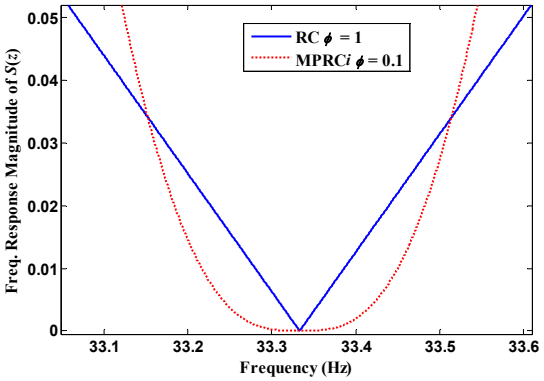

Figure 4-24. Enlarged view of Figure 4-23

The benefit of MPRC*i* is that error between the addressed frequencies can be flattened while preserving frequency error tolerant features such as Figure 4-24. A bonus to reducing the RC gain for MPRC*i* is that the stability robustness to model errors increases. From that regard HORC is not able to provide such capabilities due to instability for small gains. In Figure 4-22 it

shows that MPRC*i* is able to tolerate ± 0.025 Hz frequency error while via numeric simulation the single period RC could only tolerate $\pm 5.3\text{e-}004$ Hz despite having larger amplifications in error at unaddressed frequencies. In hardware, MPRC*i* is capable of achieving ideal performance by turning down the RC gain as the error is observed from the data. HORC on the other hand would not be preferable for this method due to instabilities that can occur when the RC gain is decreased too much.

4.5 WIDENING THE NOTCH FURTHER WITHOUT INCREASING THE ORDER OF RC

MPRC*i* and HORC with 3, -3, and 1 as weights aim for zero error at the addressed frequency component and a small portion of the neighboring frequencies as well due to the notch widening effect of these methods. In order to increase the width of each notch, one may increase the order of the repetitive controller such as addressing more identical periods for MPRC*i* or by increasing the order of HORC more than 3. However, this method can increase the computational effort significantly and result in making real-time control a challenge. Another issue arises from previous studies where it has been shown that introducing more repetitive controllers can decrease the stability robustness to model errors substantially. An alternative to this approach is introduced here for each respective RC method. By choosing different weights, 3rd order HORC has the ability to increase the width of each notch within the sensitivity transfer function by paying for less attenuation at the neighboring frequencies. One choice of weights for further widening these notches for 3rd order HORC is 2.93, -2.93, and 1. Figure 4-25 shows the magnitude of the sensitivity transfer function with the chosen weights where $p = 20$, $F(z)G(z) = 1$, $\phi = 1$, and the sample rate is 100 Hz. The fundamental frequency and associated harmonics are equally widened and uniformly spaced. Figure 4-26 shows an enlarged view of Figure 4-25

to show that HORC with 2.93, -2.93, and 1 weights no longer aims for zero error at the neighboring frequencies due to the effort of further widening the notch. The previous (3, -3, 1) weight set for HORC is plotted also for comparison. One can play with these weights to adjust the width of the notches. However, if widened too much, the error reduction will be less aggressive within the neighboring frequencies of the widened notch. MPRC is also able to imitate such effects by addressing the fundamental period and two periods that are spaced one time step back and forth from the fundamental. Figure 4-25 shows that MPRC has similar features to that of HORC where small bumps are formulated on each side of the fundamental frequency being addressed. The height of each bump determines the weakened capability of error reduction within the widened notch. Despite having similar characteristics occurring at the fundamental period, it is easy to see that for the case of MPRC, the notch widening effects disappear as the order of the harmonics get higher. This is due to the fact that the period spacing becomes larger as the harmonics get higher. Therefore, it can be said that HORC has the upper hand over MPRC when further widening the notch without increasing the order of RC.

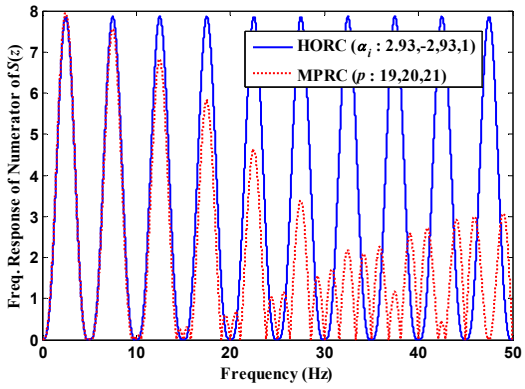

Figure 4-25. Sensitivity transfer function of RC and MPRC*i*

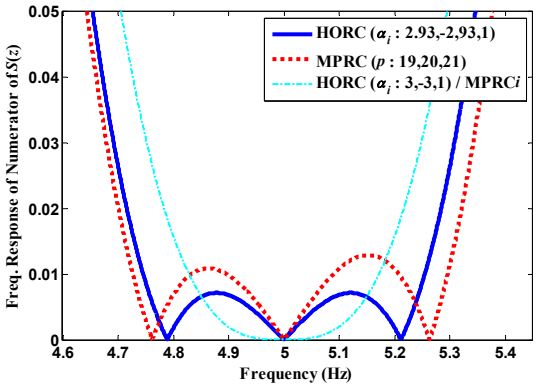

Figure 4-26. Enlarged view of Figure 4-25 with HORC (3,-3,1)

4.6 COMPUTATIONAL DIFFERENCES IN LOW PASS FILTER IMPLEMENTATION

In RC practice a low pass filter implementation is essential for preventing instabilities that may be due to unmodeled high frequency dynamics and model errors. One pays for this stability by not being able to address frequency components beyond the cutoff of the low pass filter. By achieving the same task MPRC*i* will need to implement five identical low pass filters *H* while HORC only needs to implement one. In other words MPRC*i* needs five times more multiplications and additions than that of the HORC to complete the cutoff of learning. A popular choice for *H* is to use 51 gains. In result MPRC*i* is required to compute 255 additions and multiplications within 1 time step for the low pass filter alone. NPS's TAS2 was able to execute MPRC*i* in real-time with a sample rate of 5 kHz. In result the cost of computation did not give rise to any concerns with regards to this matter.

4.7 INCORPORATING THE TWO CONTROL LAWS INTO MPRC

The typical MPRC addresses multiple unrelated periods and their respective harmonics. The tolerance for each uncertainty within the period being addressed will be the same of that of a single period RC law. Therefore MPRC for its typical use will be able to tolerate very little period uncertainty. Inspired by MPRC*i*, one may incorporate HORC or MPRC*i* into MPRC so that the tolerance of period uncertainty is increased for each unrelated period being addressed. The design structure is the same as Figure 2-2 with the exception of replacing R_j's within the block diagram with $\hat{R}(z)\big|_{\text{MPRC}i}$ of Eq. (2.22) for MPRC*i* and $[F(z)]^{-1}R_N(z)\big|_{N=3}$ for HORC. The following will describe how to determine stability for the incorporated methods and then compare the sensitivity transfer function profiles resulting from decreasing the RC gain.

4.7.1 Nonstandard Nyquist Criterion for Stability for incorporated HORC

The stability criterion for MPRC has been established in previous items. In order to directly utilize this pre-established equation for HORC incorporated into MPRC, Eq. (10) with $N = 3$ and (3, -3, 1) as the weights is expressed as

$$F(z)R_{\text{HORC}}(z) = F(z)\frac{\phi_j B_j}{z^{3p_j} - B_j} \quad , \quad B_j = H_j[3z^{2p_j} - 3z^{p_j} + 1] \tag{4.21}$$

where $F(z)$ is pulled out front of the equation. The formality of this equation is similar to that of a single period RC law within the first equation of Eq. (2.20). Due to this similarity it is possible to replace H_j and z^{p_j} of Eq. (2.20) respectively with B_j and z^{3p_j} of Eq. (4.21) to obtain the stability criterion for HORC incorporated into MPRC. The same rules apply by determining stability depending on the encirclement of the point -1 within the polar plot of interest.

4.7.2 Nonstandard Nyquist Criterion for Stability for incorporated MPRC*i*

MPRC does not have the convenience of being packaged into the formality of the single period RC design structure. The result of this is that the stability criterion cannot be deduced in a simple manner such as the HORC case. The full equation will not be derived here. Instead, one will assume $\hat{G} = 1$ so that the equation can be simplified. Taking into account that one has a perfect compensator for MPRC*i* incorporated into MPRC, the discrete representation of the control law $\hat{R}(z)\big|_{\text{MPRC}i}$ is expressed as

$$R_{\text{MPRC}i3} = [(R_1 + 1)(R_2 + 1)(R_3 + 1)]^3 - 1 \tag{4.21}$$

for 3-period MPRC*i* and

$$R_{\text{MPRC}i2} = [(R_1 + 1)(R_2 + 1)(R_3 + 1)]^2 - 1 \tag{4.22}$$

for 2-period MPRC*i* where R_j (j = 1, 2, 3) is defined within the first equation of Eq. (2.22). Based on this simplified control law the characteristic polynomial is rearranged into the form where the $3(p_1 + p_2 + p_3)$ roots on the unit circle of the original equation is removed. We can write this polynomial in the form

$$\begin{aligned} &z^{-3(p_1+p_2+p_3)}\left\{(B_{\mathrm{MPRC}i})^3 + 3A_{\mathrm{MPRC}i}(B_{\mathrm{MPRC}i})^2 + 3(A_{\mathrm{MPRC}i})^2 B_{\mathrm{MPRC}i}\right\}\bar{G} - 3C_{\mathrm{MPRC}i} + 3(C_{\mathrm{MPRC}i})^2 - (C_{\mathrm{MPRC}i})^3 = -1 \\ &P_{\mathrm{MPRC}i3} = -1 \end{aligned} \tag{4.23}$$

$$\begin{aligned} &A_{\mathrm{MPRC}i} = (z^{p_1} - H_1)(z^{p_2} - H_2)(z^{p_3} - H_3) \\ &B_{\mathrm{MPRC}i} = [(z^{p_1} - H_1)(z^{p_2} - H_2)\phi_3 H_3 + (z^{p_2} - H_2)(z^{p_3} - H_3)\phi_1 H_1 + (z^{p_3} - H_3)(z^{p_1} - H_1)\phi_2 H_2] \\ &\ldots + [(z^{p_1} - H_1)\phi_2\phi_3 H_2 H_3 + (z^{p_2} - H_2)\phi_3\phi_1 H_3 H_1 + (z^{p_3} - H_3)\phi_1\phi_2 H_1 H_2] + \phi_1\phi_2\phi_3 H_1 H_2 H_3 \\ &C_{\mathrm{MPRC}i} = (z^{-p_1} H_1 + z^{-p_2} H_2 + z^{-p_3} H_3) - (z^{-p_1-p_2} H_1 H_2 + z^{-p_2-p_3} H_2 H_3 + z^{-p_3-p_1} H_3 H_1) + z^{-p_1-p_2-p_3} H_1 H_2 H_3 \end{aligned} \tag{4.24}$$

for 3-period MPRC*i* incorporated into MPRC and

$$\begin{aligned} &z^{-2(p_1+p_2+p_3)}\left\{(B_{\mathrm{MPRC}i})^2 + 2A_{\mathrm{MPRC}i}B_{\mathrm{MPRC}i}\right\}\bar{G} - 2C_{\mathrm{MPRC}i} + (C_{\mathrm{MPRC}i})^2 = -1 \\ &P_{\mathrm{MPRC}i2} = -1 \end{aligned} \tag{4.25}$$

for 2-period MPRC*i* incorporated into MPRC. Given the periods, a necessary and sufficient condition for asymptotic stability of each case is that the $P_{\mathrm{MPRC}i3}(z)$ image or $P_{\mathrm{MPRC}i2}(z)$ image of the unit circle $z = e^{i\omega T}$ does not encircle the point -1.

4.7.3 Instability due to decreasing the RC gain

Previous items showed stability analyses of both HORC and MPRC*i*. The former method would become unstable with decreasing the RC gain opposed to the latter case in which the model error stability robustness was increased. It is investigated within this item whether this is true for the incorporated methods through numeric simulations.

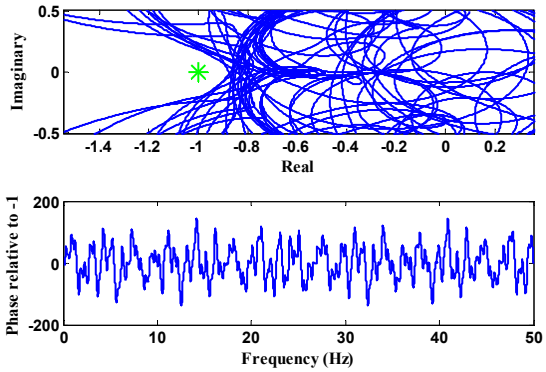

Figure 4-27. HORC incorporated into MPRC, RC gain = 0.8

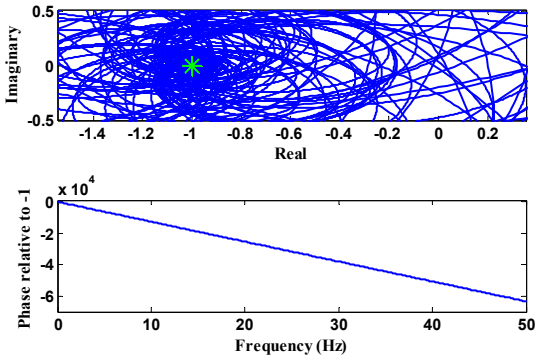

Figure 4-28. HORC incorporated into MPRC, RC gain = 0.4

The nonstandard Nyquist plots of HORC incorporated into MPRC were depicted based on the assumption of $\hat{G}=1$ and $\bar{G}=1$, while addressing the periods, 30, 45, and 101. Figure 4-27 and Figure 4-28 show similar results to that of the HORC case where the system becomes unstable when the RC gain is tuned down beyond a certain value. Although it will not be further determined whether this relationship can be proven analytically, it is plausible to think so based on the fact that HORC alone has such characteristics. MPRC*i* incorporated into MPRC is essentially MPRC with more periods being addressed. Therefore the incorporated method for MPRC will be asymptotically stable for a small enough RC gain ϕ. This can be shown by applying the small gain stability theory for RC to the characteristic equation of Eq. (4.23) or Eq. (4.25) for the 3-period and 2-period case respectively. The derivation will not be shown here.

4.7.4 Sensitivity transfer function for incorporated HORC

The motivation of incorporating HORC into MPRC is to increase the robustness of disturbance period uncertainties for each period being addressed by MPRC. As expected, Figure 4-29 and Figure 4-30 shows that the sensitivity transfer function increases the notch feature of each frequency being addressed, which are 0.99, 2.22, and 3.33 Hz.

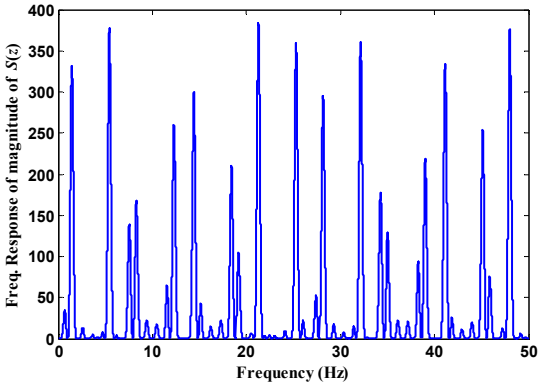

Figure 4-29. Sensitivity transfer function of HORC incorporated into MPRC

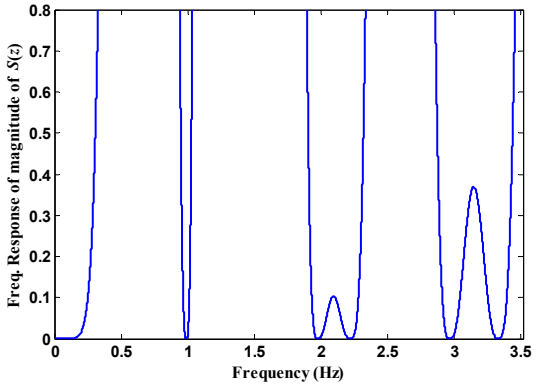

Figure 4-30. Enlarged view of Figure 4-29

One can decrease the RC gain and expect the same result of that of the HORC case where sensitivity to unaddressed frequencies and noise can be reduced. However, due to the fact that decreasing the RC gain has the possibility of harming the stability of this control law, one may be reluctant to reducing the RC gain for any reason. Instead, it may be more intriguing to fine tune the gain of MPRC*i* incorporated into MPRC to be less concerned of stability issues.

4.7.5 Sensitivity transfer function for incorporated MPRC*i*

MPRC*i* incorporated into MPRC is basically MPRC addressing multiple frequencies where some of which are identical to each other. As it is already a given fact that MPRC abides by the rules of the small gain stability theorem, MPRC will be asymptotically stable for a small enough RC gain chosen by the designer. This gives the advantage of worrying less about stability issues while fine tuning the performance in terms of noise and unaddressed frequency amplification matters. As shown in both Figure 4-31 and Figure 4-32, the functionality of decreasing the gains is straight forward without any concerns of any high peaking phenomenon that may occur.

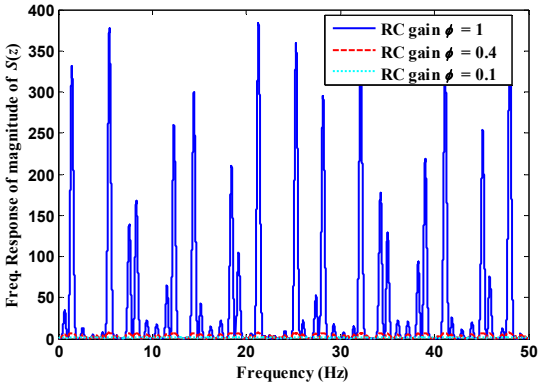

Figure 4-31. Sensitivity transfer function of MPRCi incorporated into MPRC

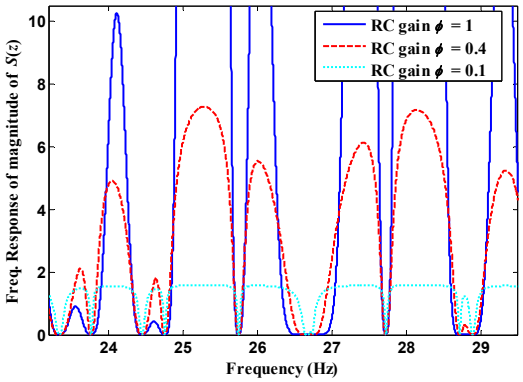

Figure 4-32. Enlarged view of Figure 4-31

4.8 NOTCH WIDENING EFFECTS FOR OTHER CONTROL LAWS

A previous publication evaluated five different candidate control algorithms for addressing optical jitter on a spacecraft testbed. One of the five which is called Matched basis function repetitive control (MBFRC) showed similar results to that of MPRC when addressing identical periods. The notch widening effect within the sensitivity transfer function is investigated here with regards to MBFRC when addressing multiple identical disturbance periods. In addition to MBFRC, Model predictive control (MPC) is also studied to see if such characteristics exist when addressing same periods as well.

4.8.1 Notch widening effects in MBFRC

Instead of addressing all frequencies of a given period, MBFRC individually addresses each frequency. One form finds the error components at these addressed frequencies using the projection algorithm of adaptive control. It uses only frequency response knowledge at addressed frequencies to eliminate error at these frequencies. Frequency domain raising produces an equivalent time invariant pole/zero model of the control law for each frequency addressed

$$T_n(z) = (a_n / r_n)\frac{[\cos(\phi_n - \tau_n)z^2 - 2\cos(\tau_n)z + \cos(\phi_n + \tau_n)]z}{[z^2 + (a_n - 2)\cos(\phi_n)z + (1 - a_n)][z^2 - 2\cos(\phi_n)z + 1]} \qquad n = 1, 2, 3, \ldots, N \quad (4.26)$$

Here ϕ_n is the angle in the complex plane associated with the frequency being addresses (with 180 deg corresponding to Nyquist), r_n and τ_n are the magnitude and phase response at this frequency, and a_n is a gain chosen between 0 and 2 associated with convergence of the projection algorithm. Figure 4-33 gives the structure of the control system for addressing *N* frequencies. The Φ and the λ_n are gains, and it can be proved that for sufficiently small gains one is guaranteed convergence to zero error (see Ref. [30]). As in MPRC one makes use of knowledge of the disturbance period, and this approach avoids either interpolation or approximation of the disturbance periods as an integer number of time steps, as needed in MPRC.

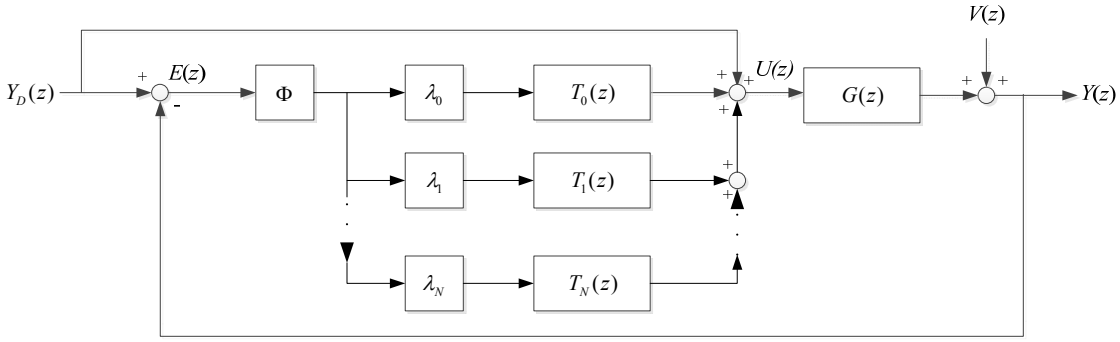

Figure 4-33. Control scheme for match basis function repetitive control

Previous experiments on the TAS2 showed that MBFRC would have better disturbance rejection capabilities in the presence of disturbance uncertainties when addressing three identical periods. In order to verify whether this is true for MBFRC in general, we investigate the notch widening effects by analyzing the sensitivity transfer functions of MBFRC.

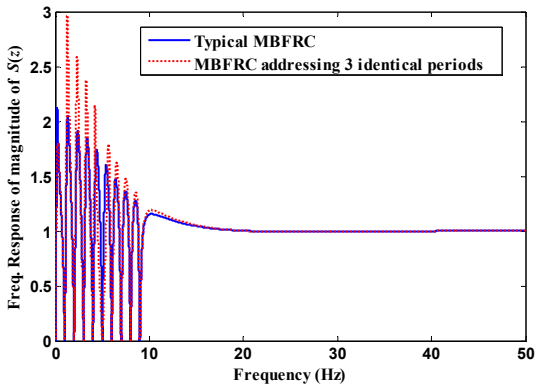

Figure 4-34. Sensitivity transfer function of two cases of MBFRC

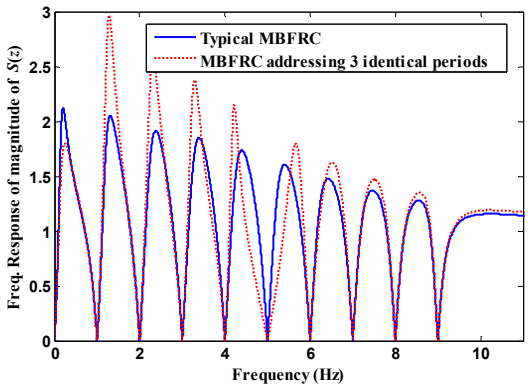

Figure 4-35. Enlarged view of Figure 4-34

A simulation is performed by comparing the sensitivity transfer functions of MBFRC addressing 10 evenly spaced frequency components starting from 0 to 9 Hz. Among the two sensitivity transfer functions one of which is redundantly addressing the 5 Hz frequency component by three times. The gain Φ is set to 0.01 for both cases. In Figure 3-34 and Figure 3-35 the sensitivity transfer function displays a widening at the 5Hz-notch where the frequency component is being redundantly addressed. The notch is widened in a sense that the narrowness of the valley has decreased and therefore permits more error attenuation when the true disturbance is slightly deviating from the addressed frequency than that of the typical MBFRC case. In order to gain some intuition on how this is possible a mathematical explanation is provided within the following.

For the sake of simplify with regards to the math of the sensitivity transfer function of MBFRC, we assume that there are no plant dynamics, thus r_n and τ_n equal 1. a_n = 1 as well and there is only one frequency component being addressed. The sensitivity transfer function is now expressed as

$$S_{MBFRC,N} = \frac{[z-\cos(\phi)](z-e^{j\phi})(z-e^{-j\phi})}{[z-\cos(\phi)](z-e^{j\phi})(z-e^{-j\phi}) + N[\cos(\phi)z^2 - 2z + \cos(\phi)]} \tag{4.27}$$

where N refers to the number of times the frequency component ϕ is being redundantly addressed. In order to see how N affects the magnitude of Eq. (4.27) near the addressed frequency component, we substitute z of Eq. (4.27) with $e^{j\phi}$ to obtain $-2jN\sin^2(\phi)e^{j\phi}$, which is the resulting denominator term of Eq. (4.27) at the addressed frequency component. The magnitude of the denominator of Eq. (4.27) is $2N\sin^2(\phi)$ at this frequency. This gives some information that increasing N will decrease the magnitude of $S_{MBFRC,N}$ near the addressed frequency component and therefore having a less narrow valley within the sensitivity transfer function.

4.8.2 Notch widening effects in MPC

Previous publications show that there are several ways of implementing Model predictive control (MPC) (see Ref. [31]). Only one of which will be used here to explain the notch widening effects of MPC. In the case where one has only disturbance corrupted data, one can create a system model

$$\sum_{i=0}^{n+2f+n_d} \alpha_i y(k-i) = \sum_{i=1}^{n+2f+n_d} \beta_i u(k-i) \tag{4.28}$$

with the disturbance information embedded within the equation. In Eq. (4.28) n refers to the order of the disturbance free model, f refers to the number of expected frequency components, and n_d equals zero when there is no disturbance at DC or at Nyquist frequency. Eq. (4.28) is further reformulated into a predictive control model such as the example below.

$$\begin{bmatrix} \alpha_0 & 0 & 0 & 0 \\ \alpha_1 & \alpha_0 & 0 & 0 \\ \alpha_2 & \alpha_1 & \alpha_0 & 0 \\ \alpha_3 & \alpha_2 & \alpha_1 & \alpha_0 \end{bmatrix} \begin{bmatrix} y(k+1) \\ y(k+2) \\ y(k+3) \\ y(k+4) \end{bmatrix}_F = \begin{bmatrix} 0 & \beta_3 & \beta_2 \\ 0 & 0 & \beta_3 \\ 0 & 0 & 0 \\ 0 & 0 & 0 \end{bmatrix} \begin{bmatrix} u(k-3) \\ u(k-2) \\ u(k-1) \end{bmatrix}_P - \begin{bmatrix} \alpha_3 & \alpha_2 & \alpha_1 \\ 0 & \alpha_3 & \alpha_2 \\ 0 & 0 & \alpha_3 \\ 0 & 0 & 0 \end{bmatrix} \begin{bmatrix} y(k-2) \\ y(k-1) \\ y(k) \end{bmatrix}_P + \begin{bmatrix} \beta_1 & 0 & 0 & 0 \\ \beta_2 & \beta_1 & 0 & 0 \\ \beta_3 & \beta_2 & \beta_1 & 0 \\ 0 & \beta_3 & \beta_2 & \beta_1 \end{bmatrix} \begin{bmatrix} u(k) \\ u(k+1) \\ u(k+2) \\ u(k+3) \end{bmatrix}_F \tag{4.29}$$

The above Eq. (4.29) is the predictive control model for a 3rd order disturbance embedded system model, where $n + 2f + n_d = 3$ within Eq. (4.29). The predictive model is formulated so that the u input and y output terms are separately packaged with respect to 4 future terms with a subscript denoted as F and 3 past terms with a subscript denoted as P. Premultiplying by the inverse of the coefficient matrix on the left produces a model of the following form, giving the future output as a function of past command inputs, past output, and future command inputs.

$$y_{F,s}(k) = P_1 u_{P,p}(k) - P_2 y_{P,p} + W u_{F,s}(k) \tag{4.30}$$

where

$$P_1 = \begin{bmatrix} \alpha_0 & 0 & 0 & 0 \\ \alpha_1 & \alpha_0 & 0 & 0 \\ \alpha_2 & \alpha_1 & \alpha_0 & 0 \\ \alpha_3 & \alpha_2 & \alpha_1 & \alpha_0 \end{bmatrix}^{-1} \begin{bmatrix} 0 & \beta_3 & \beta_2 \\ 0 & 0 & \beta_3 \\ 0 & 0 & 0 \\ 0 & 0 & 0 \end{bmatrix} \quad P_2 = \begin{bmatrix} \alpha_0 & 0 & 0 & 0 \\ \alpha_1 & \alpha_0 & 0 & 0 \\ \alpha_2 & \alpha_1 & \alpha_0 & 0 \\ \alpha_3 & \alpha_2 & \alpha_1 & \alpha_0 \end{bmatrix}^{-1} \begin{bmatrix} \alpha_3 & \alpha_2 & \alpha_1 \\ 0 & \alpha_3 & \alpha_2 \\ 0 & 0 & \alpha_3 \\ 0 & 0 & 0 \end{bmatrix} \quad W = \begin{bmatrix} \alpha_0 & 0 & 0 & 0 \\ \alpha_1 & \alpha_0 & 0 & 0 \\ \alpha_2 & \alpha_1 & \alpha_0 & 0 \\ \alpha_3 & \alpha_2 & \alpha_1 & \alpha_0 \end{bmatrix}^{-1} \begin{bmatrix} \beta_1 & 0 & 0 & 0 \\ \beta_2 & \beta_1 & 0 & 0 \\ \beta_3 & \beta_2 & \beta_1 & 0 \\ 0 & \beta_3 & \beta_2 & \beta_1 \end{bmatrix} \tag{4.31}$$

and

$$y_{F,s}(k) = \begin{bmatrix} y(k+1) \\ y(k+2) \\ \vdots \\ y(k+s) \end{bmatrix} \quad u_{P,p}(k) = \begin{bmatrix} u(k-p) \\ u(k-p+1) \\ \vdots \\ u(k-1) \end{bmatrix} \quad y_{P,p} = \begin{bmatrix} y(k-p+1) \\ y(k-p+2) \\ \vdots \\ y(k) \end{bmatrix} \quad u_{F,s}(k) = \begin{bmatrix} u(k) \\ u(k+1) \\ \vdots \\ u(k+s-1) \end{bmatrix} \tag{4.32}$$

$s = 4$ and $p = 3$ for Eq. (4.29). Linear model predictive control generates the set of inputs from the current time to the end of the prediction horizon in order to minimize the quadratic cost function over this time interval

$$J(k) = \left[y_{F,s}(k) \right]^T Q y_{F,s}(k) + \left[u_{F,s}(k) \right]^T R u_{F,s}(k) \tag{4.33}$$

For a recursively adapting scheme only the first time step of this result is applied to the system, and the process is then repeated each time step. Substituting Eq. (4.30) into Eq. (4.33) and then minimizing with respect to $u_{F,s}(k)$ yields,

$$\begin{gathered} u_{F,s}(k) = A_1 u_{P,p}(k) + A_2 y_{P,p}(k) \\ A_1 = -BP_1 \qquad A_2 = BP_2 \qquad B = (R + W^T Q W)^+ W^T Q \end{gathered} \tag{4.34}$$

and the + superscript denotes the pseudo-inverse. Since only the first time step of this result is applied, the MPC controller is an IIR filter for the control action at time step *k* that can be written as

$$u(k) = \sum_{i=1}^{p-1} G_i u(k-i) + \sum_{i=0}^{p-1} H_i y(k-i) \tag{4.35}$$

where the G_i and H_i gains come from the first row of A_1 and A_2 respectively for a single input single output system.

Previous investigations showed that when there the broadband disturbance is large compared to the narrowband disturbance that needs to be annihilated, the MPC controller would have trouble accurately identifying the disturbance period. If one were to have information of the narrowband disturbance frequency prior to this identification procedure, it would be possible to

address this issue by artificially embedding the narrowband disturbance redundantly into the disturbance embedded system model of Eq. (4.28) such as

$$[z^2 - 2\cos(\omega_1 T)z + 1]^N \sum_{i=0}^{n+2f+n_d} \alpha_i y(k-i) = [z^2 - 2\cos(\omega_1 T)z + 1]^N \sum_{i=1}^{n+2f+n_d} \beta_i u(k-i) \qquad (4.36)$$

where N is the number of times the frequency component of interest is being addressed. After Eq. (4.36) is rearranged into the ARX model form such as Eq. (4.28), the MPC IIR filter can be produced by sequentially following Eq. (4.29) through Eq. (4.35). A numeric simulation is conducted that shows the notch widening effects of MPC when same frequencies are addressed multiple times (See Figure 4-36 and Figure 4-37). 10, 25, and 40 Hz are addressed by MPC for one case while the other addresses the same periods with the 25 Hz component addressed 3 times. The plant is a 3rd order model with 100 Hz sampling rate.

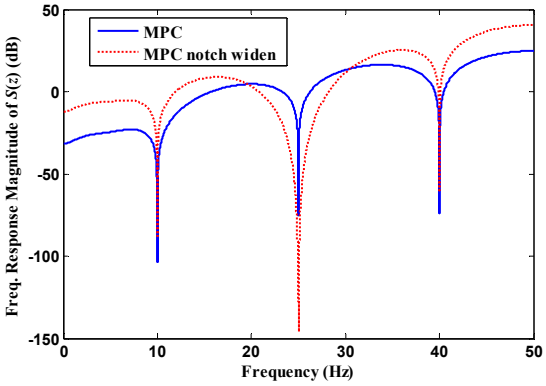

Figure 4-36. Sensitivity transfer function MPC showing notch widening effect at 25 Hz in Log. Scale

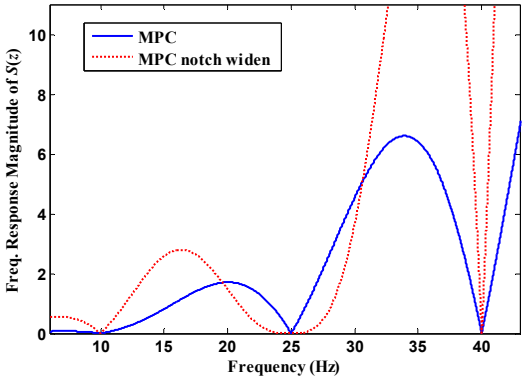

Figure 4-37. Sensitivity transfer function MPC showing notch widening effect at 25 Hz

Therefore one is able to widen the notch of the sensitivity transfer function of MPC by artificially embedding disturbance information into the disturbance embedded system model of Eq. (4.28).

4.9 CONCLUSIONS

It was shown that when MPRC was implemented to address multiple periods that were identical, the transfer function representation was identical to that of HORC provided that the RC gain was set equal 1, there was no cutoff filter used, and a perfect RC compensator was used for nullifying the dynamics of the plant model such as $\hat{G} = 1$. This specific configuration of periods with MPRC was referred to as MPRC*i*, which produced robustness to period fluctuations. A comparison between the two methods was made changing the fixed condition, namely the RC gain ϕ. Emphasis was given to reducing the final error level.

4.9.1 Stability

When decreasing the RC gain HORC would go unstable with a small enough gain. MPRC*i* on the other hand would have an increase in robustness to model error due to the small gain stability theory. Increasing the RC gain above 1 would induce instability for both methods.

4.9.2 Sensitivity Transfer Function Profile

When decreasing the RC gain MPRC*i* would show similar characteristics to that of the single-period case where the unaddressed frequencies would get smaller by paying for more sensitivity with regards to accurateness of periods being addressed. However, HORC would have high peaking side lobes within the range of unaddressed frequencies before becoming unstable. These high peaking side lobes can severely amplify errors that are within range of these.

4.9.3 Final Error Level due to Broadband Disturbance and Measurement Noise

The final error level of HORC due to broadband disturbance and measurement noise can be severely amplified by high peaking side lobes within the sensitivity transfer function for a small

enough RC gain. MPRC*i* on other hand can fully use the capabilities of reducing sensitivity to noise and broadband disturbance by fine tuning the RC gain. For short range of decreasing the RC gain from 1, HORC is capable of amplifying less error due to measurement noise and broadband disturbance when compared to MPRC*i*. However, this value is not at significant and can be considered negligible.

4.9.4 Frequency Error Tolerance

For a given RC gain, HORC is slightly more tolerant to period uncertainties than that of MPRC*i*. Nevertheless, simulation results show that this advantage is not significant. Due to stability matters, MPRC*i* is exclusively capable of fine tuning the RC gain in hardware so that ideal performance is achieved by monitoring the error level in data.

4.9.5 Widening the Notch Further without Increasing the Order

HORC has the ability to widen the notch further by simply changing the configuration of weights and by paying for less attenuation near the neighboring frequencies of the addressed ones. MPRC is capable of mimicking such performance by spreading the addressing periods apart by a certain amount of time steps. However, MPRC fails to do this for harmonics.

4.9.6 Low Pass Filter Implementation

Using a cutoff filter is considered essential for real situations in implementing RC. Due to the difference in the design structure for both methods, MPRC*i* requires five more cutoff filters than that of HORC. Nevertheless, previous experiments showed that today's computers had no trouble with processing MPRC*i* in real time despite having a fast sample rate of 5 kHz.

4.9.7 Incorporating into MPRC

It was shown that both HORC and MPRC*i* could be incorporated into MPRC in order to address unrelated periods while increasing the robustness to period uncertainties. Simulation results showed that the incorporated-HORC would go unstable for a small enough RC gain. From that regard, incorporated-MPRCi would be stable due to the small gain stability theory. Incorporated- MPRCi is also exclusively capable of fine tuning the RC gain to achieve ideal performance.

4.9.8 Other Control Algorithms

MBFRC and MPC both showed notch widening characteristics within their respective sensitivity transfer function when the periods were addressed redundantly.

CHAPTER 5

ADDRESSING BAD TRANSIENTS WITHIN STARTUP OF MULTIPLE-PERIOD REPETITIVE CONTROL

5.1 INTRODUCTION

The previous chapter has shown that MPRC*i* can be used to widen the notch of multiple frequencies. This is ideal for situations where there are multitudes of frequency content within the disturbance with some degree of period uncertainties. The width of each notch within the sensitivity transfer function, which is the transfer function of disturbance to error, can be adjusted by the Repetitive controller gain until the designer can find the ideal gain that produces the best error mitigation performance. However, experimental results from Reference [28] show a sudden jump within the early stage of the transient response when implementing MPRC*i* shown in Figure 5-1. The startup issue observed is different from other startup issues with repeating high frequency images within the response of single-period RC (see Ref. [32], [33]). The purpose of this chapter is to investigate the cause of bad transients when implementing MPRC*i*, and then find a method to resolve the issue. Further investigation will show similar issues can be found in MPRC when addressed periods are close together.

5.2 HIGH PEAKS WITHIN THE TRANSIENTS OF MPRC WHEN ADDRESSING IDENTICAL PERIODS

MPRC*i* is a special configuration of MPRC where the Repetitive controller addresses multiple identical periods. A hypothesis is made here that the size of the peak would differ depending on how these periods are spread apart from each other. An algorithm was developed so that the sum of the three periods being addressed would be fixed to the value 120. The periods are then randomly distributed within this fixed sum. For each set of randomly distributed periods a

numerical simulation was performed by addressing these periods with MPRC. For simplicity we assume that the plant has no dynamics. Figure 16 shows the standard deviation of the three periods and the associated normalized peak, which is the ratio between the maximum value transient peak and the maximum value disturbance peak, within the transients of the response. The plot shows a trend that implies that the normalized peak increases as the three periods are close together. By paying close attention to Figure 5-2 one can notice that the normalized peak is at its maximum when all periods are the same. The investigation goes further by increasing the number of periods being addressed by MPRC*i* via numerical simulation.

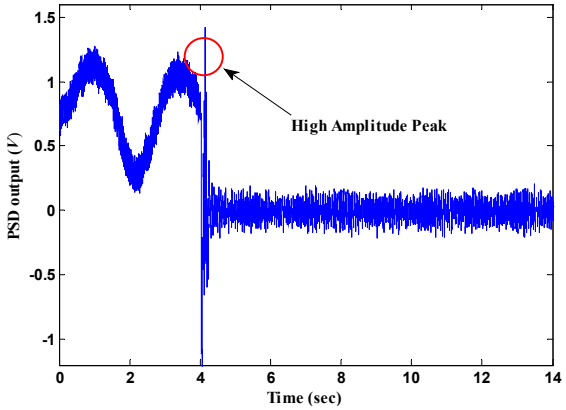

Figure 5-1. High amplitude peaks within the transient from Reference 4

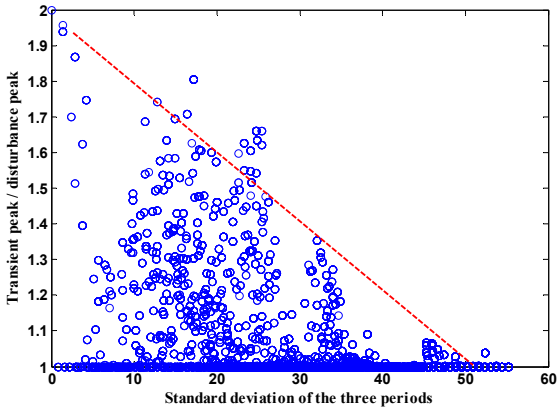

Figure 5-2. 10000 samples for the normalized peak in 3-period MPRC

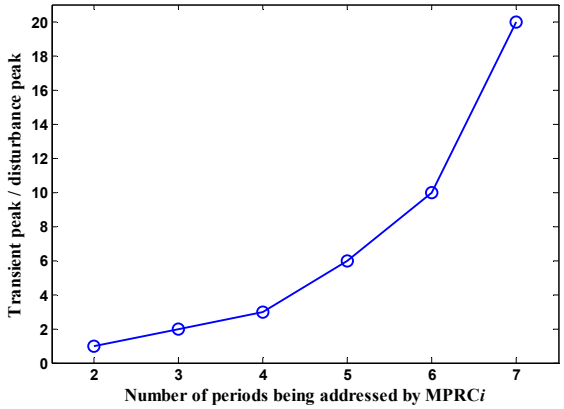

Figure 5-3. Normalized peak as a function of the number periods being addressed by MPRC*i*

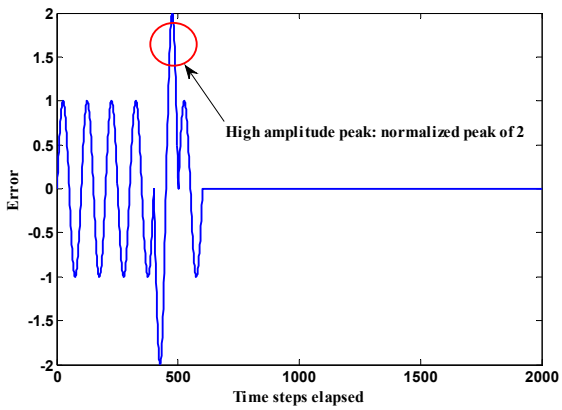

Figure 5-4. Numerical simulation of 3-period MPRC*i* addressing 1 Hz

Figure 5-3 verifies that the peaks get larger as more periods are addressed in MPRC*i*. This can be an issue when the transient peak is larger than the saturating limits of the hardware actuator. The MPRC system can go unstable due to the nonlinearities introduced to the system.

5.2.1 Reason for High Peaks within the Transients of MPRC*i*

It is certain that MPRC will have high amplitude peaks within its transient response when addressing multiple identical periods. Figure 5-4 shows the response of a numerical simulation of MPRC*i* addressing a 1 Hz disturbance. The plant dynamics are discarded within the simulation for simplicity. The plot shows a noticeable peak that is twice the size of the original disturbance. The phenomenon is investigated in detail by analyzing the 3-period MPRC*i* case.

The block diagram of MPRC is shown in Figure 2-1 where the design parameters have been selected so that $R_n(z) = 1/[z^{p_n} - 1]$, $F(z) = 1$, $G(z) = 1$ and $\hat{G}(z) = F(z)G(z) = 1$ for simplicity. The parameters each represent the Repetitive Control (RC) law for each period being addressed, RC compensator, and the true world respectively. These parameters have been specifically chosen for a true world with no dynamics or unit transfer function plant. For real applications the dynamics of the plant exist and design methods of Reference [8] are needed for MPRC implementation. With the selected design parameters, each transfer function block in Figure 2-1 can assume the basic difference equation form $\tilde{u}(k) = \tilde{u}(k-p) + \phi e(k-p)$. The Repetitive controller has to wait at least p time steps before it is turned on. When the controller is initiated at time step k_i each transfer function block within the diagram is turned on synchronously. Since $\tilde{u}$ for each block is zero for all samples that exist prior to time step k_i, each transfer function block will output a signal that is equivalent to $\phi e(k-p)$ from k_i to k_i+p-1 time steps. Due to the fact that each control block looks p time steps into the past, the two interconnecting blocks such

as $R_1\hat{G}$ and $R_2\hat{G}$ will not be able to contribute to the error being fed into R_2F and R_3F during the first period, which is from k_i to k_i+p-1. Therefore only the three control blocks R_1F, R_2F, and R_3F will contribute to the adjusted command $U(z)$ during the first period after the control law was turned on. As mentioned previously the three control blocks will output the same signal $\phi e(k-p)$ for the first period. Thus, $u(k) = 3\phi e(k-p) = -3\phi v(k-p)$ where $v(k)$ is the disturbance signal. The resulting output during the first period of control action is $y(k) = [1-3\phi]v(k-p)$ and $y(k)\big|_{\phi=1} = -2v(k-p)$ when ϕ = 1. The result is characterized as an overcompensation of the error as each control law tries to address the disturbance independently during the first period of control action. This explains the factor of two amplification and reversed sign observed in Figure 5-4. One can expect that changing the periods slightly different from each other will not drastically change the peak value. Figure 5-2 implies that this is true by showing that the peak value is still high when the peaks are close to one another. In conclusion, the MPRC addressing periods that are identical or close to each other have a high possibility of saturating the hardware actuator when one wants to increase the number of addressed frequencies.

5.2.2 The Effect of DC Offset within the Error

Analogous to having high peaks within the transient response, the DC bias within the error can be overcompensated as well due to the structure of MPRC. In order to understand the phenomenon we isolate the DC component from the error within the difference equation of the three control blocks R_1F, R_2F, and R_3F such as $\tilde{u}(k+p) = \tilde{u}(k) + \phi e_s(k) + \phi e_{DC}(k)$ where $e_s(k)$ and $e_{DC}(k)$ are the periodic error and DC bias respectively. It can be well understood that the

$e_{DC}(k)$ component will be overcompensated by the same logic as the previous case. Figure 5-5 shows overcompensation due to both the sinusoidal component and DC component of the error. Due to this phenomenon it would be reasonable to have a closed-loop feedback law that addresses bias within the error before applying an MPRC law addressing multiple identical periods.

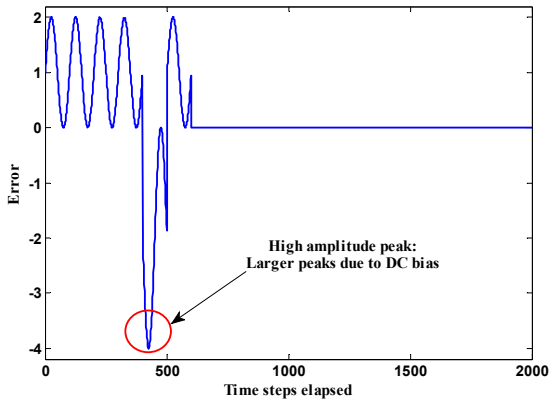

Figure 5-5. MPRC*i* with DC bias of 1

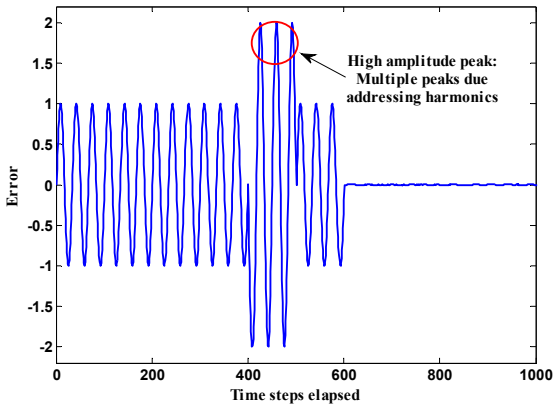

Figure 5-6. MPRC*i* addressing 2nd harmonic

5.2.3 Having Multiple High Peaks when Addressing Harmonics

From the previous items it was determined that overcompensation of the error would occur during the time the MPRC law was first turned on until p time steps after. In cases where harmonics exist within the disturbance signal, the error recorded by each individual controller of the MPRC law would contain multiple peaks depending on the order of the harmonics. As the adjusted command is outputted these peaks will be overcompensated as well causing multiple high peaking within the transient response. The number of peaks is equal to the order of the harmonic + 1. Figure 5-6 shows MPRC*i* addressing the 2nd harmonic of 1 Hz.

5.3 ADDRESSING THE ISSUE OF HIGH AMPLITUDE TRANSIENTS WITHIN MPRC

High peaks within the beginning of Repetitive control action can saturate the actuator limit of the hardware causing instabilities. The following item will discuss how this issue can be avoided when implementing MPRC*i*.

5.3.1 Decreasing the Repetitive control gain

The simplest approach is to decrease the Repetitive control (RC) gain within the MPRC law. The decreased gain will scale down the error so that the adjusted command during the first period $u(k) = -3\phi v(k-p)$ will not overcompensate for the error. The tradeoff is that one must pay for a slower learning rate to get rid of the peak. The results addressing a 1 Hz disturbance signal is shown in Figure 5-7. Although this might be a bit discouraging in terms of achieving maximum convergence rate, real world applications are prone to have model errors which warrant the need for decreasing the RC gain to stabilize the controller (Ref. [26]). Another good reason for decreasing the RC gain is for reducing the amplification of unaddressed frequencies due to the waterbed effect in presence of broadband disturbance.

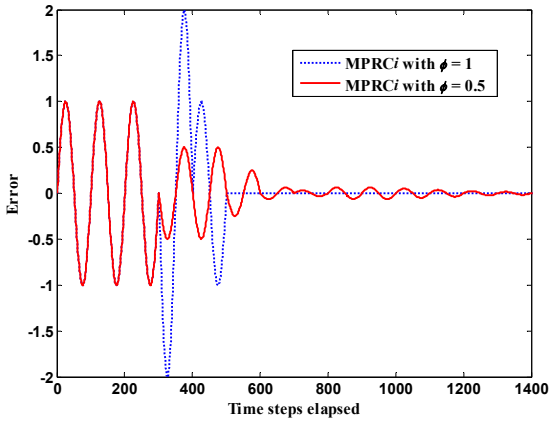

Figure 5-7. Decreasing the RC gain to get rid of the peak

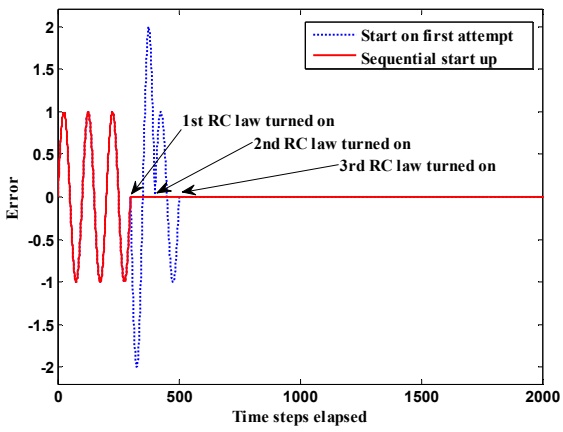

Figure 5-8. Sequentially turning on each individual RC law within MPRC*i*

5.3.2 Sequential start for each individual RC law

The previous item explains how the control blocks within Figure 2-2 overcompensate for the error. Instead of implementing each control block on first attempt, the individual RC laws can be turned on p_i, which is the period of previously implemented control law, time steps after the previous RC law was turned on. This will indeed prevent overcompensation of error, but there is concern that this may extend the time required to converge when compared to implementing all individual RC laws on first attempt. Figure 5-8 shows deadbeat like response when sequentially turning on each individual RC law. Since the error is already addressed when the first RC law is turned on, the convergence time is not delayed at all and actually faster than starting on first attempt. The investigation is progressed by slightly changing the periods being addressed to 93, 90, and 87 with RC gain equal to 1.

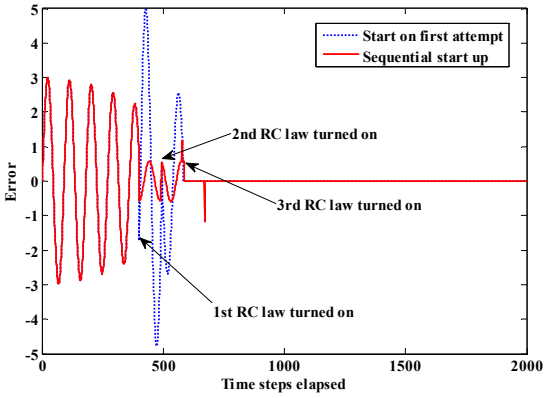

Figure 5-9. Sequential start up for periods 93, 90, and 87 with ϕ = 1

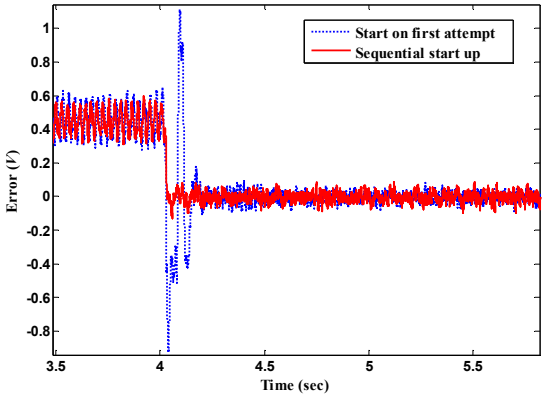

Figure 5-10. Sequential start up for 3-period MPRC addressing 35.5 Hz CMG induced jitter

Figure 5-9 shows a comparison of turning on the individual RC laws on first attempt and the new sequential method. The sequential method addresses the period starting from the largest to smallest. According to the results the method of sequentially turning on each individual RC law is very effective when periods are close to each other. The time delay due to the sequential turn

on process is almost negligible. Although it is not shown here there is no need to employ the sequential method when periods are spread far apart since the high amplitude peak naturally diminishes. Figure 5-10 shows experimental results with the TAS2 using 3-period MPRC*i* while the CMG's are turned on, but without the testbed floating. The sequential method eliminates the overcompensation that occurred when starting at first attempt. Going back to the previous example shown in Figure 5-9, it is important that the periods should be addressed starting from the highest period to the lowest period. The reason for this originates from the basic concept that each individual RC block during the first period will output a signal that is equal to the error one period back or $e(k-p)$. If the previous RC block was addressing a shorter period than that of the current RC block, the error that is learned by the current RC block will contain jump discontinuities that was created when the output signal of the previous RC block was applied to the adjusted command $U(z)$.

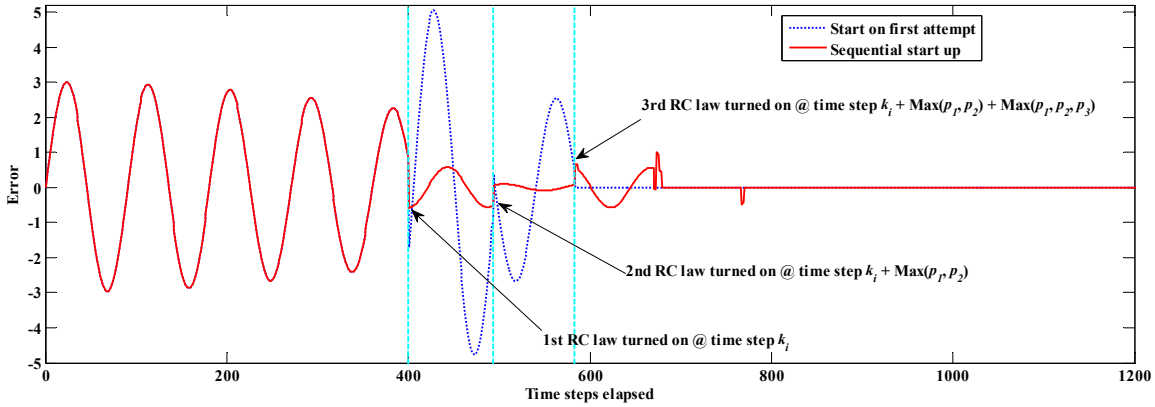

Figure 5-11. Mitigating jump discontinuities by delaying start up of each RC law

Another method is proposed here that is less sensitive to the specific order of the periods being sequentially addressed by paying for more time to converge. The first RC law starts at an arbitrary time step k_i. The second RC law, which includes the interconnecting block, is turned on

at $k_i + \max(p_1, p_2)$. The third RC law is turned on at $k_i + \max(p_1, p_2) + \max(p_1, p_{2,} p_3)$. This method reduces jump discontinuities within the output signal by avoiding learning during the adjustments made by the previous individual RC laws within the design structure. Figure 5-11 shows a more detailed view addressing the same disturbance given within Figure 5-9.

5.4 CONCLUSIONS

MPRC shows high peaks within its transient response when addressing identical periods and periods that are close together. This phenomenon occurs when each individual RC law within the MPRC structure is turned on at first attempt. In order to remedy the issue a sequential method of turning on each individual RC law was introduced and was shown to be very effective by completely eliminating the high peak within the transient response.

CHAPTER 6

EVALUATION OF FIVE CONTROL ALGORITHMS FOR ADDRESSING CONTROL MOMENT GYROSCOPE INDUCED JITTER ON A SPACECRAFT TESTBED

6.1 INTRODUCTION

Spacecraft very often experience problems with jitter. It is usually produced by reaction wheels or control moment gyros (CMGs) that serve as actuators for the attitude control systems, but can be due to other sources such as a momentum wheel, or a cryogenic pump. Jitter can compromise the performance of fine pointing equipment on board, and one can try to use passive vibration isolation techniques to address this problem. Active control methods specifically designed to use knowledge of the periodic nature of the disturbance can produce better performance. In some applications one mounts the fine pointing equipment on an active isolation mount such as a Stewart platform to apply active control methods, as treated in Ref. [34]. A new class of applications relates to the new communications technology of laser communications relay (LCR) that has substantial advantages over radio frequency (RF) systems. The precise laser pointing requirements challenges the acquisition, tracking, and pointing (ATP) technologies. But the jitter suppression can replace the complexity of a 6 degree-of-freedom Stewart platform with a much simpler pan and tilt control of a fast steering mirror (FSM). It is the purpose of this paper to perform experimental implementations of 5 different candidate control methods for addressing the jitter rejection problem, in order to obtain insight into the characteristics, issues, and performance of each method in hardware applications.

The Adaptive Optics Center of Excellence of Naval Postgraduate School (NPS) Three-Axis Simulator 2 (TAS2) testbed is a spacecraft simulator designed for developing and validating ATP technologies for the Bifocal Relay Mirror Spacecraft (BRMS) whose concept is shown in Figure 6-1 (Refs. [35], [36], [37], [38], [39], [40]). Two optically coupled telescopes on the spacecraft are used to relay a laser source from the ground/air/space to a target point on the earth or in space. CMGs are the primary source of jitter, and experiments are performed with the CMGs running but without floating the testbed on its air bearing, and also with it floated. An active attitude control system is then in operation to maintain the spacecraft attitude, making use of the CMG actuators. Attitude sensing makes use of a star tracker, and special techniques are needed to adjust the star tracker information to account for the short distance of the spacecraft to the star images appearing on the ceiling of the laboratory. The following sections will briefly describes each of the 5 candidate jitter control algorithms.

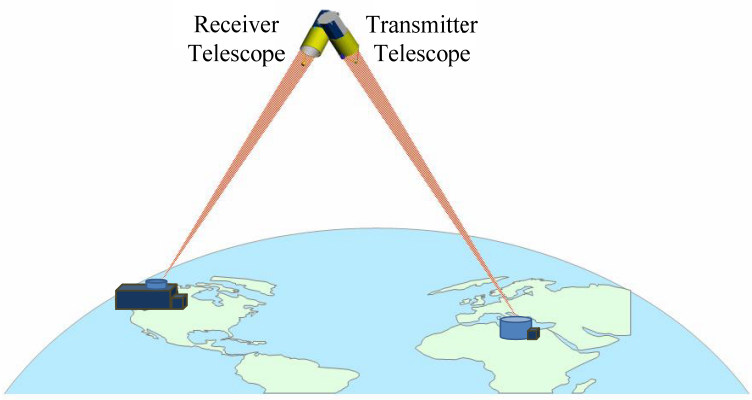

Figure 6-1. Concept of BRMS

6.2 FIVE CANDIDATE CONTROL ALGORITHMS FOR JITTER SUPPRESSION

6.2.1 Multiple-Period Repetitive Control and Matched Basis Function Repetitive Control

Multiple-Period Repetitive Control (MPRC) was explained in detail in chapter 2. Matched Basis Function Repetitive Control (MBFRC) was briefly explained in section 4.7.1 of chapter 4. In terms of the end result of each algorithm, MBFRC can selectively address a frequency component that does not necessarily have to be an integer number in terms of samples (Refs [41], [42]). MPRC on other hand requires that the period being addressed to be an integer number of samples without an interpolator and addresses all harmonics of the fundamental until the learning is cutoff by a low pass filter.

6.2.2 Adaptive Filtered-X LMS Algorithm

Figure 6-2 presents the block diagram structure (Refs. [11], [28], [34], [43]). A feedback approach to Filtered-X LMS (XLMS) estimates the correlated disturbance source signal from feedback information by subtracting the estimated plant output from the measured error. The filtered-X method gets its name by passing the reference signal through an IIR filter plant model in order to adjust the phase of the compensating command signal in anticipation of the phase lag it will experience going through the true world plant. The LMS (Least Mean Square) algorithm uses a stochastic gradient-descent approach, to successively minimize a cost function representing the mean square error such as the following.

$$J(k) = E[e^2(k)] = E[(d(k) - \mathbf{w}^T(k)\mathbf{x}(k))^T (d(k) - \mathbf{w}^T(k)\mathbf{x}(k))]$$

$$= E[(d^2(k)] - 2\mathbf{p}^T(k)\mathbf{w}(k) + \mathbf{w}^T(k)\mathbf{R}(k)\mathbf{w}(k) \tag{6.1}$$

$$= \underbrace{E[(d^2(k)] - \mathbf{p}^T(k)\mathbf{R}^{-1}(k)\mathbf{p}(k)}_{\text{Independant of weights } \mathbf{w}} + \underbrace{(\mathbf{w}(k) - \mathbf{R}^{-1}(k)\mathbf{p}(k))^T \mathbf{R}(k)(\mathbf{w}(k) - \mathbf{R}^{-1}(k)\mathbf{p}(k))}_{\text{Quadratic function of weights } \mathbf{w}}$$

where $\mathbf{p}(k) = E[d(k)\mathbf{x}(k)]$ is the cross-correlation vector and $\mathbf{R}(k) = E[\mathbf{x}(k)\mathbf{x}^T(k)]$ is the auto correlation matrix. The stochastic approach calculates the gradient of the cost as an attempt to minimize it with respect to the weights $\mathbf{w}(k)$

$$-\nabla J(k) = 2\mathbf{p}(k) - 2\mathbf{R}(k)\mathbf{w}(k) \tag{6.2}$$

The two terms $\mathbf{R}(k) \approx \mathbf{x}(k)\mathbf{x}^T(k)$ and $\mathbf{p}(k) \approx \mathbf{x}(k)d(k)$ are estimated by using the current time step values.

$$\begin{aligned} -\nabla J(k) &= 2\mathbf{x}(k)d(k) - 2\mathbf{x}^T(k)\mathbf{x}(k)\mathbf{w}(k) \\ &= 2\mathbf{x}(k)[d(k) - \mathbf{x}(k)\mathbf{w}(k)] \\ &= 2\mathbf{x}(k)e(k) \end{aligned} \tag{6.3}$$

This results in updating the weights of an FIR filer according to

$$\mathbf{w}(k+1) = \mathbf{w}(k) + \mu\mathbf{x}(k)e(k) \tag{6.4}$$

where the $\mathbf{w}$ is the weight vector, $\mathbf{x}$ is the reference signal vector with length equal to number of weights, and μ is the adaptive step gain. In order to produce the ARX plant model, system identification of the plant is required. XLMS does not require any information of the disturbance prior to implementing the control algorithm. This can be an advantage when the disturbance is poorly known or varies, but when there is good knowledge there is a potential for improved performance when this knowledge is incorporated in the algorithm.

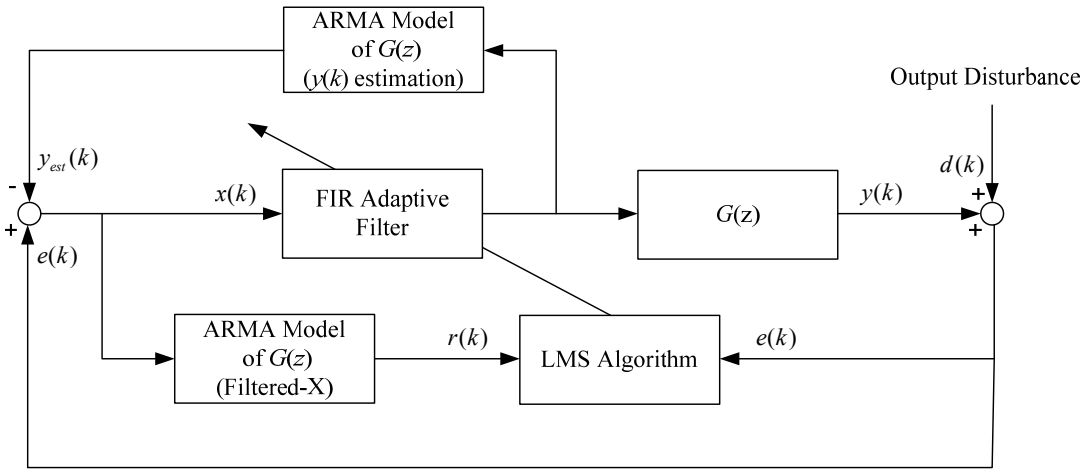

Figure 6-2. Feedback type Filtered-X LMS Algorithm control scheme

6.2.3 Model Predictive Control

Linear model predictive control uses a system model of the form (Ref. 13-15)

$$y_s(k+q) = P_1 u_p(k-p) - P_2 y_p(k-p) + W u_{s+q}(k) \tag{6.5}$$

Such a model can be produced from a state space model, or an ARX model (with a vector solution variable in the case of multiple outputs), or one can use input/output data to directly identify coefficients in the model of Eq. (6.5) to fit the data. The y_s, y_p, u_{s+q}, u_p are super vectors, for example, $y_s(k+q)$ contains all outputs at time steps from the beginning of the prediction horizon for the current step *k*, that is step $k+q$, to the end of the prediction horizon, for a total of *s* time steps of output. The *y* refer to output, the *u* to inputs, and the subscript *p* refers to vectors associated with past time steps. Linear model predictive control (MPC) plans the set of inputs from the current time to the end of the prediction horizon in order to minimize the quadratic cost function over this time interval

$$J(k) = \left[y_s(k+q) \right]^T Q y_s(k+q) + \left[u_{s+q}(k) \right]^T R u_{s+q}(k) \tag{6.6}$$

Then only the first time step of this result is applied to the system, and the process is then repeated each time step. Substituting Eq. (6.5) into Eq. (6.6) and then minimizing with respect to $u_{s+q}(k)$ yields,

$$\begin{gathered} u_{s+q}(k) = A_1 u_p(k-q) + A_2 y_p(k-q) \\ A_1 = -BP_1 \qquad A_2 = BP_2 \qquad B = (R + W^T Q W)^+ W^T Q \end{gathered} \tag{6.7}$$

and the + superscript denotes the pseudo-inverse. Since only the first time step of this result is applied the MPC controller is an IIR filter for the control action at time step *k* that can be written as

$$u(k) = \sum_{i=1}^{p} G_i u(k-i) + \sum_{i=1}^{p} H_i y(k-i) \tag{6.8}$$

where the G_i and H_i gains come from the first *r* rows of A_1 and A_2 respectively for an *r*-input, *m*-output MIMO system. The implementation used here uses a real time adaptation of the coefficients in Eq. (6.5) using an LMS descent. Equation (6.6) requires a pseudo inverse whose size depends on the prediction horizon. If needed, one can update the coefficients in Eq. (6.5) less frequently than every time step. To start the control, one needs to produce rich input data for the initial identification. MPC can produce high order control laws, and it is possible that the controller transfer function fails to be stable while the feedback system is stable. Figure 6-3 presents the block diagram structure of an adaptive scheme for MPC.

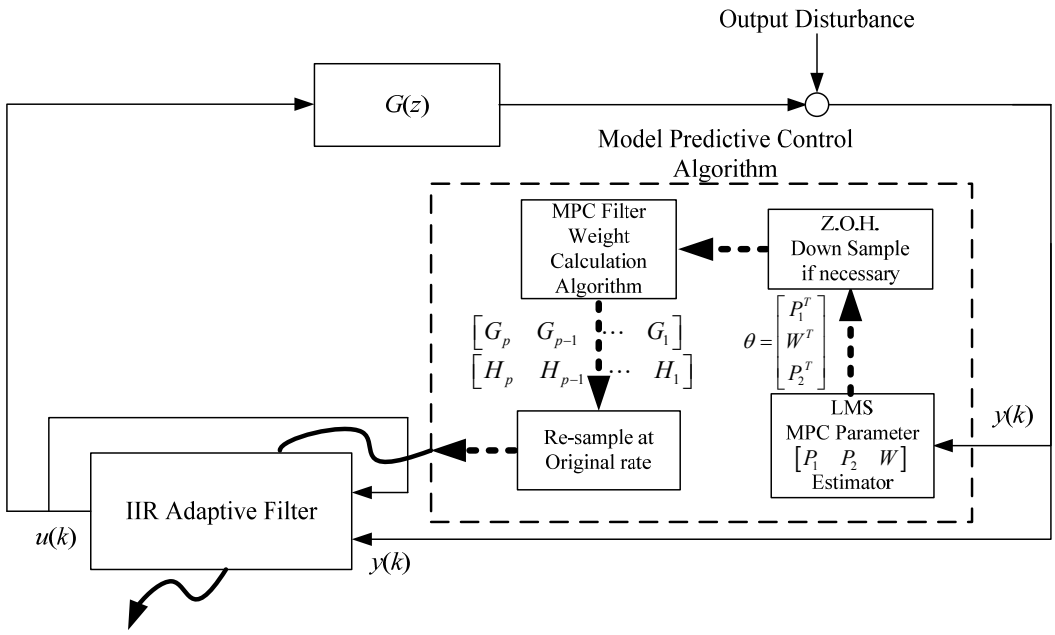

Figure 6-3. Real-time adaptive MPC scheme

6.2.4 Clear Box Algorithm associated with Adaptive Basis Method

The Clearbox algorithm of Refs. [47], [48], and [34] models the input/output dynamics as a *p*th order MIMO ARX (Auto-Regressive eXogenous inputs) model

$$y(k) = \sum_{i=1}^{p} \bar{\alpha}_i y(k-i) + \sum_{i=1}^{p} \bar{\beta}_i u(k-i) \tag{6.9}$$

that includes the influence of periodic disturbances following the internal model principle, i.e. instead of an explicit disturbance forcing function, the periodic disturbance is absorbed into the dynamics of the homogeneous equation by having poles on the stability boundary that produce result in oscillations at the disturbance frequencies. Hence, $y(k)$ is a disturbance corrupted output, and $\bar{\alpha}_i$ and $\bar{\beta}_i$ are the coefficients of the difference equation including the disturbance frequencies. This model can be identified using disturbance corrupted data using a model order

satisfying $p \geq (n + 2f + 1)/m$, where n is the order of the system, f is the number of frequencies in the disturbance, and the added one handles any constant disturbance if present. To obtain a disturbance free system model with coefficients α_i and β_i, one can convert to a state space model, diagonalize the model, and eliminate the state variables associated with eigenvalues on the unit circle and return to an ARX model. Form this model one can calculate the disturbance forcing function $\eta(k)$ from

$$\eta(k) = y(k) - \sum_{i=1}^{p} \alpha_i y(k-i) - \sum_{i=1}^{p} \beta_i u(k-i) \tag{6.10}$$

If the disturbance is to be eliminated from the output after transients have disappeared, producing zero output, the feedforward signal $u_f(k)$ needed to cancel the disturbance satisfies

$$\sum_{i=1}^{p} \beta_i u_f(k-i) = -\eta(k) \tag{6.11}$$

Given a periodic signal of a given frequency, one can produce this signal as a linear combination of the sine and the cosine function for that frequency. More generally one can produce it by any two functions of that frequency that have a different phase. If $\eta(k)$ is a sum of periodic disturbance functions, then the Adaptive Basis Method of Refs. [48], [34], generates a corrective control action as a superposition time shifted values of the $\eta(k)$ function

$$u_f(k) = \psi_1 \eta(k - \Delta_1) + \psi_2 \eta(k - \Delta_2) + \cdots + \psi_N \eta(k - \Delta_N) \tag{6.12}$$

where $N \geq 2f + 1$, and the Δ_i (i = 1,…,N) are the time (or phase) shifts need to span the space. Their choice should satisfy $\Delta_i \geq 1$ for causality, $\Delta_i \neq \Delta_j$ for all i and j to avoid duplication of time shifts, and $|\Delta_i - \Delta_j| \neq |\Delta_j - \Delta_k|$ for all i, j, and k to help prevent linear dependence of the basis

functions. The control coefficients ψ_i in Eq. (6.12) are recursively estimated using algorithms such as LMS and RLS. Also, the adaptive basis method may use past time steps of $\eta(k)$ more efficiently than that of a typical tapped-delay filter. Figure 6-4 presents a block diagram for this control algorithm.

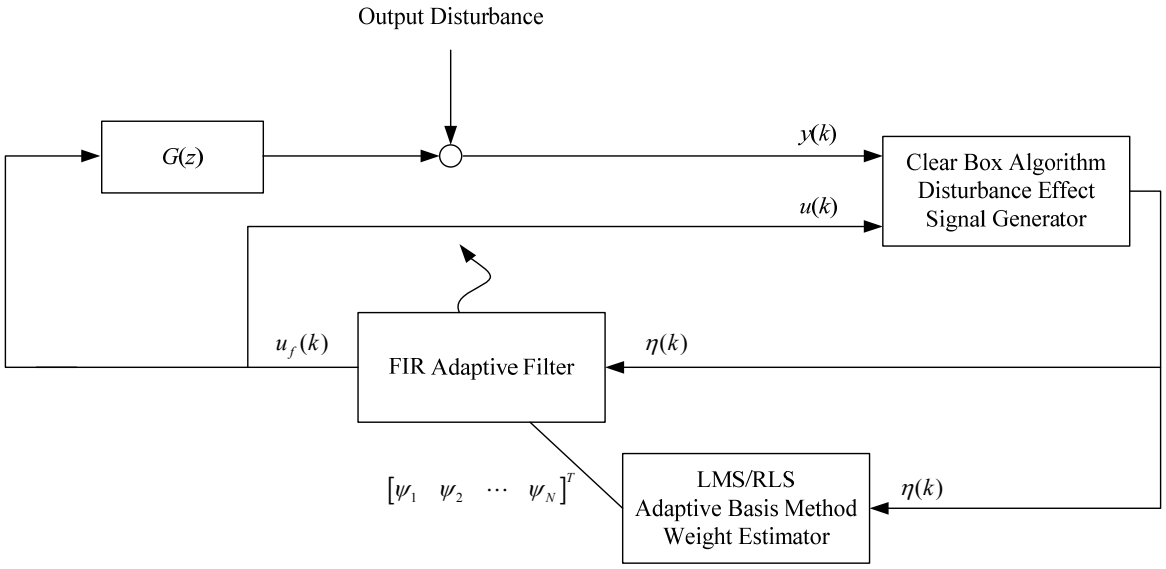

Figure 6-4. Adaptive Basis Method incorporated with the Clear box algorithm

The following will show how to derive a MIMO ARX model from a MIMO state space equation. Consider the state space equation

$$x(k+1) = Ax(k) + Bu(k)$$
$$y(k) = Cx(k) \tag{6.13}$$

where the system matrices A, B, and C are $n \times n$, $n \times r$, and $m \times n$ respectively for an r-input, m-output, n-state system. A z-transformation is applied and then rearranged with respect to the output $Y(z)$ as follows

$$Y(z) = C(zI - A)^{-1} BU(z) \tag{6.14}$$

The inversion term can be equivalently expressed in terms of an adjugate and determinant such as the following

$$Y(z) = C\frac{\text{adj}(zI - A)}{\det(zI - A)} BU(z) \tag{6.15}$$

The determinant term is multiplied on both side of the equation to yield

$$\det(zI - A)Y(z) = C\,\text{adj}(zI - A)BU(z) \tag{6.16}$$

where the determinant term is a n-dimensional polynomial of z and the adjugate term is a $n \times n$ matrix in which each element will be a (n-1)-dimensional polynomial at the most. The corresponding polynomials are denoted below

$$\det(zI - A) = z^n + \overline{a}_n z^{n-1} + \cdots + \overline{a}_1 z^0$$

$$C\,\text{adj}(zI - A)B = \begin{bmatrix} p_{11}(z) & p_{12}(z) & \cdots & p_{1r}(z) \\ p_{21}(z) & p_{22}(z) & \cdots & p_{2r}(z) \\ \vdots & \vdots & \ddots & \vdots \\ p_{m1}(z) & p_{m2}(z) & \cdots & p_{mr}(z) \end{bmatrix} \tag{6.17}$$

$$p_{ij}(z) = a_{ij,n-1} z^{n-1} + a_{ij,n-2} z^{n-2} + \cdots + a_{ij,0} z^0$$

The adjugate matrix term can further be decomposed into the following

$$\begin{bmatrix} p_{11}(z) & p_{12}(z) & \cdots & p_{1r}(z) \\ p_{21}(z) & p_{22}(z) & \cdots & p_{2r}(z) \\ \vdots & \vdots & \ddots & \vdots \\ p_{m1}(z) & p_{m2}(z) & \cdots & p_{mr}(z) \end{bmatrix} = \sum_{i=1}^{n} \begin{bmatrix} a_{11,i-1} & a_{12,i-1} & \cdots & a_{1r,i-1} \\ a_{21,i-1} & a_{22,i-1} & \cdots & a_{2r,i-1} \\ \vdots & \vdots & \ddots & \vdots \\ a_{m1,i-1} & a_{m2,i-1} & \cdots & a_{mr,i-1} \end{bmatrix} z^{i-1} \tag{6.18}$$

where the z-power term is now isolated from the matrices. Substituting the determinant and adjugate term in Eq. (6.15) with Eq. (6.17) and Eq. (6.18) respectively will yield

$$z^n Y(z) = -\sum_{i=1}^{n} \overline{a}_i z^{i-1} Y(z) + \sum_{i=1}^{n} \begin{bmatrix} a_{11,i-1} & a_{12,i-1} & \cdots & a_{1r,i-1} \\ a_{21,i-1} & a_{22,i-1} & \cdots & a_{2r,i-1} \\ \vdots & \vdots & \ddots & \vdots \\ a_{m1,i-1} & a_{m2,i-1} & \cdots & a_{mr,i-1} \end{bmatrix} z^{i-1} U(z) \tag{6.19}$$

which can conveniently be converted into an ARX model by applying an inverse z-transform such as the following

$$y(k) = \sum_{i=1}^{n} \overline{\alpha}_i y(k-i) + \sum_{i=1}^{n} \overline{\beta}_i u(k-i) \tag{6.20}$$

where

$$\overline{\alpha}_i = -\overline{a}_{n-i+1}$$

$$\overline{\beta}_i = \begin{bmatrix} a_{11,n-i} & a_{12,n-i} & \cdots & a_{1r,n-i} \\ a_{21,n-i} & a_{22,n-i} & \cdots & a_{2r,n-i} \\ \vdots & \vdots & \ddots & \vdots \\ a_{m1,n-i} & a_{m2,n-i} & \cdots & a_{mr,n-i} \end{bmatrix} \tag{6.21}$$

We now have a MIMO ARX model.

6.3 EXPERIMENTAL SETUP

The TAS2 spacecraft simulator allows us to test the above jitter control algorithms in hardware with realistic disturbances produced by 3 CMGs operating for the attitude control system. An artificially generated disturbance source was used in hardware experiments of some nonconventional control algorithms in Ref. [49], [50]. The TAS2 is floated on an air bearing with the attitude control system operating for some of the experiments, while other experiments do

not float the simulator. Figure 6-5 shows the TAS2 experimental setup, while Figure 8 shows the actual hardware. The receiving telescope receives laser light from a laser source, which is reflected off of the control fast steering mirror (FSM) and then off of the beam splitter, and sent out through the transmitting telescope directed to the desired destination on the target position sensing device (PSD). Ideally, one wishes to keep the laser centered on this device in spite of jitter of the testbed. Of course in applications one does not have access to such feedback information at the receiving location, and one would like to have a sensor on the output of the transmitting telescope that measures inertial motion of the output laser relative to inertial space. For purposes of these experiments we seek to eliminate all jitter as sensed at the location of the beam splitter, aiming to keep the signal centered on the jitter detection PSD. The characteristics of this control problem should be very similar to that of the actual problem, so that the experiments do represent an appropriate test of the effectiveness of the methods.

Figure 6-6 shows the hardware. The optical payload consists of an upper optical deck with a receiver telescope, a lower optical deck with a transmitter telescope, and they are connected though a rotational stage with a hollow shaft to provide the gimbaled motion and the optical path of the beam. The transmitter telescope on the lower deck is connected to the spacecraft bus through passive vibration isolators. The beam splitter transmits 50% of the light to the jitter detection sensor, an ON-TRAC Photonics Inc. PSD. This signal is used by the candidate control algorithms to adjust the pan and tilt of the FSM on the lower deck.

The attitude control system uses CMGs, which are preferred over reaction wheels due to their higher torque levels for agile spacecraft control. Four CMGs are mounted on the spacecraft bus, with rated angular momentum of 22.5 N-m-s at 2500 RPM and a maximum torque of 12 N-m. Attitude sensing is done with the camera shown located on the upper deck, which senses 3 stars

displayed on the LCD screen on the ceiling. It is connected to a dedicated computer through a frame grabber, and this computer communicates to the spacecraft bus computer to transfer attitude information. The simulator electronics is an integration of power control switch box, power switching and control electronics, and an industrial PC. The power control switch box has a main power switch and individual switches for CMGs, IMU, top deck control, and the mass balancing system. It also has an interface with an external power supply. Power switching and control electronics interface CMG controllers, IMU, IR sensor, and inclinometers. A PC104 industrial PC has an analog input and output ports as well as digital out ports to send the commands and receive various data from control electronics and sensors. The main control program is coded in the host computer using Matlab/Simulink. Real-time control software is communicating between the host computer and target PC104 industrial PC via wireless Ethernet connection.

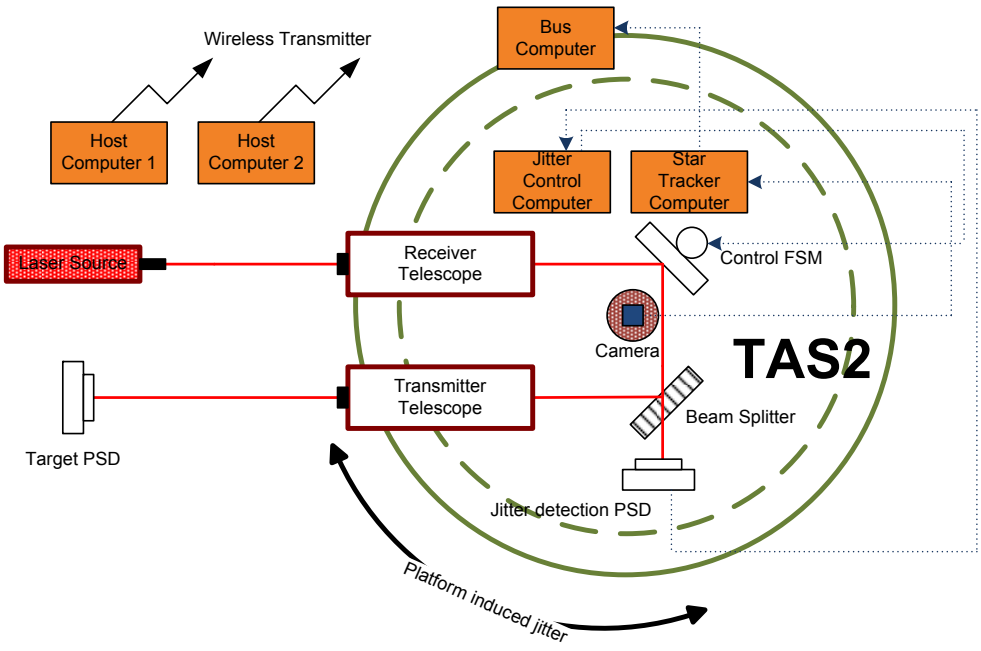

Figure 6-5. TAS2 Experiment Setup

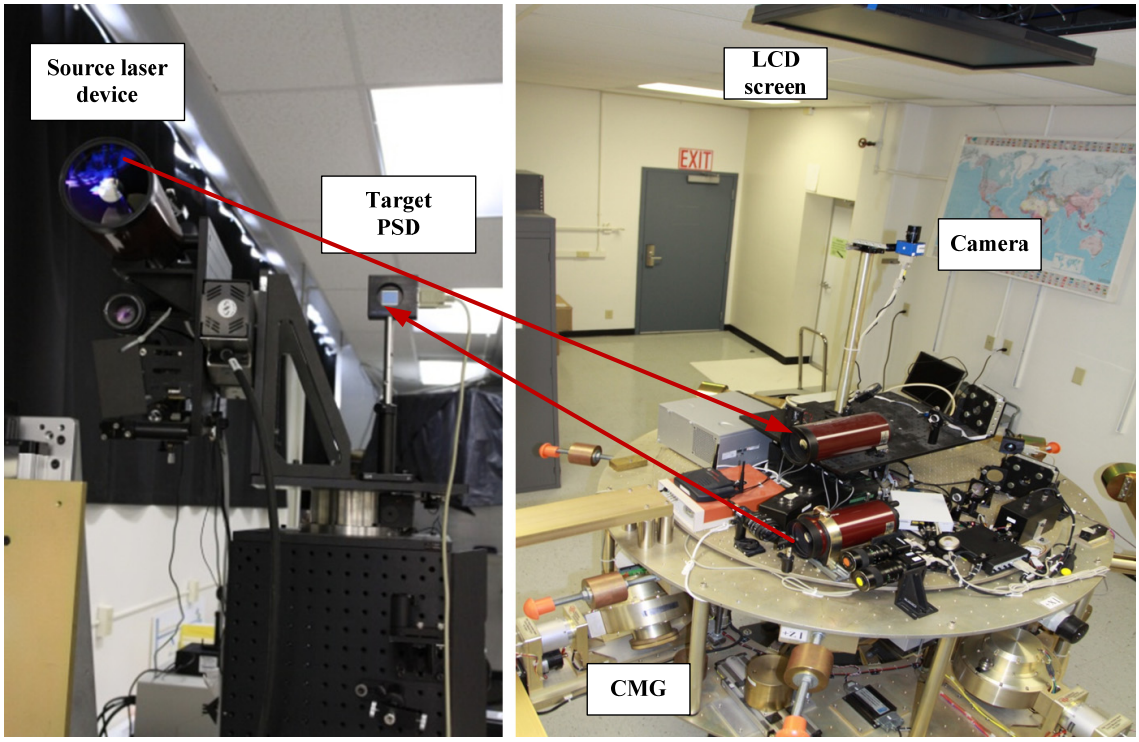

Figure 6-6. Image of EARL and TAS2 relaying a laser beam

6.3.1 Control Implementation

Two host computers and three target computers run simultaneously, but not synchronously, for attitude pointing and beam stabilization. All target PC's run in a real-time operating system environment called xPC Target by Mathworks. The target computers are dedicated to separate tasks of jitter control, star tracker, and the spacecraft bus. The code is programmed in Matlab/Simulink, compiled into C, and then downloaded onto its respective target computer through a wireless router on the testbed.

The SVS-Vistek 340 camera transmits a 640 x 480 12 bit digital sequence to the frame grabber which interprets the digital sequence as an image that is processed by the target computer at a sample rate of 80 Hz. The sample rate is selected to be 2 times faster than the bus computer due to the asynchronous operation between the two computers. The calculated

quaternion components are transmitted through the NI PCI-6733 output board toward the Diamond-MM-32-AT data acquisition board where the signal is acquired located at the bus sector.

The bus sector computer runs a quaternion feedback control scheme based on the acquired quaternion components from the star tracker at a sample rate of 40 Hz. The IMU provides rate information used for the derivative action of the attitude control law and for the steering logic to drive the gimbals through a RS-232 serial port connection. The desired rotation rate is also transmitted through the serial connection. Hall effect sensor data from the CMG's are transmitted to the jitter control computer through the data acquisition board in order to provide information of the rotating speed of the CMG's.

The PSD outputs two analog signals that range from -10 to 10 V where 0 V refers to the case when the beam hits the center of the sensor for both x and y axes. The analog signal is acquired by the NI PCI-6259 data acquisition board (DAQ) and then processed by the jitter control target computer at a sample rate of 5 kHz. A compensating command signal is calculated from the chosen control algorithm. This signal is transmitted through the DAC of the DAQ toward the FSM where the jitter within the beam is corrected. Figure 6-7 below shows a schematic of the interconnection between the several experimental components.

Table 6-1. Software/Hardware specifications for TAS2

Software/Hardware	Specifications
Matlab	2011b, xPC Target 5.1, 2007b, xPC Target 3.3,OKID Toolbox
Star tracker Computer	AMD Athlon 64 X2 5200+ 2.7 GHz
Jitter Control Computer	Intel® Core™ i7-2600K Processor 3.4 GHz

Bus Computer	Intel Pentium III 750MHz

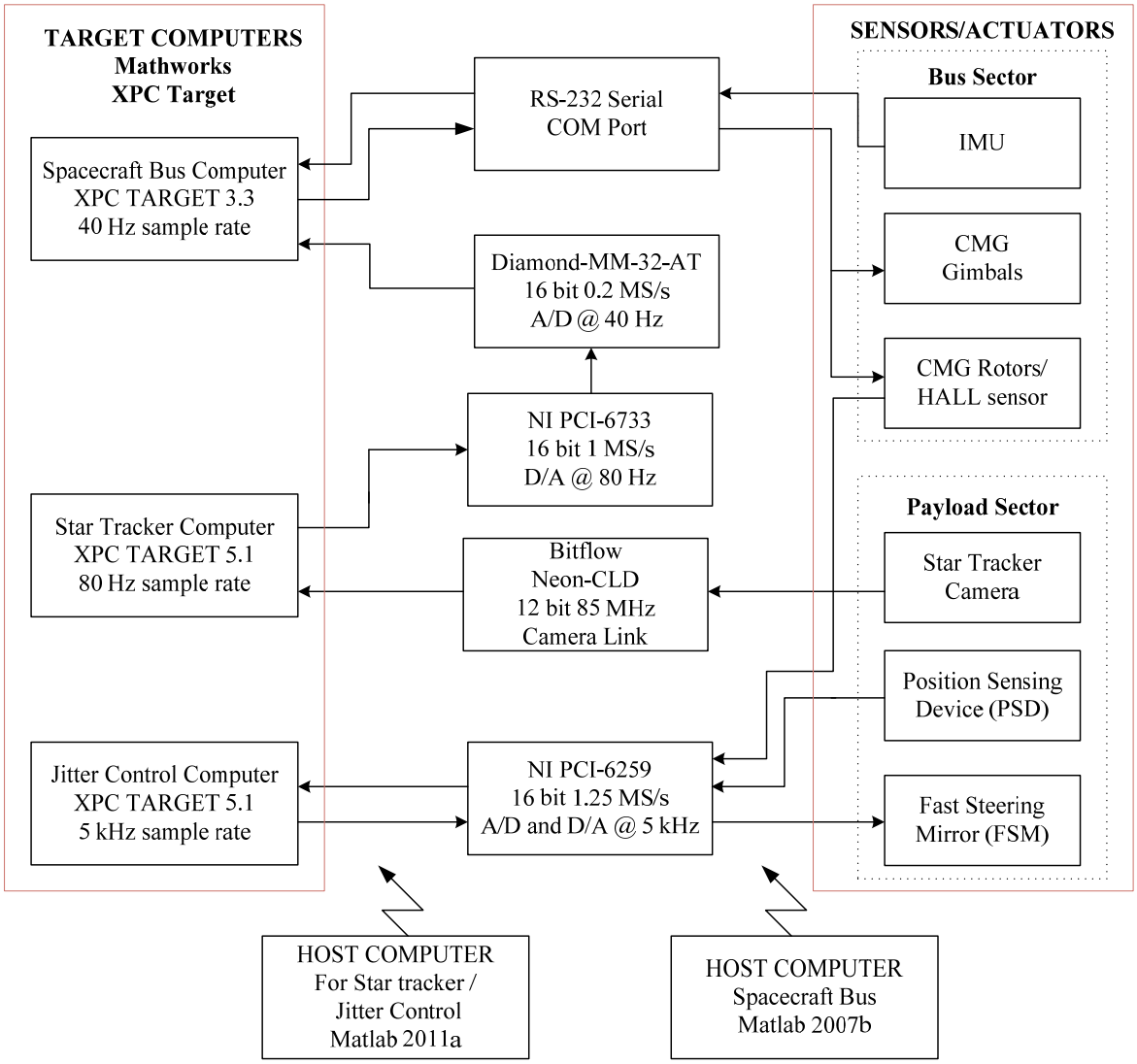

Figure 6-7. Control Implementation

6.4 ATTITUDE SENSING WITH THE STAR TRACKER

The attitude sensor is a star tracker. The camera processes the acquired image of the stars so that the vector starting from the origin of the camera coordinate frame to each star on the LCD screen is calculated. A reference vector of the stars that are acquired within the reference

coordinate frame is calculated a priori. Afterwards the star tracker calculates the star vectors associated with the most current orientation each time step. During the duration of the most recent time step, the QUEST algorithm (Ref. [51], [52]) estimates the current orientation by using both the reference and current-time star vectors. Because the star images are near to the camera and not at infinity, additional computation must be made as detailed below. One must modify the star vectors originating from the camera coordinate frame by recalculating the star vectors to start from the origin of the spacecraft coordinate frame instead.

6.4.1 Using the Camera for Star Vector Calculation

A method proposed by Carl Christian Liebe (Ref. [53]) shows how a camera can be used to compute the unit vectors pointing toward each star from the origin of the camera coordinate frame. The actual position of each star that is imaged on the charged-coupled-device (CCD) of the camera can be directly measured in terms of physical units, and this takes care of the x and y coordinates of the current star of interest on the CCD. The magnitude of the z coordinate, which is the distance between the origin of the camera frame and CCD sensor, is considered to be equivalent to the focal length of the lens, provided that the distance of the object is at least 10 times larger than the focal length. Therefore one is able to calculate the unit vector of each star on the CCD from the origin of the camera coordinate frame. The unit vectors of stars on the LCD screen is computed by flipping the sign of the previous vectors according to

$$\begin{pmatrix} S_x \\ S_y \\ S_z \end{pmatrix} = \left[\text{norm} \begin{pmatrix} -(X_c - X_o) \\ -(Y_c - Y_o) \\ -f \end{pmatrix} \right]^{-1} \begin{pmatrix} -(X_c - X_o) \\ -(Y_c - Y_o) \\ -f \end{pmatrix} \tag{6.22}$$

where S_x, S_y, and S_z correspond to the *x*, *y*, and *z* components respectively, of the unit star vector with respect to the camera coordinate frame, (X_c, Y_c) are the coordinates of the stars located on the CCD sensor or focal plane, (X_o, Y_o) is the intersection of the optical axis and the focal plane, and *f* is the focal length of the lens. See Figure 6-8. When acquiring the image from the camera it is important that the image is rearranged so that it appears as it would if it were to be seen on the CCD sensor. Also, the coordinate frame of the acquired image must be equivalent to the selected camera coordinate frame. Only then will the star tracker provide the correct star vectors.

6.4.2 QUEST Algorithm

Let the $\boldsymbol{b}_i$ denote the star unit vectors associated with the most current time-step orientation of the spacecraft where *i* depends on the number of stars that are acquired from the image. The reference unit vectors, denoted as $\boldsymbol{r}_i$, are calculated offline and serve as a set of reference vectors for the stars when the spacecraft is aligned with the *R* reference coordinate frame. We wish to find the orthonormal 3 x 3 direction cosine matrix *A* by solving $\boldsymbol{b}_i = A\boldsymbol{r}_i$. The Wahba problem asks to find matrix *A* to minimize

$$L(A) = \frac{1}{2}\sum_{i=1}^{k} \left|\boldsymbol{b}_i - A\boldsymbol{r}_i\right|^2 \tag{6.23}$$

Alternatively, one may want to find the quaternion representation $\boldsymbol{q}$ to minimize

$$J(\boldsymbol{q}) = \frac{1}{2}\sum_{i=1}^{k} a_i \left|\boldsymbol{b}_i - A(\boldsymbol{q})\boldsymbol{r}_i\right|^2 \tag{6.24}$$

where the a_i are positive weights assigned to each measurement. Instead of minimizing *J*, we can maximize *g* defined as

$$g(\boldsymbol{q}) = 1 - J(\boldsymbol{q}) / \left(\tfrac{1}{2} \sum_{i=1}^{k} a_i \right) \tag{6.25}$$

It can be shown that $g(\boldsymbol{q})$ can be written as $g(\boldsymbol{q}) = \boldsymbol{q}^T K \boldsymbol{q}$ where

$$K = \begin{bmatrix} S - \sigma I & z \\ z^T & \sigma \end{bmatrix} \; ; \; \boldsymbol{z} = \frac{1}{m_k} \sum_{i=1}^{k} a_i \left(\boldsymbol{b}_i \times \boldsymbol{r}_i \right) \; ; \; S = B + B^T \; ; \; B = \frac{1}{m_k} \sum_{i=1}^{k} a_i \boldsymbol{b}_i \boldsymbol{r}_i^T \; ; \; \sigma = \frac{1}{m_k} \sum_{i=1}^{k} a_i \boldsymbol{b}_i^T \boldsymbol{r}_i$$

$$m_k = \sum_{i=1}^{k} a_i \tag{6.26}$$

and *I* is the 3 by 3 identity matrix. It can be shown that the $\boldsymbol{q}^*$ of unity length that maximizes $g(\boldsymbol{q})$ satisfies the eigenvector equation $K\boldsymbol{q}^* = \lambda \boldsymbol{q}^*$ where λ is a Lagrange multiplier. Substitution into $\boldsymbol{q}^T K \boldsymbol{q}$ shows that it is maximized by the largest eigenvalue $g(\boldsymbol{q}^*) = \lambda_{\max}$, and $\boldsymbol{q}^*$ is the corresponding eigenvector. Once $\lambda_{\max}$ is found, there is no need to solve for the eigenvector of *K*, because the optimal vector of Rodrigues parameters $\boldsymbol{y}^*$ and the optimal quaternion can be found from

$$\boldsymbol{y}^* = [(\lambda_{\max} + \sigma) I - S]^{-1} \boldsymbol{z} \qquad ; \qquad \boldsymbol{q}^* = \frac{1}{\sqrt{1 + \left| \boldsymbol{y}^* \right|^2}} \begin{bmatrix} \boldsymbol{y}^* \\ 1 \end{bmatrix} \tag{6.27}$$

6.4.3 Indoor Star Tracker Algorithm

The star vectors originating from any point on the spacecraft will be the same when the stars are at infinity. Corrections must be made when the star tracker is indoors (Ref. [54]). When the

stars are close to the camera and when there is a discrepancy between the origin of the camera body coordinate frame, denoted as O^C in Figure 6-9, and the origin of the spacecraft body coordinate frame, denoted as O^S. From Figure 6-9 one observes the difference between star vectors $\boldsymbol{b}_i$ and star vectors $\hat{\boldsymbol{b}}_i$. Therefore the vector measured from the camera body coordinate frame cannot be used as a correct measurement for the spacecraft attitude with a coordinate frame originating at O^S. The vectors from O^S to each star on the screen is calculated directly using basic vector calculations

$$\bar{R}_o + \alpha_i \hat{\boldsymbol{b}}_i = \beta_i \boldsymbol{b}_i \tag{6.28}$$

where α_i and β_i are the distances from the stars to the origins O^C and O^S respectively, and $\bar{R}_o$ is the vector from O^S to O^C.

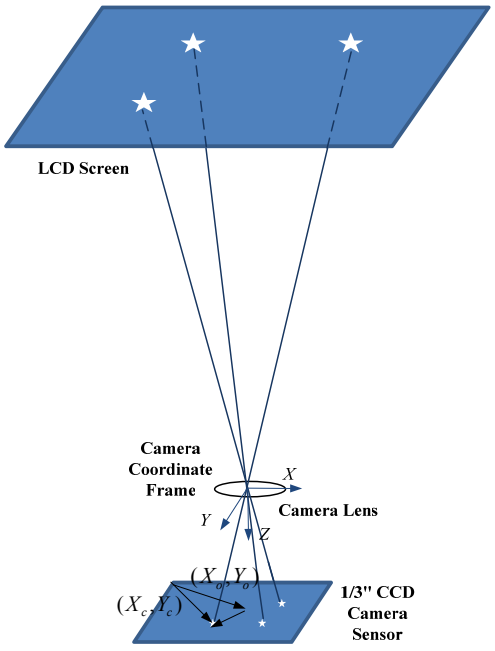

Figure 6-8. Star Vectors detected by star tracker

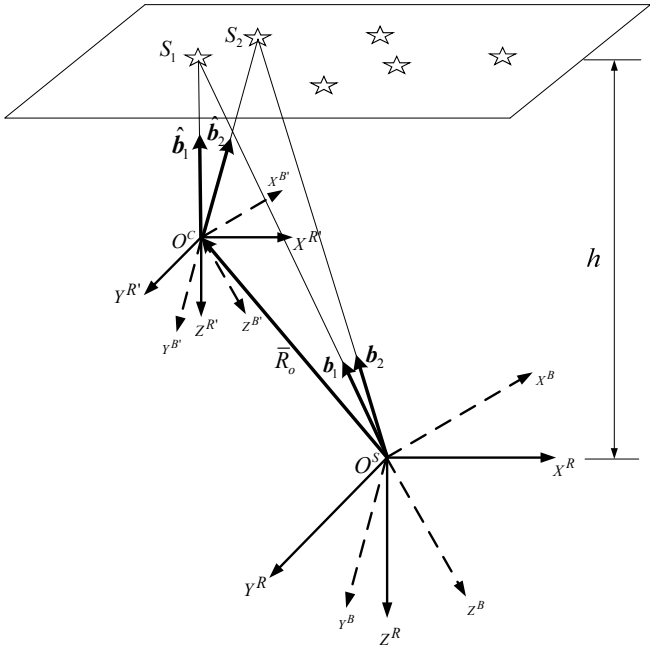

Figure 6-9. The indoor star tracker problem

The inertial reference frame of the spacecraft is defined as the *R* coordinate. The direction cosine matrix A is equal to the three-by-three identity matrix when the spacecraft body coordinates are aligned with this coordinate frame. In our special case, this is the orientation that permits the laser beam to traverse through the entire optical path. In order to solve Eq. (6.28) we must project the two vector terms on the left side onto the *z*-axis provided that the distance between O^S and the LCD screen, denoted as *h*, can be measured accurately. Define a vector $p = [0 \quad 0 \quad -1]^T$ that is coaxial with the negative *z*-axis in the inertial coordinate frame *R*. Then α_i is calculated by the vector relationship

$$\alpha_i = \left[h - p \bullet \left(A^T \overline{R}_o^{\,B} \right) \right] / \; p \bullet \left(A^T \hat{\boldsymbol{b}}_i^{\,B'} \right) \tag{6.29}$$

where the superscript *B* in both $\overline{R}_o^{\,B}$ and $\hat{\boldsymbol{b}}_i^{\,B'}$ indicate that the vectors are represented with respect to the moving body coordinate frame. Equation (6.29) shows that α_i is dependent of *A* making $\boldsymbol{b}_i$ of Eq. (6.28) dependent of *A* as well. Thus $\boldsymbol{b}_i = A\boldsymbol{r}$ becomes $\boldsymbol{b}_i(A) = A\boldsymbol{r}_i$ which is a nonlinear problem. The indoor star tracker algorithm developed in Ref. [54] addresses the nonlinear problem using a sequence of iterations solving linear equations as presented in the following Algorithm. Simulation results from previous work show that the orientation *A* will converge to its true value with only a few iterations provided that the initial error in *A* is smaller than 3 degrees.

Algorithm 6-1. Indoor Star Tracker Algorithm with QUEST

acquire $\hat{\boldsymbol{b}}_i; A = I$

for $j = 1:10$

$$\alpha_i = \frac{h - p \bullet \left(A^T \bar{R}_o^{\,B} \right)}{p \bullet \left(A^T \hat{\boldsymbol{b}}_i^{\,B'} \right)} \; ; \boldsymbol{b}_i = \text{normalize}\left(\bar{R}_o + \alpha_i \hat{\boldsymbol{b}}_i \right); A = \text{QUEST}\left(\boldsymbol{r}_i, \boldsymbol{b}_i \right)$$

end

6.5 EXPERIMENTAL RESULTS

6.5.1 System Identification

Both the MPRC and the XLMS algorithms want a mathematical model for the relationship of actuator inputs to the (Baker Adaptive Optics Light Force one) FSM to the resulting output measured by the ON-TRAK PSD (Figure 6-10). Such a model is helpful for MBFRC if it is to adaptively update the information about the disturbance frequency ϕ_n and the associated gain and phase responses r_n and τ_n. The Clearbox algorithm allows one to create and use a disturbance corrupted model for the situation where it is not possible to turn off the disturbance. For the testbed we are able to create a model with the CMGs off in order to obtain a disturbance free model directly.

Figure 6-11 separately investigates the behavior of the FSM. They commonly have a limited linear operating range. Uniformly distributed white Gaussian noise at the different amplitudes indicated result in the output frequency responses shown in the figure, and we see that the responses do not completely scale with the input amplitudes at higher frequencies suggesting nonlinear behavior for higher amplitude inputs at higher frequencies.

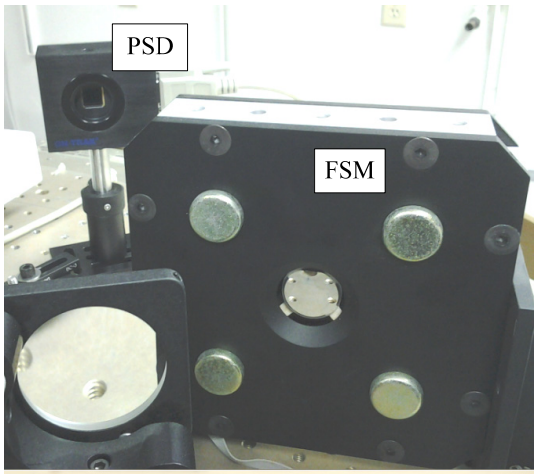

Figure 6-10. Baker FSM and ON-TRAK PSD

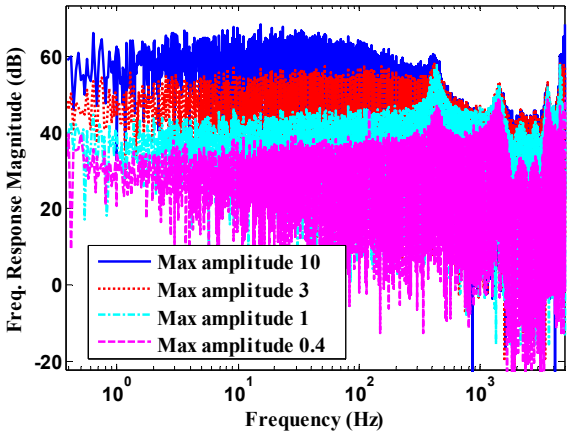

Figure 6-11. Possible nonlinear FSM behavior

To obtain the model from actuator to output, a sine sweep input from 0.1 Hz to Nyquist frequency was applied to the FSM at a sample rate of 5 kHz, collecting four sets of input-output data for the *x* and *y* axis, including any dynamic coupling between the two axes. The results are shown in Figures 6-12 and 6-13. The cross coupling terms in Figure 6-12 have a substantially reduced output and hence we neglect the coupling. Then 14^{th} order ARX models were generated for the uncoupled *x* and *y* axes using the Observer Kalman-Filter Identification (OKID) package (Ref. [55]) designed for identification from frequency response data.

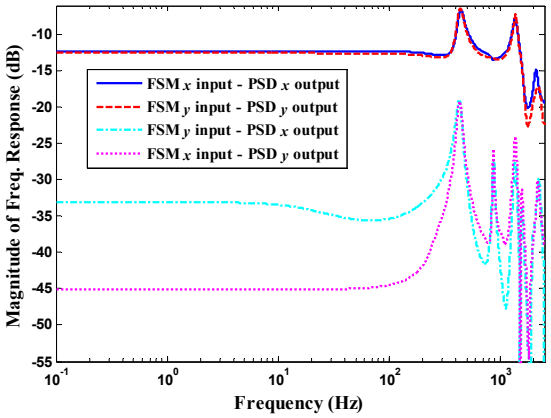

Figure 6-12. Magnitude of Freq. Response

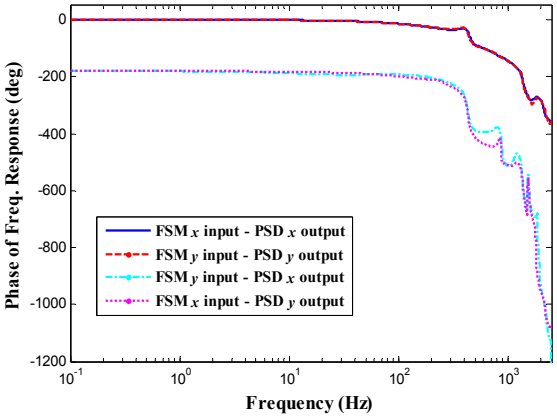

Figure 6-13. Phase of Freq. Response

6.5.2 Spacecraft Attitude Regulation and Disturbance Characteristics

The TAS2 spacecraft bus has an upside-down pyramid mounting of four single gimbal control moment gyros, only three of which are used in the experiments. The skew angle is setup as 90 degrees, and the pseudoinverse steering logic from Bong Wei (Ref. [56]) is applied. The attitude regulation of the spacecraft bus uses a quaternion PID feedback control law employing quaternion feedback from the star tracker unit, and rate information for steering and PID control comes from the onboard IMU. The spacecraft regulates with respect to the desired quaternion [0 0 0 1], which allows the laser beam to go through the receiving telescope and be relayed toward the designated target. The rotor speed of the CMGs is around 35.5 Hz, or 2130 rpm, and the sample rate of the spacecraft attitude control system runs at 40 Hz.

From Figures 6-14 and the detail in Figure 6-15 showing the fourth quaternion component, the spacecraft maintains 0.01 degree accuracy during the period starting from 45 seconds to the end of the experiment. This accuracy allows the beam to always traverse the full optical train. After the quaternion feedback control law manages to maintain the beam within range of the PSD, the

PSD begins to collect data displaying the characteristics of the CMG induced jitter, as shown in Figures 6-16 and 6-17.

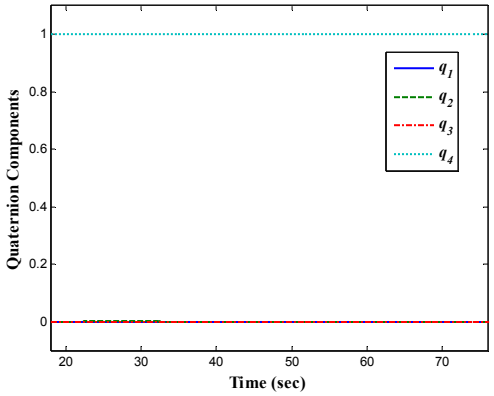

Figure 6-14. Quaternion components during spacecraft regulation

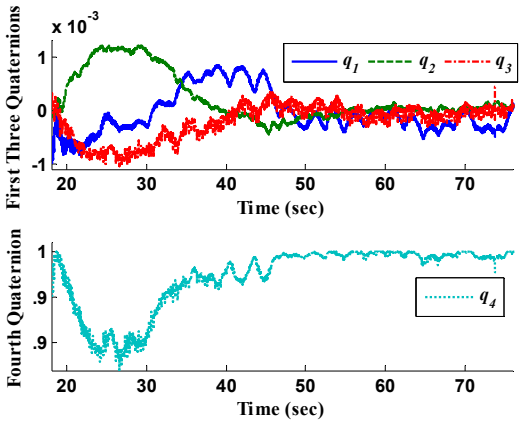

Figure 6-15. Enhanced view of quaternion components for spacecraft regulation

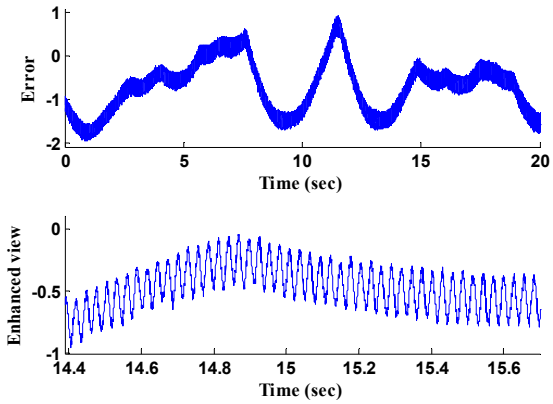

Figure 6-16. Disturbance characteristics during spacecraft regulation

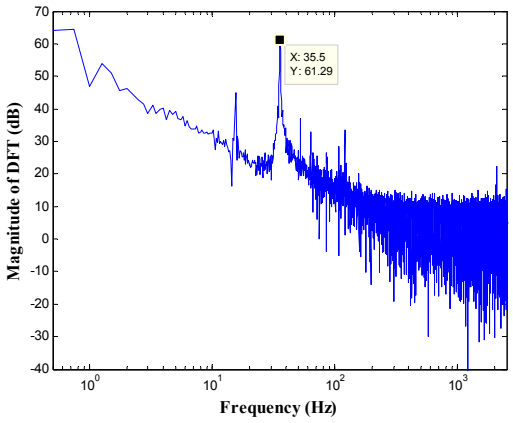

Figure 6-17. DFT magnitude of disturbance environment

Figure 6-16 demonstrates low frequency variations of the beam position on the PSD despite the active attitude control system. The Discrete Fourier Transform (DFT) of the error data in Figure 6-17 exhibits a tall peak at 35.5 Hz corresponding approximately to the Hall effect sensor information, which fluctuates between 140 and 141 time steps per revolution. The CMG speed is

calculated from this number of time steps between pulses, and this limits the accuracy of the information. Nevertheless, the dominant frequency component of the jitter corresponds closely to once per revolution of the CMGs. The ON-TRAK PSD uses a 10.0 x 10.0 mm duolateral silicon sensor for centroiding the beam. The peak to peak amplitude of the jitter corresponds to 0.43 V, which represents 400 micro meters on the sensor. Using the length of the optical path from the receiving telescope to the PSD we can approximately compute the mean amplitude of the optical beam angular jitter onboard of the spacecraft to be 184 micro radians. A similar attempt can be made to compute the angular jitter of the transmitting beam coming from the spacecraft.

6.5.3 Disturbance Rejection Experiments without Floating the Spacecraft on the Air Bearing

In the preliminary set of experiment to understanding the characteristics of each control algorithm for jitter suppression, the TAS2 is not floated but simply sits on top of the air bearing. The CMG's are turned on to produce the CMG induced optical jitter but the attitude control system is off. The control algorithms are turned on at 4 seconds.

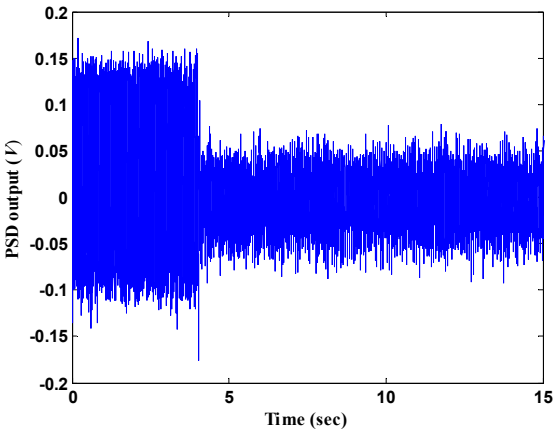

Figure 6-18. MPRC controlling jitter with CMG speeds at 21.1, 28, 34.75 Hz

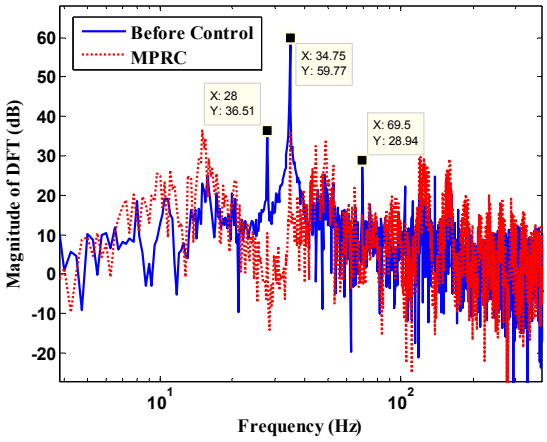

Figure 6-19. DFT magnitude of jitter from Figure 6-18

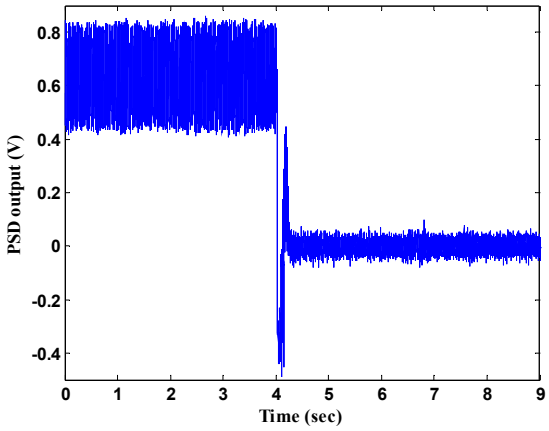

Figure 6-20. MPRC controlling jitter with all three CMG speeds at 35.67 Hz

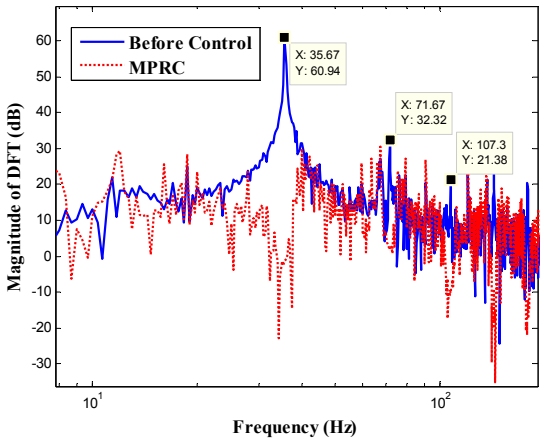

Figure 6-21. DFT magnitude of jitter from Figure 6-20

Figures 6-18 through 6-21 display the disturbance rejection capabilities of MPRC. A 51-gain filter H cuts off the learning at 300 Hz, and the RC gain is reduced to 0.8 to reduce noise sensitivity. The compensator uses 40 gains with V set to zero in Eq. (2). Experiments are performed using three different periods, one for each CMG (Figures 6-18 and 6-19), and using the same commanded period for all CMGs (Figures 6-20 and 6-21). When addressing multiple unrelated periods, MPRC attenuates the dominant frequency components, but it fails to completely nullify the disturbance peak at 34.75 Hz due to limitations in accurately synchronizing with the CMG rotation speed. This peak corresponds to 143.88 samples per period. The rotor speed calculated by counting the number of time steps between impulses from the Hall effect sensor is not able to provide an accurate period when it is not an integer number of time steps. One could increase the sample rate separately for just the CMG algorithm, and then use an interpolator for the repetitive controller. Note from Figure 6-21 that MPRC completely nullifies the dominant frequency component and all its harmonics up to the cutoff when all three speeds are made to coincide, i.e. MPRC becomes robust to period uncertainties

when addressing multiple identical periods. This represents a new method of addressing the issue of sensitivity of RC to uncertainty or fluctuations in the period, and is a competitor to the higher order RC methods of Refs. [24] and [25]. The waterbed effect is also observed in the figure, where significant attenuation at some frequencies must be compensated by amplification at some other frequencies. More detail within this phenomenon was explained within chapter 4 and Reference [57].

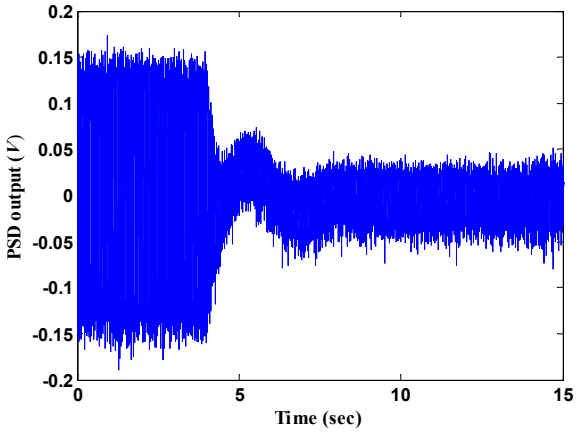

Figure 6-22. MBFRC controlling jitter with all three CMG speeds at 35.75 Hz

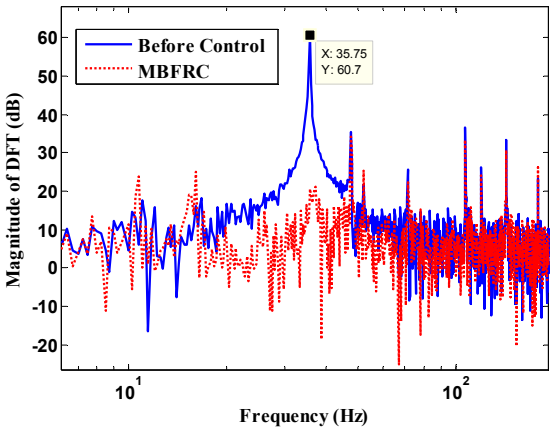

Figure 6-23. DFT magnitude of jitter from Figure 6-22

Figures 6-22 and 6-23 show results using MBFRC with control gain 0.0002 and a_n set to 1. The three CMGs of the TAS2 will be rotating at the same speed. MBFRC also decreases sensitivity to accurate knowledge of the period when it addresses multiple identical periods. The theory guarantees stability for sufficiently small gain (Ref. [30]), but the size of the gain was limited, and produced the slow convergence in Figure 6-22. The small gain limited the amplification from the waterbed effect. Note that for MBFRC if one wants to attenuate a

harmonic, one has to individually address this frequency as well as the fundamental. This was not done in these experiments.

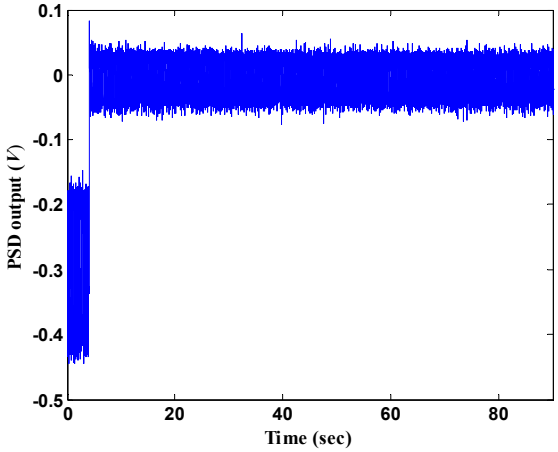

Figure 6-24. XLMS controlling jitter with CMG speeds at 21.3, 28, 35 Hz

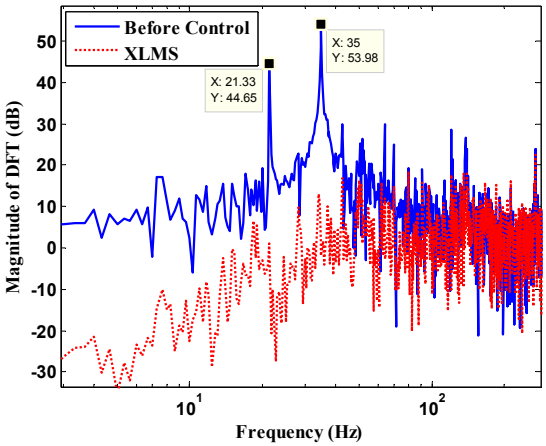

Figure 6-25. DFT magnitude of jitter from Figure 6-24

Figures 6-24 and 6-25 study XLMS showing good disturbance rejection for not just the dominant frequency components but also a substantial portion of the broadband low frequency disturbance as well. It does not address the harmonics. Note that the DFT was taken from 70 to 90 seconds, where the XLMS algorithm has fully converged. Although it has not displayed, the dominant frequency components are not completely nullified during the earlier part of the experimental run. Therefore much time is required to get such good results using XLMS. The gain required for maintaining stability is 0.03, and a large number of weights, 1500, were used for the tapped-delayed FIR filter. This was necessary to achieve this performance.

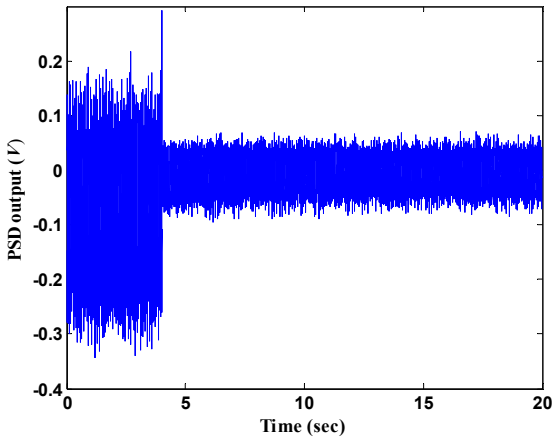

Figure 6-26. MPC controlling jitter with CMG speeds at 21.3, 28, 35 Hz

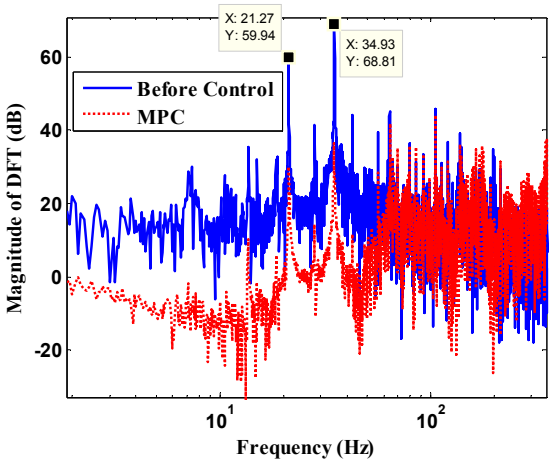

Figure 6-27. DFT magnitude of jitter from Figure 6-26

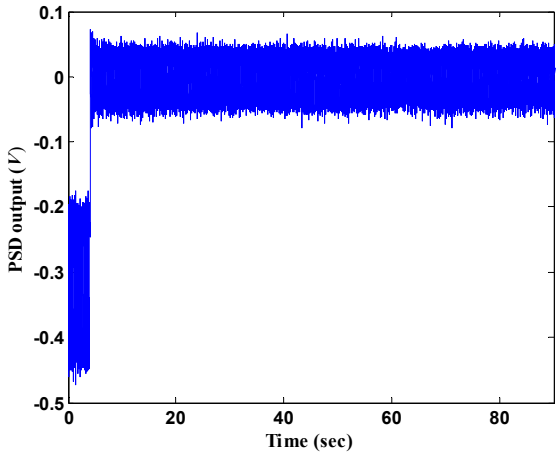

Figure 6-28. Adaptive Basis Method controlling jitter with CMG speeds at 21.3, 28, 35 Hz

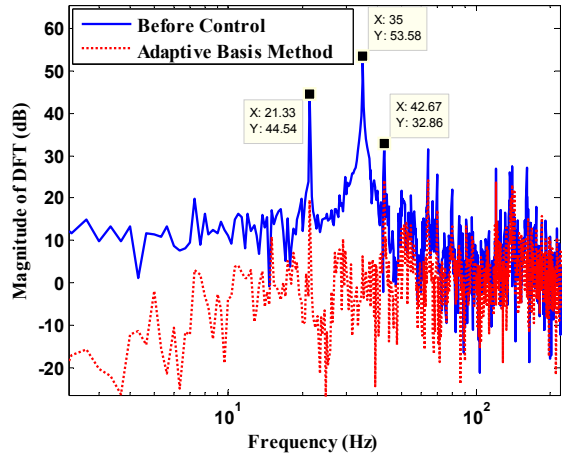

Figure 6-29. DFT magnitude of jitter from Figure 6-28

Figures 6-26 and 6-27 show results for the MPC approach. White Gaussian noise is applied for 4 seconds at the beginning of the run for initial identification with an LMS algorithm, and thereafter the IIR filter weights are updated every time step. Figure 6-27 shows decent disturbance rejection at the dominant peaks and good broadband disturbance rejection in the low frequency range. This design used 80 past time steps, and 10 future steps, starting two steps

within the future. The adaptive step gain for the LMS algorithm is 0.000000001 in order to maintain stability. The MPC law here decides to act as a broadband controller.

Adaptive Basis Method results are given in Figures 6-28 and 6-29. Note the similarity to XLMS. However, ABM used only 30 weights for the adaptive FIR filter compared to 1500. This is possible due to fact that ABM eliminates redundancies when utilizing the delayed information of the reference signal. The step gain is 0.03 for the LMS algorithm. However, a 300^{th} order ARX model of Eq. (6.10) was used for accurately identifying the undamped natural frequencies due to the presence of large noise. Simulation results not shown here suggest that a lower order model could be successfully used.

6.5.4 Disturbance Rejection with Spacecraft Floated

The following results float the TAS2 on its air bearing to simulate a non-gravity environment. The three CMGs of the TAS2 will be rotating all at the same speed. The star tracker will maintain the attitude within the tolerance needed for the beam to traverse the full optical path. The jitter control algorithms are initiated once the spacecraft attitude controller has settled. The control action for each algorithm will begin after 4 seconds. It is interesting to note that there is a new frequency peak introduced when we float the testbed, and algorithms that do not address this frequency can amplify it.

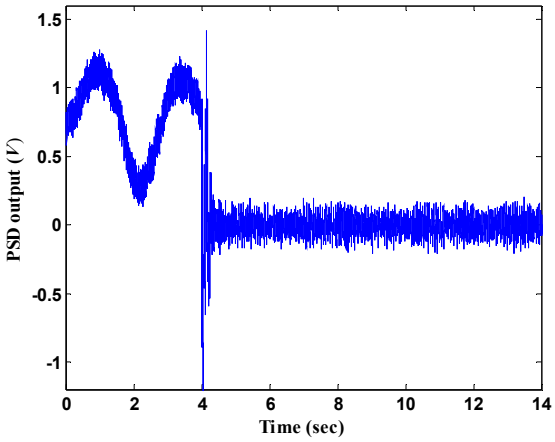

Figure 6-30. MPRC controlling jitter with spacecraft floating with attitude controller

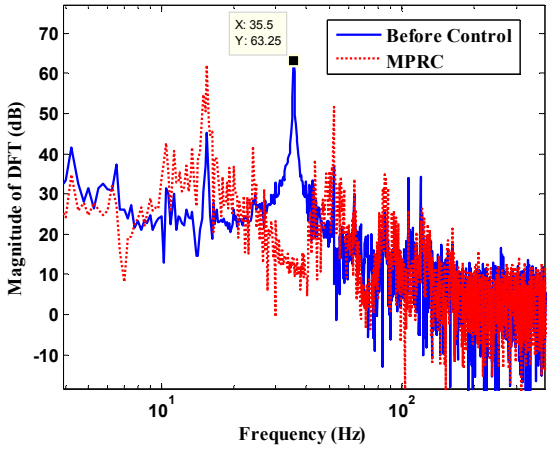

Figure 6-31. DFT magnitude of jitter from Figure 6-30

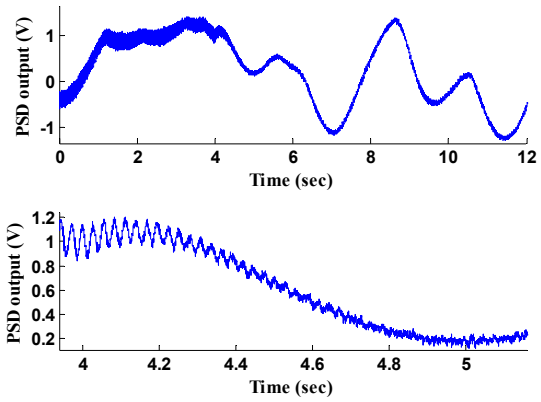

Figure 6-32. MBFRC controlling jitter with enhanced view at 4 ~ 5 seconds

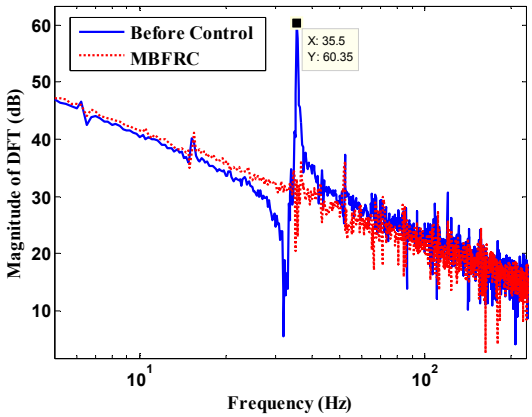

Figure 6-33. DFT magnitude from Figure 6-32

Figures 6-30 and 6-31 give results for MPRC with good disturbance rejection at the dominant peak using the same design parameters as previously. The waterbed effect produces amplification of neighboring frequencies, including amplification of the new peak. Concerning MBFRC, Figures 6-32 shows it is not able to stabilize the beam toward the center of the PSD,

although the enhanced view in the lower half of the Figure demonstrates that the high frequency jitter is slowly attenuating after 4 seconds. Figure 6-33 verifies that the dominant peak has been accurately nullified despite being unable to center at the PSD. The MBFRC results without floating had slow convergence due to the small gain value needed for stability. This gain limitation with its slow convergence may prevent the method from addressing the large amplitude variations encountered here. MBFRC fails to address the large-amplitude-low-frequency-components, but succeeds in addressing the small amplitude jitter.

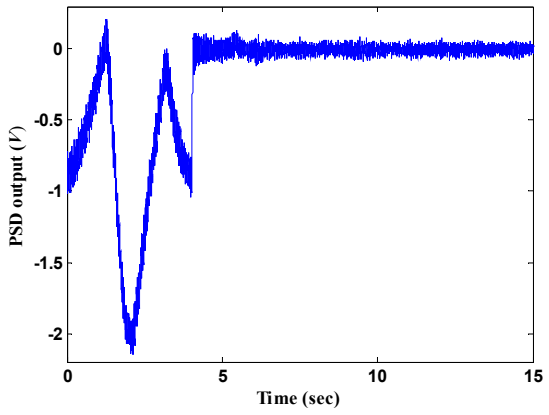

Figure 6-34. XLMS controlling jitter with spacecraft floating with attitude controller

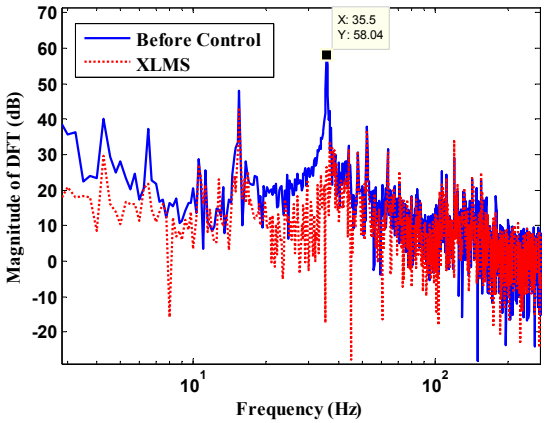

Figure 6-35. DFT magnitude from Figure 6-34

In Figures 6-34 and 6-35, XLMS accurately suppresses the dominant frequency component using 1000 filter weights and a 0.001 adaptive step gain. Although XLMS serves its initial purpose by rejecting the dominant frequency term, it fails to suppress the additional 15 Hz component that appeared when floated. It may be that after a sufficient amount of time for convergence of the weights, the XLMS algorithm will be able to successively reject this 15 Hz component as well.

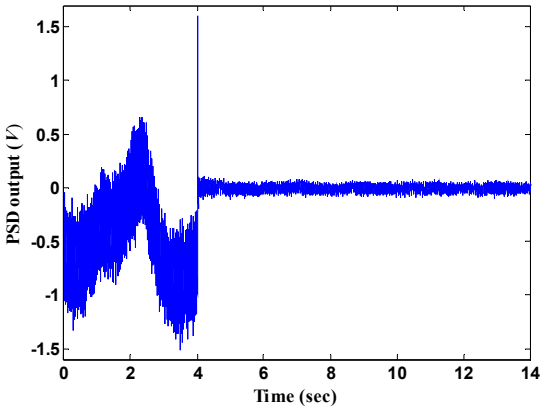

Figure 6-36. MPC controlling jitter

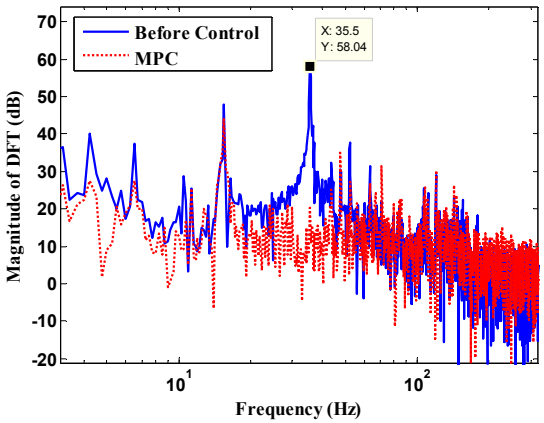

Figure 6-37. DFT magnitude of Figure 6-36

MPC in Figure 6-36 and 6-37 creates a notch feature around the dominant frequency component displaying perfect disturbance rejection for the frequency component of interest. MPC uses 200 past time steps and 10 time steps for the length of the prediction horizon that starts after 2 steps of the current time step. ABM in Figures 6-38 and 6-39 perfectly addresses the dominant peak, and also a large portion of the broadband disturbance as well. ABM uses the same design parameters of that of the preliminary case.

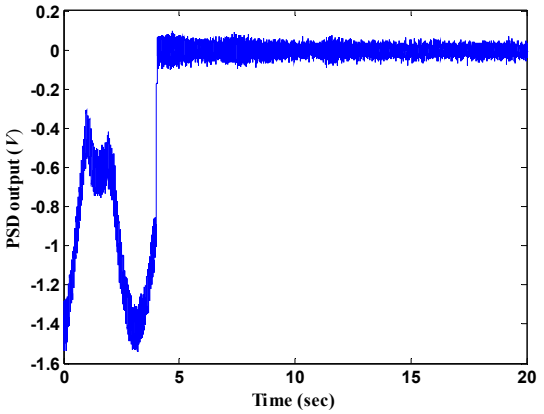

Figure 6-38. ABM controlling jitter

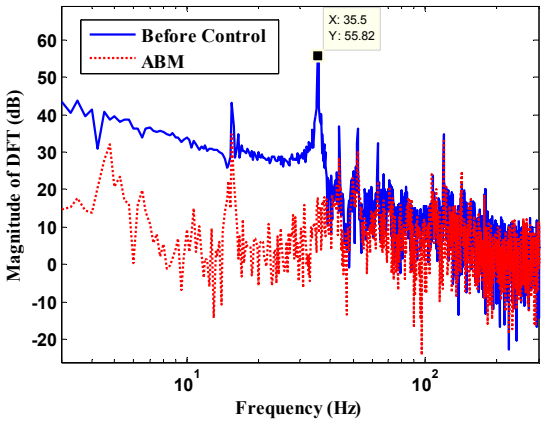

Figure 6-39. DFT magnitude of Figure 6-38

6.6 CONCLUSIONS

To successfully relay the beam coming from the source device to the desired target, 0.01 degree accuracy is required by the spacecraft attitude control system of the TAS2 testbed. Once this has been achieved, the dominant error frequency component within the optical jitter is closely correlated to the speed of each CMG, but other unrelated error frequency components are present. The CMG induced optical jitter within the beam is around 184 micro radians, which may vary depending on the gimbal orientation of the CMG's.

MPRC requires accurate period information in order to completely reject jitter. The paper establishes that when all CMGs are running at the same speed, using three identical frequencies MPRC produces decreased sensitivity to accurate knowledge of the period, and is then a competitor to high order RC used for this purpose. In both cases insensitivity to period error or variation is accompanied by additional error amplification at other frequencies due to the waterbed effect. The MBFRC algorithm is shown to require low gain for stability, and this resulted in a failure to stabilize the beam due to attitude variations. Nevertheless, MBFRC manages to reject the dominant frequency component within the optical jitter.

XLMS does a very good job for rejecting all narrowband disturbance frequencies provided that the weights have enough time to fully converge. More weights will provide better performance for the testbed's particularly rich disturbance environment. MPC and ABM both show superior disturbance rejection capabilities for the dominant frequency component. XLMS, MPC, and ABM all have trouble addressing the lower frequency peak that appeared when the testbed was floated. It is possible that all three methods need more time to accurately characterize is low frequency due to the relatively high sample rate. If the disturbance period for the low frequency component that is uncorrelated to the CMG rotation can be determined prior to each experimental run, MPRC would be able to address this frequency with little time needed.

The best disturbance rejection result, which is with ABM, achieved on the AOCoE of NPS TAS2 reduces the jitter to 67 micro radians, about a 66 % overall amplitude reduction.

CHAPTER 7

IMPROVING LASER COMMUNICATION BETWEEN FORMATION FLYING SATELLITES USING REPETITIVE CONTROL FOR JITTER MITIGATION

7.1 INTRODUCTION

Much attention has been triggered towards Mars missions within the spacecraft community after the successful decent and landing of the Mars rover Curiosity. The Curiosity uses its state-of-the-art equipment to collect and process multitudes of data while surveying the planet. Current camera technology allows us to increase the resolution of the image or video taken from the Curiosity. This high definition imagery requires a large data transmission rate, but is currently limited due to the radio frequency (RF) systems being relied upon in space. The example NASA gives is the Mars Reconnaissance Orbiter which is capable of transmitting data up to 6 Mbps. Laser communication systems (or LaserCom) would increase this rate to 100 Mbps and therefore making it possible to transmit HD video.

Opposed to RF where pointing accuracy of the transmitting signal is less crucial, LaserCom requires a combination of accurate performance in both formation flying between satellites that compose the communication link and acquisition, tracking, and pointing (ATP) technologies for spacecraft as well. Spacecraft often have multiple rotating parts such as CMG's, reaction wheels and momentum wheels. Slight imbalance within any of these devices will cause vibration of the spacecraft structure that can be transmitted to the payload where optical elements are mounted for purpose of LaserCom. The vibration will cause the optical elements to shake, thus creating an

angular deviation in the propagating beam known as optical jitter which can potentially disrupt the communication link.

The Naval Postgraduate School (NPS) Three-Axis Spacecraft Simulator (TAS2) is designed for developing and validating ATP technologies for the Bifocal Relaying Mirror Spacecraft (BRMS), which has a similar concept to that of LCR. A previous paper (Ref. [28]) written by the authors show experiments correcting jitter that was naturally induced by the imbalance within the CMG's of the TAS2 tested while floating on top of a pressurized air bearing. The goal of the experiments was to suppress jitter within the beam on board of the spacecraft starting from the receiving telescope up to the beam splitter within the optical path. Five control algorithms were evaluated where the two non-adaptive control laws only had information on the primary frequency component of the disturbance. Under the given conditions of the testbed it was shown that the Clear box algorithm incorporated with the Adaptive Basis Method was able to produce the best results for jitter suppression on the TAS2 testbed.

Despite providing intuition on how each control method would address the given disturbance situation, the experimental setup was incapable of addressing the true problem of LCR in the absence of line-of-sight (LOS) tracking. This paper will show modifications to the existing optical scheme of the TAS2 that was motivated by a lunar Lasercom setup presented by NASA (Ref. [58]). The paper demonstrates the effectiveness of the modifications made on the testbed by showing experimental results of significantly reducing target error.

As an additional effort to the previous paper mentioned above, the sub-peaks of the frequency spectrum within optical jitter are investigated in detail through modal surveying analysis as an attempt to indentify reoccurring vibration modes. The determined frequencies will be supplied to a recently developed method of Multiple-Period Repetitive Control (MPRC)

where the width of each notch could be adjusted according to the amount of period uncertainty that exists (Ref. [57]). High peaking transients tend to exist when implementing this method and a new technique is introduced here to avoid such detrimental occurring. MPRC will serve as a representative of non-adaptive control laws here and will be compared to adaptive control laws such as adaptive Filtered-X LMS/RLS through a spectrum of different cases. The different cases are provided so that it is understood what the limitations and advantages are for each control law when addressing optical jitter. The best control algorithm for a specific situation can be chosen by relating to the cases discussed here.

7.2 TRUE SCENARIO AND MODIFICATIONS TO PREVIOUS EXPERIMENTAL SETUP

7.2.1 True Scenario

An LCR operation may consist of several satellites depending on the specific mission. In this paper we arrange a scenario such as Figure 7-1 showed below.

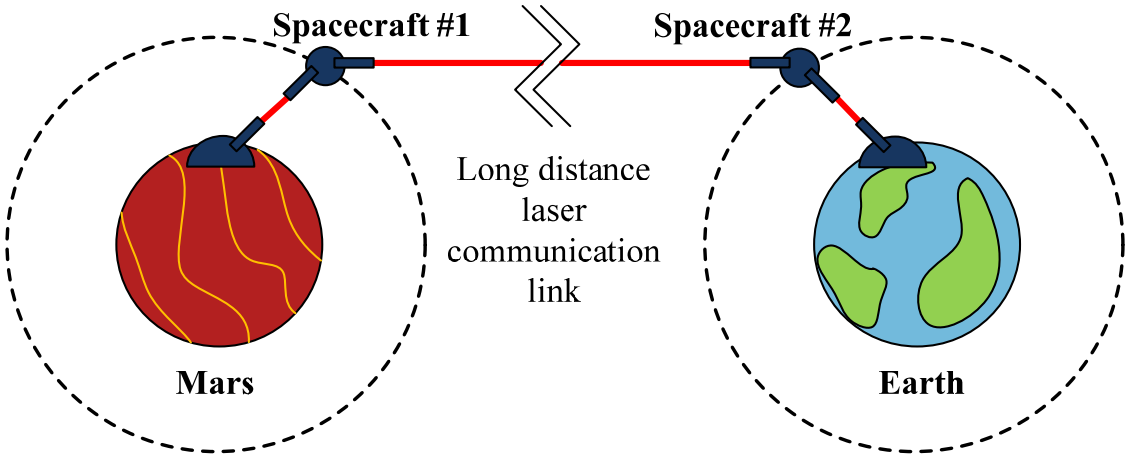

Figure 7-1. LCR between Mars and Earth

Two laser communication links are established between the communication towers and their respective satellites orbiting around Mars and Earth. A long distance interplanetary communication link exists between the two satellites and can easily be disrupted by even the smallest angular deviation within the transmitting beam. Rotating devices such as CMG's and reaction wheels can induce vibration onto the spacecraft which makes optical jitter a common problem in LCR. In this paper the TAS2 testbed is tailored in the direction of improving pointing accuracy within the interplanetary communication link of the current LCR operation scenario. Although formation flying between the two satellites plays a key role in this operation, we replace this with a simpler spacecraft attitude regulation problem for the experiments.

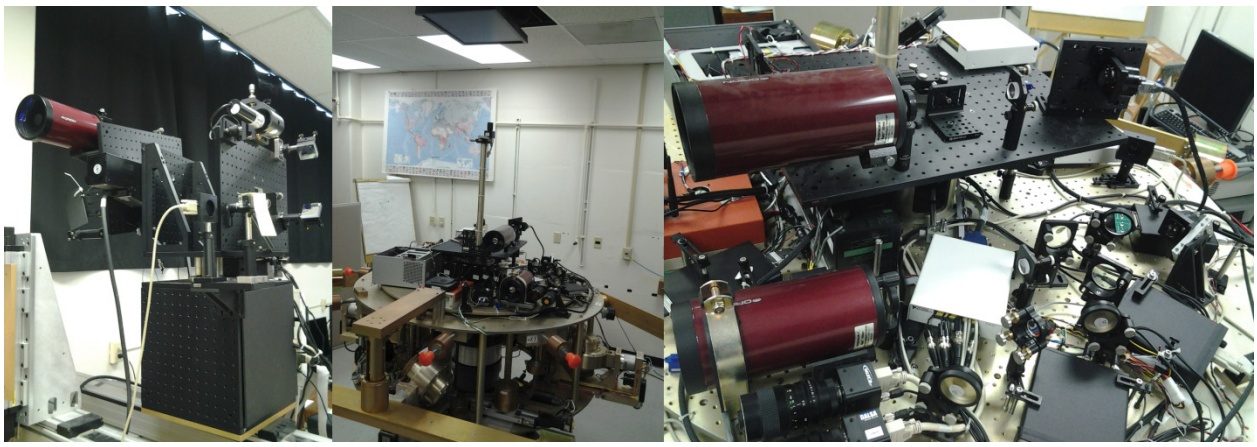

Figure 7-2. Source tower, target laser beacon, and TAS2 tesbed

The experimental setup is shown above in Figure 7-2. The TAS2 represents Spacecraft #1 of Figure 1, which is shown in the middle of Figure 7-2. The source tower represents the one on Mars shown in the left picture with the telescope in Figure 7-2. The target located near the source tower in Figure 2 will represent Spacecraft #2, and the objective of the testbed is to mitigate errors measured at this target so that disruption within the interplanetary communication link is avoided.

7.2.2 Previous Hardware Setup

Reference [28] shows that the TAS2 can successively relay a beam coming from a source towards a target by using attitude control through CMG's. Information on what direction the spacecraft should point to for relaying was provided by an onboard star tracker unit. In a sense, LOS tracking of the target was coarsely achieved limited by the accuracy of the star tracker and bandwidth of the CMG actuators. Control algorithms were capable of suppressing jitter and any error left from coarse tracking with a tip/tilt Fast steering mirror (FSM) based on measurement readings of a Position sensing device (PSD). Unfortunately from an optical perspective the previous optical scheme does not pay attention to line-of-sight (LOS) error from the target in which case the error reduction performance is significantly degraded compared to the jitter suppression on board of the spacecraft platform. In addition to not having LOS tracking abilities, the control loop of the previous setup would not be able to correct for jitter occurring within the optical path beyond a certain optical element, which is referred to as a common and uncommon path problem in optics. Modifications are made here as an attempt to resolve these issues and will be described within the following.

7.2.3 Target Laser Beacon System

In order to provide information to the optics of TAS2 regarding the desired LOS of the target, a laser beacon system was newly constructed at the target or Spacecraft #2. The optical scheme of the laser beacon is shown below in Figure 7-3 along with the actual setup.

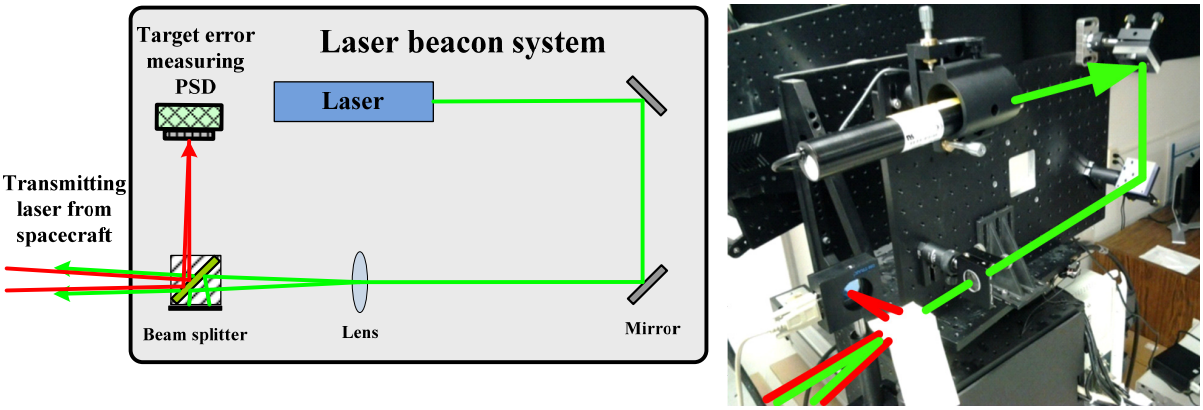

Figure 7-3. Optical scheme and actual setup for the laser beacon system at target (Spacecraft #2)

Instead of directly measuring target error from the beam transmitting from the spacecraft, a beam splitter is placed in front of the target PSD so that the laser beacon beam is able to propagate through the path of the transmitting beam in the opposite direction. The laser beacon is a diverging beam which allows the beam to enter the transmitting telescope of the TAS2 with less required pointing accuracy. After diverging from a point source the size of the beacon beam upon arrival well exceeds the size of the transmitting telescope's aperture and therefore makes the desired LOS insensitive to jitter occurring within the laser beacon system. The laser beacon within the true scenario is shown below in Figure 7-4.

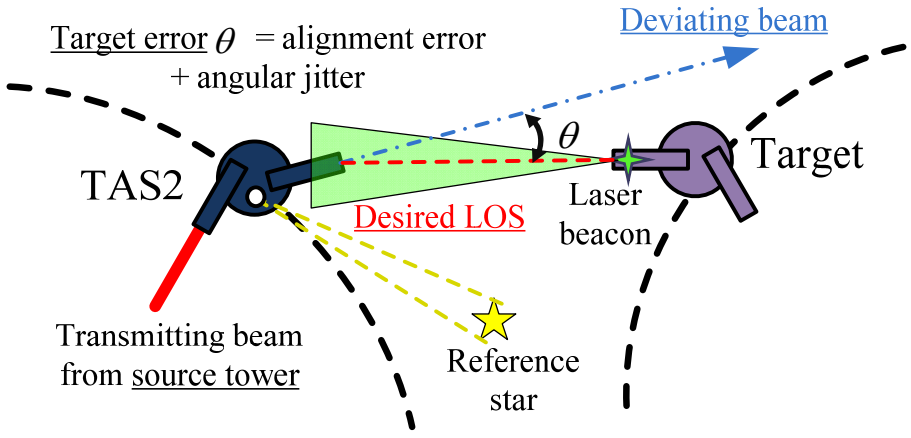

Figure 7-4. The laser beacon in the true application scenario

7.2.4 Target Track Loop

Now that the desired LOS of the target has been provided to the optical system of the TAS2, an additional control loop must be introduced to the existing optical scheme to correct for any LOS error. This new optical scheme rearranges the position of the beam splitter and introduces an additional FSM - PSD pair to the system which composes the target track loop shown in Figure 7-5. Although it will not be dealt here in detail, two lenses are integrated to the setup for relaying the pupil plane of the receiving telescope's primary mirror to FSM #13 in Figure 7-5. The target track loop was motivated by a setup proposed by NASA shown in Figure 7-6. Instead of using an Inertial Reference Unit (IRU) such as the NASA scheme (Ref. [58]), the TAS2 will rely on a bright beacon source as mentioned previously. The laser communication satellite shown in Figure 7-6 does not relay the beam, yet transmits the beam from its own onboard laser source making the setup relatively simple.

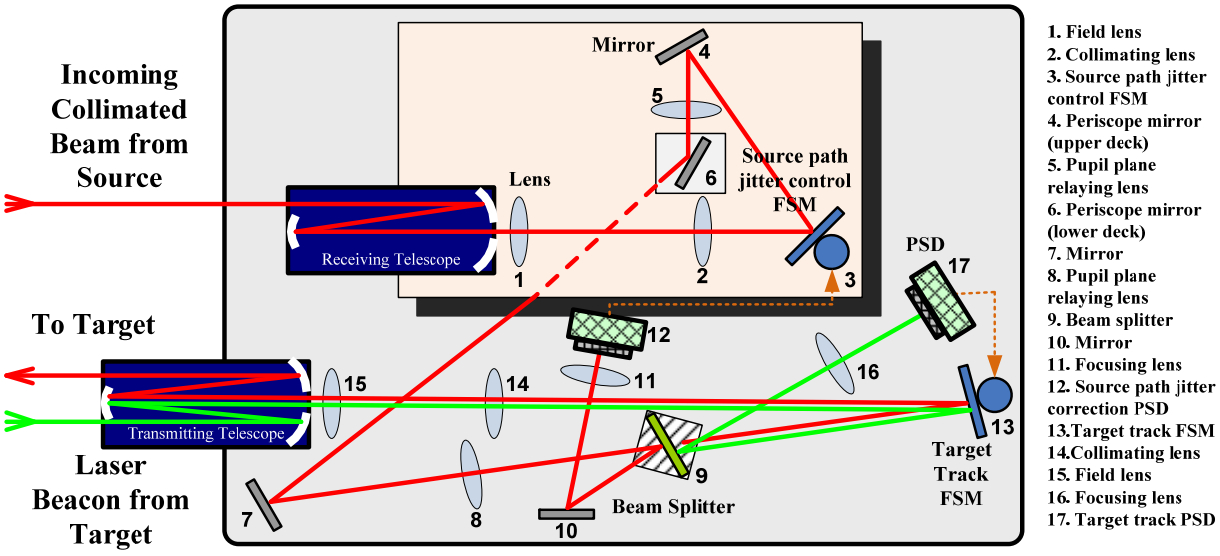

Figure 7-5. Optical setup for TAS2

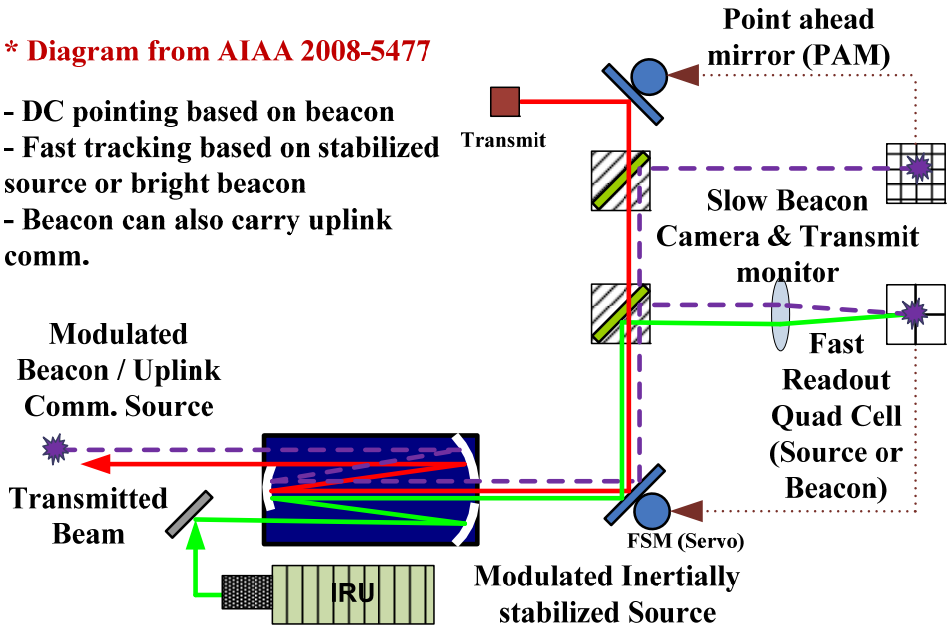

Figure 7-6. Optical setup for NASA

Owing to its relatively long optical path and beam relaying capabilities, the TAS2 has two control loops within its optical scheme. The source path jitter correction loop and the target track loop. The former loop is closed by FSM #3 and PSD #12 in Figure 7-5. The objective of this control loop is to transmit the beam from FSM #13 in the direction normal to the aperture plane of the telescope free of jitter. However, optical jitter occurring between FSM #13 and the transmitting telescope cannot be corrected by the source path jitter correction loop, which leaves a blind spot for jitter correction. Another issue takes place as a result of spacecraft attitude control error or coarse-LOS tracking error. Since the former loop only focuses on transmitting the beam normal to the aperture plane of the telescope, the transmitting beam would not be able to point towards the target if the spacecraft were to oscillate about the desired spacecraft orientation or have coarse-LOS error as shown in the scenario of Figure 7-4. PSD #17 of Figure 7-5 is aligned so that the beam is centered when the incoming beam is normal to the aperture plane of the transmitting telescope. Any LOS error will be detected by PSD #17 and FSM #13

will be able to provide the correct amount of tip/tilt necessary for LOS tracking of the target. Nonlinearities were detected within the FSM of the previous paper. The two FSM's are replaced with Optics in Motion FSM's for linear performance.

7.3 TARGET ERROR SUPPRESSION EXPERIMENTS WITH NEW OPTICAL SCHEME

The previous item focused on explaining the modifications and how they comply with the true application scenario. The following section will evaluate the effectiveness of the modifications by performing two types of experiments. The first experiment is performed for the purpose of evaluating the correlation between the onboard jitter rejection performance and the target performance. The second experiment takes the evaluations from the previous case into account and provides the best results conducted.

7.3.1 Sequence of Sub-tasks for Reducing Error in Interplanetary Link

In order to establish the interplanetary communication link shown in Figure 7-1, a series of sub-tasks must be executed in sequential order. The rotors of the CMG's in the TAS2 are spun up to its ideal speed of 35.5 Hz. The TAS2 is floated on its air bearing and the spacecraft attitude controller is turned on with a sample rate of 40 Hz. The star tracker unit estimates the current-time-step orientation of spacecraft by implementing the QUEST algorithm (Ref. [51]) for coarse-LOS target tracking. Figure 7-7 shows the four quaternion components converging to $[0000]^T$, which is the desired orientation for the spacecraft for coarse-LOS target tracking. Once the attitude controller settles at 50 seconds the two telescopes of the TAS2 roughly lock on to the source tower and target spacecraft respectively so that the beam is relayed. As an alternative of referring to the quaternion components of the star tracker, the alignment of the beam can be

roughly verified by observing the beam of the transmitting telescope shown in Figure 7-8. Once the pupil of each telescope matches up, the transmitting beam assumes the shape of a donut shaped image. The progression of the beam aligning by the attitude control law is shown at the bottom of Figure 7-8. Both source path correction loop and target track loop are turned on simultaneously mitigating error at the target. The target is located 29 ft from the TAS2. One the beam is relayed the target PSD is able to calculate the error due to jitter. Based on the readings of target PSD and physical size of sensor the angular jitter is calculated to be 68 micro radians. The target spacecraft were to be 1000 km away, the transmitting beam would be jittering 68 meters from the center of the target.

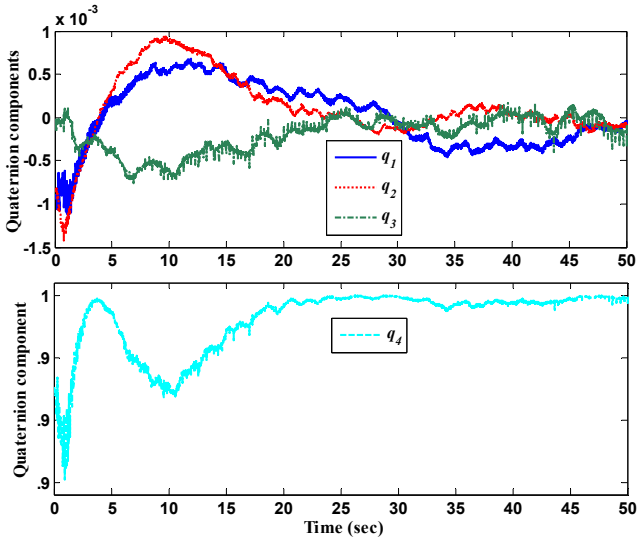

Figure 7-7. Quaternion components from star tracker

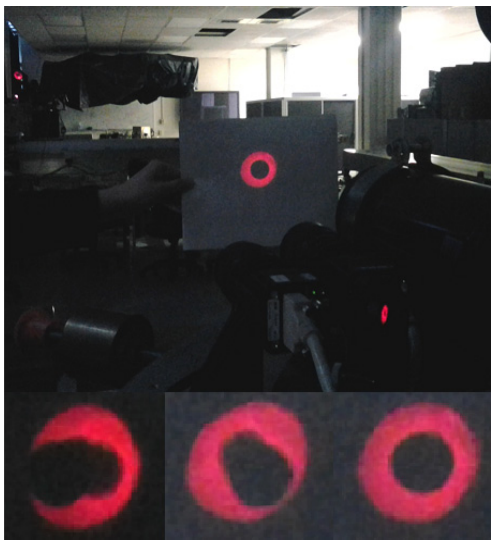

Figure 7-8. Matching the 2 pupils of the receiving and transmitting telescope for beam alignment

7.3.2 Performance Correlation Between Onboard Rejection and Target Error

Reference [28] conducts jitter suppression experiments for several different control algorithms such as MPRC, Adaptive Filtered-X LMS, and the Clear box algorithm associated

with Adaptive Basis Method (ABM). The reader may refer to the previous paper for more detail about these algorithms. In order to evaluate the performance correlation between onboard rejection and target error, we aim for aggressive annihilation of the primary peak within the disturbance spectrum and compare results between the target and onboard readings.

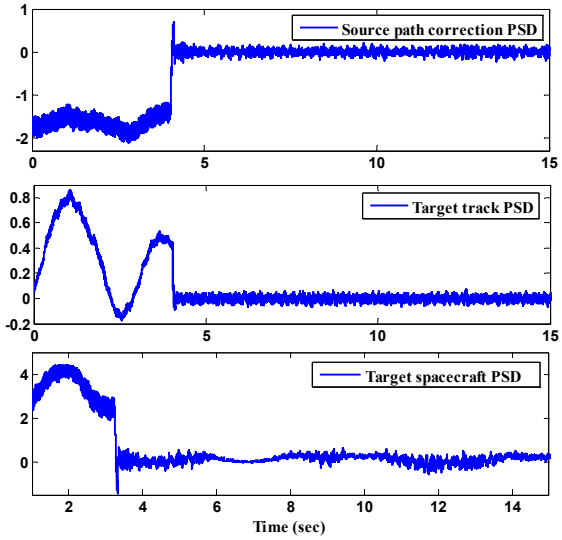

Figure 7-9. Error [*V*] in the time domain (MPRC*i*)

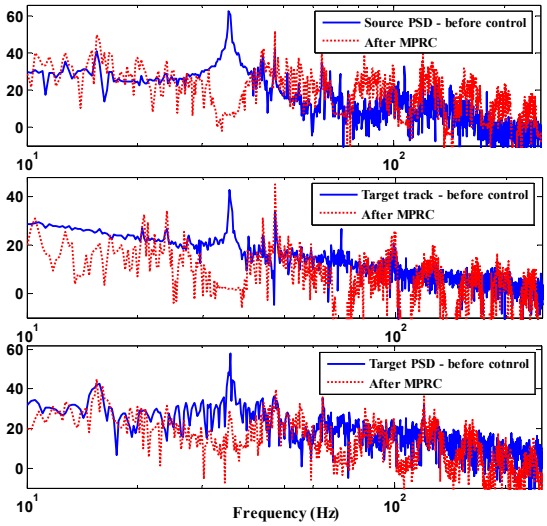

Figure 7-10. DFT magnitude (dB) of Figure 7-9

Among the algorithms that were previously implemented we select MPRC that addresses the primary peak by three times. This special configuration was referred to as MPRC*i* from Reference [57], and was selected due to its capability of suppressing the designated frequency component and the neighboring frequencies which makes the performance observation more convenient. More detailed explanation on the implementation of MPRC*i* will be mentioned within later sections. Figure 7-9 shows the PSD readings of the source path correction loop, target track loop, and the target starting from top to bottom. Both control loops are turned on at 4 seconds and the target starts to log data a second later. The target error readings show small low frequency variation even after control. This is likely to occur even for small inaccuracies that exist in pupil plane relaying within the target track loop or due to non-common path and

common path issues. Figure 7-10 shows the respective Discrete Fourier Transform (DFT) magnitude of the error from Figure 7-9. Deep notches are formed at the primary peak of 35.5 Hz for both source path and target track loop. Classic example of the waterbed effect is displayed as the unaddressed frequencies are amplified. The target PSD however shows a small peak at the primary frequency within the notch despite having aggressive suppression done by both onboard control loops. A possible cause for this phenomenon is when there is overcompensation done by the FSM's due to common and non-common path issues within the optical setup. To be more specific, there can be a situation where the detected jitter is induced by an optical component that does not lie within primary path of the transmitting beam. Correcting for this jitter would actually induce jitter on to the transmitting beam of the primary path by overcompensation. Overcompensation of jitter can occur when components #9, #10, #11, and #12 vibrate within the source correction path in Figure 7-5. It also occurs within the target loop when #9, #16, and #17 tend to vibrate as well. Although the non-common path issue is inevitable for most optical schemes, it is important to passively damp these components as much as possible to avoid overcompensation of jitter.

7.3.3 The Effectiveness of the Modified Scheme

The previous performance evaluation provides insight about possible overcompensation of jitter. From a control perspective it may be better performance-wise to be less aggressive in control action within the target track loop so that there can be less jitter overcompensation due to the non-common path issue of the optical setup. Although this is not necessarily true it is shown here that significant error reduction can be achieved by somewhat agreeing to this logic. Figure 7-11 shows ABM applied to the source path correction loop at 4 seconds, and FXLMS applied to the target track loop at 4 seconds as well. The second subplot of Figure 7-12 shows that FXLMS

has not fully addressed the primary peak within the target track loop opposed to the source path loop where ABM was capable of thoroughly annihilating this peak. Nevertheless the third subplot of Figure 7-12 shows that the primary peak and secondary peak of 15.5 Hz of the target error has been significantly rejected. The most bottom subplot of Figure 7-11 overlays both results of jitter mitigation with and without the laser beacon. The contrast is significant and shows much improvement by using the laser beacon and target track loop. In this particular case the resulting control action taken onboard the spacecraft was in favor of the current non-common path issue within the optical setup of the TAS2.

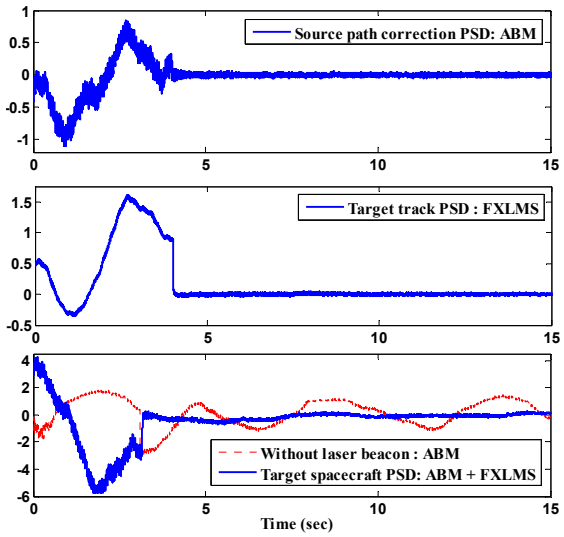

Figure 7-11. Error [*V*] in the time domain

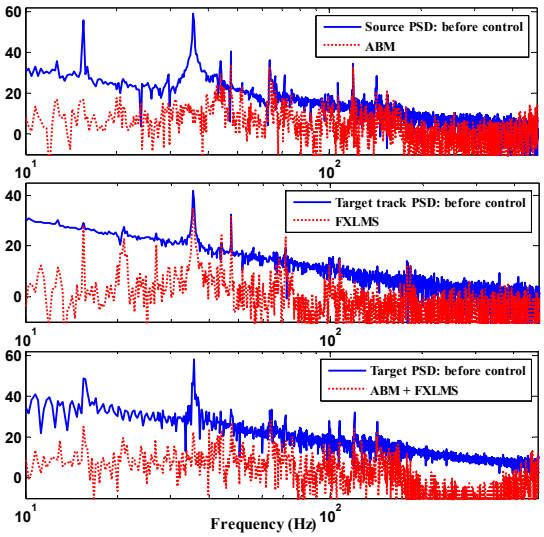

Figure 7-12. DFT magnitude (dB) of Figure 7-11

The second and third plot of Figure 7-12 both show a flattening profile within the low frequency range which implies that the target track loop has achieved its primary goal of addressing LOS error due to spacecraft attitude pointing inaccuracies. However, as shown within the correlation performance analysis of the previous item, the target track loop is reluctant to correcting for jitter within its path due to overcompensation of control action. It is possible that jitter mitigating capabilities of the target track loop can improve when components #9, #16, and #17 are better

isolated from mechanical vibration of the spacecraft so that jitter correction is less effected by the non-common path issue.

7.4 MODAL SURVEYING AND IDENTIFYING OPTICALLY SIGNIFICANT VIBRATION MODES

Reference [28] shows how five control algorithms address the primary peak of the disturbance that is correlated to the rotor speed of the CMG's. However, the frequency spectrum of the disturbance signal consists of multiple sub-peaks that cannot be addressed by non-adaptive control laws without prior information of these peaks. It is the purpose of this item to investigate these sub-peaks in detail as an attempt to identify reoccurring optically significant vibration modes. The identified vibration modes can be applied to non-adaptive control laws so that the disturbance rejection performance can be maximized.

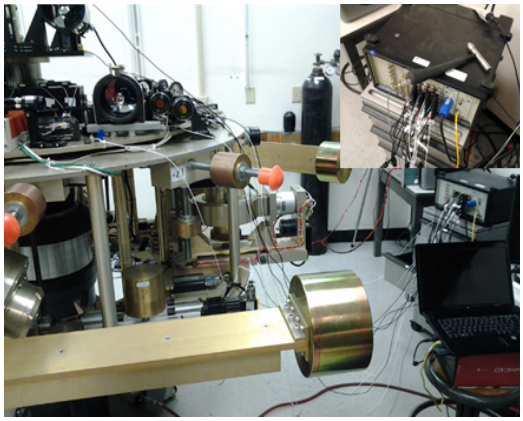

Figure 7-13. PULSE Multi-analyzer system type 3560D and impulse hammer for modal surveying analysis

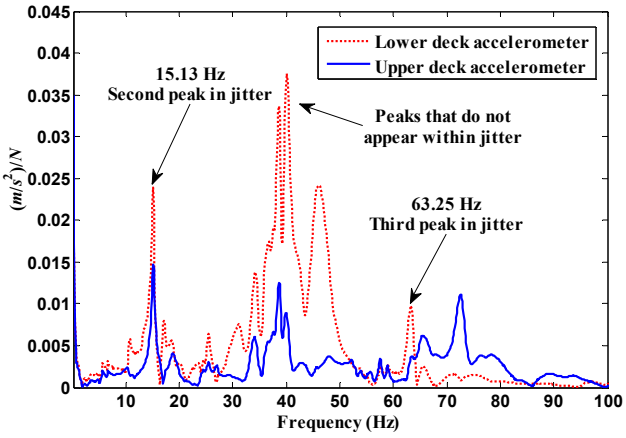

Figure 7-14. Modal analysis frequency response $(m/s^2)/N$ results of TAS2 structure

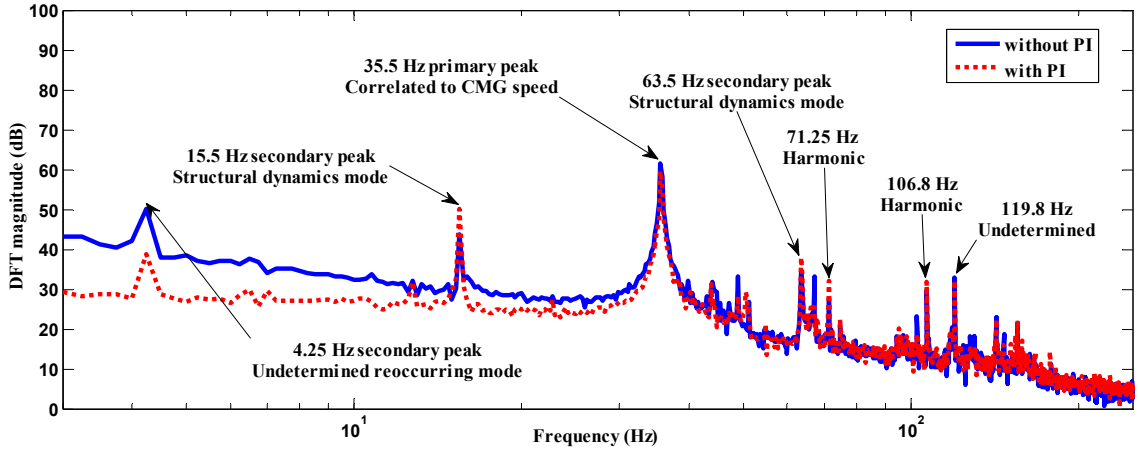

Figure 7- 15. Reoccurring modes within averaged-DFT magnitude (dB) of jitter from source path PSD

The PULSE Multi-analyzer system type 3560D was used for identifying structural vibration modes of the TAS2 testbed shown in Figure 7-13. The analyzer device itself with the impact hammer is located on the right top corner of Figure 7-13. Our interest is in the structural vibration modes that induce jitter to the beam. Therefore, the probes or accelerometers of the analyzer were positioned on the optical path near each optical component in order to examine structural modes that excite or shake these components. 24 channels consisting of 23 accelerometer readings and 1 impulse hammer reading were used within the PULSE Multi-analyzer system when performing an impulse response test with the PULSE 15.1 software. The TAS2 was floated with the CMG's turned off when conducting the impulse test. The PULSE software would calculate the frequency response $(m/s^2)/N$ of the TAS2's structural dynamics after every impact of the impulse hammer. The frequency response was averaged after a total number of five impacts. Two accelerometer readings respectively located on the upper and lower deck of the TAS2 were selected, and the frequency response for each unit was shown in Figure 7-14. The 15.13 Hz peak within this plot identifies the undetermined 15.5 Hz second most dominant peak within jitter that was questioned by the former paper from reference 4. The small

discrepancy between the frequency detected within jitter and frequency from modal surveying can be due to the accelerometer itself adding up to the dynamics of the structure. The 63.25 Hz peak was identified and it will be shown later to be one of the reoccurring modes within jitter with considerable amplitude. One can pay attention to the fact that the 63.25 Hz modes appears within the lower deck but not the upper deck. Nevertheless the 63.5 Hz peak will appear within the PSD reading due to the optical jitter's nature of accumulating within the beam propagating throughout the entire optical path. Despite the effort of determining the 15.5 Hz vibration mode, modal surveying is not considered the best way for determining optically significant vibration modes. Modes located between 33 and 48 Hz within Figure 7-14 do not manifest themselves within jitter of the transmitting beam. In most cases optical components such as lenses are very sensitive and cannot adhere directly to foreign objects. Even if the probe could be attached to optical components, the extra dynamics added to these components may dominate the response giving false information about the system. Instead, a more accurate option would be a Laser Doppler vibrometer for surveying vibration modes that exist within large and sensitive optics.

A more direct approach was taken for determining the reoccurring modes within jitter. The TAS2 was floated while the attitude controller was turned on. After the attitude settles the beam would align itself and data would be collected for 10 seconds from the source path PSD. This process would be iterated ten times. The DFT magnitude of each data set was averaged and shown in Figure 7-15. One curve displays raw DFT data that includes jitter and the low frequency variation due to attitude control error. The other eliminates the bias by implementing a crudely designed Proportional Integral (PI) control law through the source path jitter correction FSM. More attention is paid to the second curve as upcoming sections will show experimental results performed with control algorithms that are implemented with a PI controller. According

to Figure 7-15, starting from the most dominant to least dominant, the reoccurring modes within the disturbance are 35.5, 15.5, 63.5, 4.25, 71.25, 106.8, 119.8, and 50.5 Hz where 71.25 and 106.8 are harmonics of the primary peak 35.5 Hz. These modes will be considered as prior knowledge of the disturbance environment and applied to MPRC which serves a representative for non-adaptive control laws.

7.5 BASE CASE COMPARISON BETWEEN MPRC AND ADAPTIVE FILTERS

Reference [28] focuses on rejecting the primary frequency component in jitter while no particular action was taken for the sub-components within the disturbance. Adaptive control laws such as Filtered-X LMS (XLMS), Model Predictive Control (MPC), and the Clear box algorithm associated with the Adaptive Basis Method (ABM) show significant disturbance rejection performance at the primary peak, but display less aggressiveness towards the sub-peaks. Nevertheless, the overall error is reduced substantially. MPRC on the other hand shows amplification at unaddressed frequencies due to the waterbed effect which degrades the overall error reduction performance. A previous paper (Ref. [57]) provides a method for implementing MPRC*i* for multiple periods and demonstrates the ability to minimize amplification at unaddressed frequencies by tuning the RC gain. Since the identified optically significant modes by modal surveying were in fact averaged from multiple data sets, there lies an uncertainty within the majority of the modes which makes the proposed method ideal for the given situation.

Three case comparisons will be made between non-adaptive and adaptive control laws to determine the extent of each control law's capability. MPRC is chosen to represent the former, while XLMS is chosen for the later. The reader can refer to Reference [28] for more detail. Experiments will be conducted within the source path jitter correction loop of the TAS2 while

the attitude control law is turned on for coarse target tracking. Jitter control begins after alignment settles.

7.5.1 Nesting a Crudely Designed PI Controller within the Inner Loop

The first class of comparisons is based on having a crudely designed PI controller nested within the inner loop of each control algorithm. The purpose of the PI controller is to merely eliminate bias within the error so that the beam is stabilized from low frequency variations due to attitude control error of the spacecraft. This example should make the disturbance peaks more distinguished as shown within Figure 7-15 and makes it convenient for observing the reduction rate of each peak within the frequency spectrum.

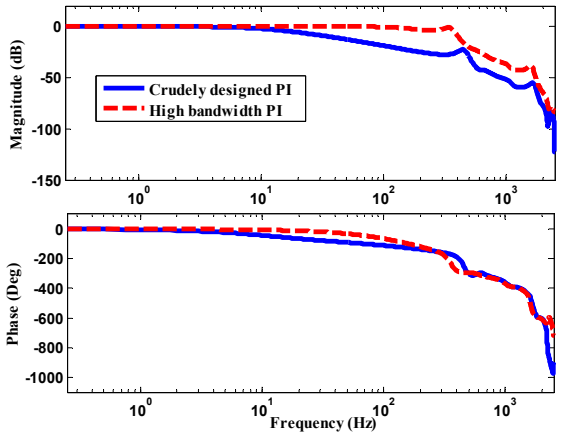

Figure 7-16. Magnitude and phase response of crudely designed PI and high bandwidth PI

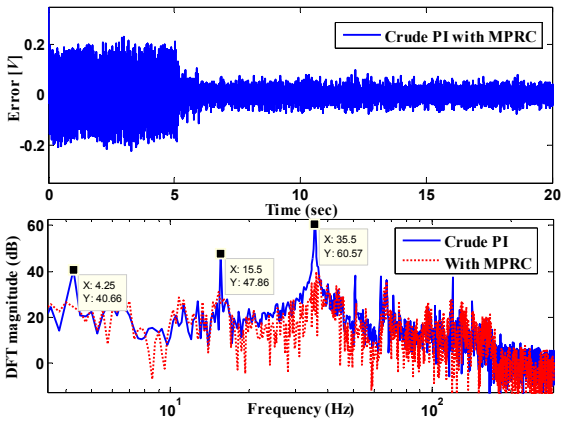

Figure 7-17. MPRC*i* addressing frequency components identified by modal surveying

Figure 7-16 shows the frequency response of the FSM to PSD plant with a crudely designed PI controller. The 3 dB bandwidth is 12 Hz which implies that the PI controller will function more or less as a bias eliminator for the given situation. The PI feedback loop is turned on immediately once data is collected from the source path PSD. Figure 7-17 shows results of MPRC*i* turned on at 5 seconds addressing the optically significant vibration modes. The MPRC

implements 13 individual RC laws in total where the primary peak is addressed with a 3-period MPRC*i* law to provide more robustness to the period fluctuation and all other components are addressed with 2-period MPRC*i* laws. According to Figure 7-17 we can see that the overall error is significantly reduced. However, the primary peak has not been aggressively notched out due to the small RC gain of 0.08 used for avoiding sever amplification at unaddressed frequencies. More detail is provided in Table 7-1 to show the reduction rate of each component being addressed. The RMS error for the last 2 seconds is 0.0211.

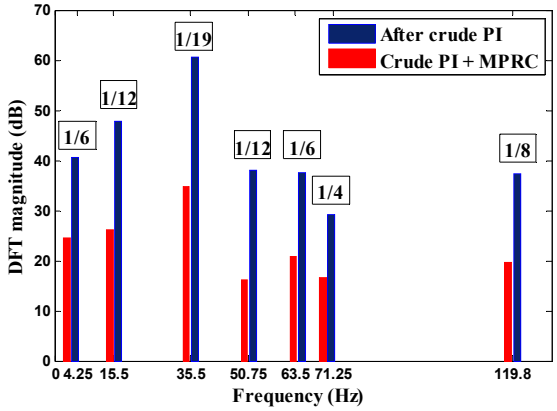

Figure 7-18. Reduction rate of each frequency component when implementing MPRC

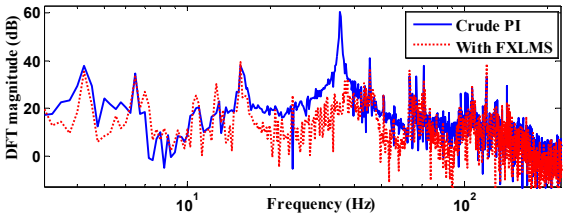

Figure 7-20. FXLMS with different rejection characteristics

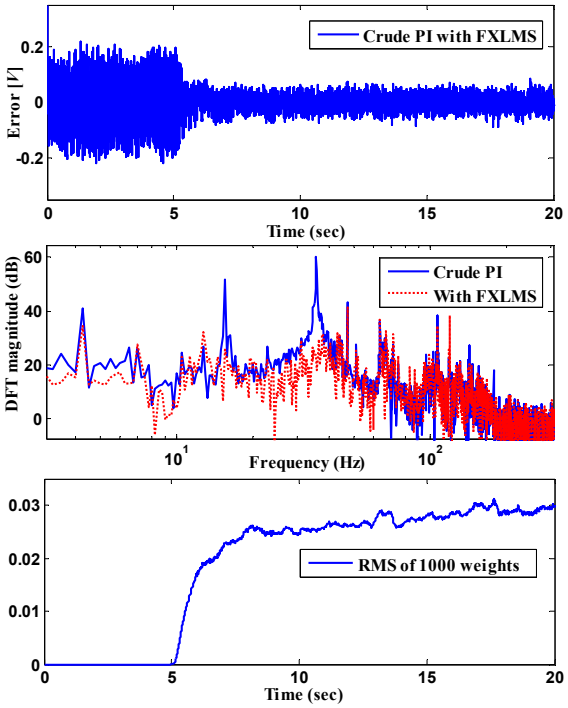

Figure 7-19. FXLMS with 1000 weights

Figure 7-19 shows jitter control results of FXLMS implemented with the crudely designed PI controller. In theory an FIR filter has the capability of rejecting one sinusoidal signal per two weighted tapped delays. The number of weights chosen here for XLMS is 1000, which means the adaptive FIR filter can theoretically produce a compensating signal containing up to 500

sinusoidal signals. The high order was chosen due to the richness of the frequency components within jitter detected by the PSD. A step gain of 0.001 was chosen to stabilize FXLMS. Although the stochastic gradient algorithm of FXLMS is not designed to eliminate specific peaks within the frequency spectrum of the disturbance, the middle plot of Figure 7-18 shows that FXLMS significantly rejects the two most dominant peaks, which are 35.5 and 15.5 Hz. Rejection at other secondary-peaks are hard to notice despite the fact that the bottom plot of Figure 7-19 shows nearly converged weights. The RMS of the weights is plotted to avoid complication of showing a 1000 weights. As mentioned before FXLMS adapts weights in the direction of reducing the overall error and does not explicitly aim for specific frequencies. Figure 7-20 shows rejection results for a slightly different disturbance environment regarding the size of each peak. The 15.5 Hz before applying FXLMS is not as substantial as the previous case, and FXLMS does not decide to reject this specific frequency component. Nevertheless the RMS errors for the former and later examples are 0.0220 and 0.0207 respectively, which show that the overall rejection performance difference is unnoticeable despite the different frequency components reduction behaviors.

Both MPRC and FXLMS show significant disturbance rejection capabilities. There was no noticeable error mitigation performance difference between the two algorithms based on the RMS computations of the final error. To add a comment, MPRC required an iterative process of tuning the RC gain and then observing the results to obtain this ideal performance. Implementation of FXLMS was relatively less complicated where the only concern was to stabilize the controller by decreasing the step gain.

7.5.2 Nesting a High bandwidth PI Controller within the Inner Loop

This item puts more effort into the design process of the PI controller. The bandwidth is increased as much as possible while avoiding a high resonant peak before the cutoff as shown in Figure 7-16. The -3 dB bandwidth is around 194 Hz, which implies better error reduction capabilities at higher frequencies than the previous PI law. This item will show performance comparisons between the well designed high bandwidth PI controller and the two augmented control laws, MPRC and FXLMS.

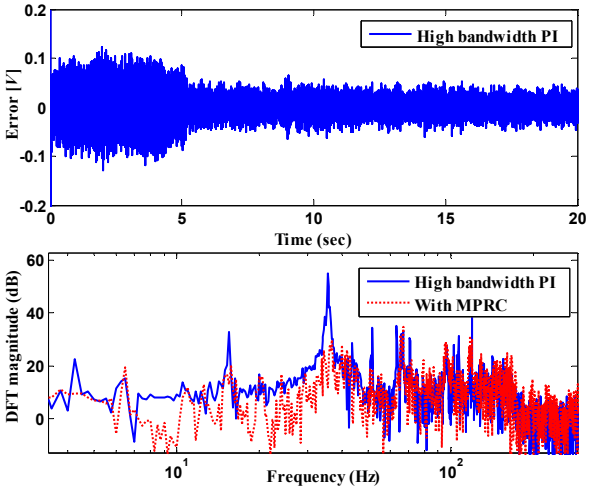

Figure 7-21. MPRC*i* with a high bandwidth PI controller addressing jitter

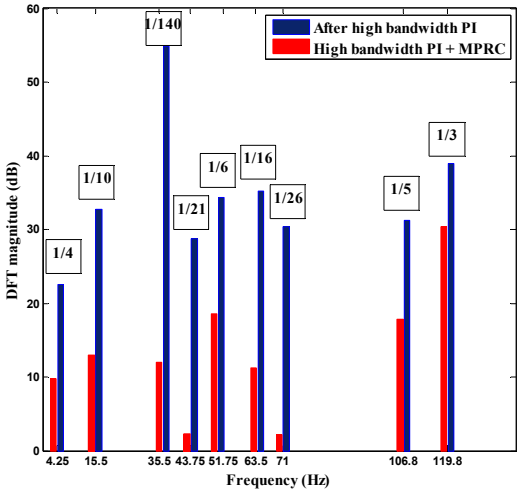

Figure 7-22. Reduction rate of each component in MPRC with high bandwidth PI

Figure 7-21 shows results for implementing MPRC with a high bandwidth PI controller. Despite having a well designed PI controller, MPRC tends to show significant error mitigation capabilities over the conventional feedback control law. Nevertheless the high bandwidth PI does a better job than the former crudely designed PI as one can verify this by comparing the bar charts from Figure 7-18 and Figure 7-22. This particular MPRC design consists of 15 individual RC laws. A 3-period MPRC*i* law was dedicated to addressing 35.5 Hz and associated harmonics, 71 and 106.8 Hz. The disturbance rejection rates of these components are indicated within Figure 7-22. The rest are addressed by 6 sets of two-period MPRC*i* laws. The RC gain used here is 0.09

for maximizing the error reduction performance with an RMS of 0.0136 which shows improvement over the previous case of implementing MPRC with a crudely designed PI controller.

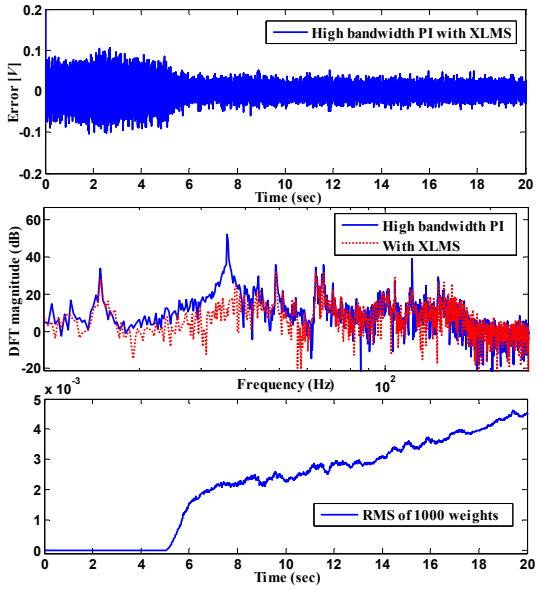

Figure 7-23. XLMS with a high bandwidth PI controller addressing jitter

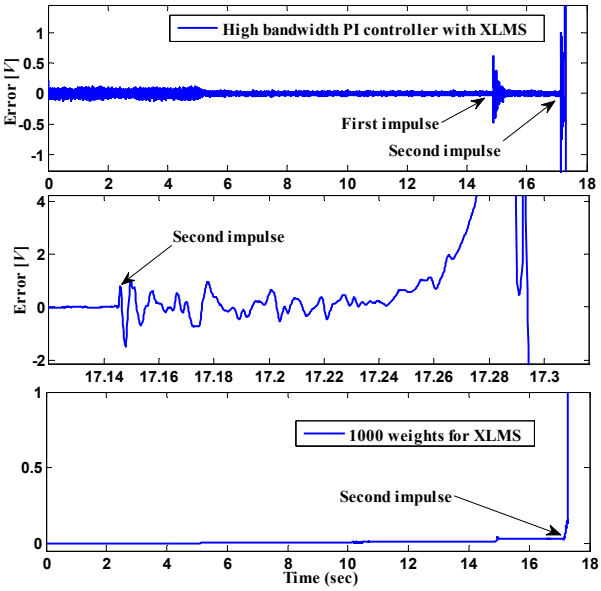

Figure 7-24. XLMS jerk introduced to the disturbance causing instability

Figure 7-23 shows significant jitter mitigation results when implementing FXLMS with 1000 weights. The previous experiments with FXLMS showed disturbance rejection of two peaks, 15.5 and 35.5 Hz. In this case FXLMS decides to address 35.5 and 119.8 Hz, which are the most dominating peaks within the disturbance frequency spectrum shown within the middle plot of Figure 7-23. Although it is as not as rapid as the beginning, the weights of the adaptive filter are still slowly ascending in Figure 7-23. The stochastic gradient method tends to be less rapid in adaptation when error approaches its final value. Therefore it would be possible for more improvement within error mitigation performance if more time was available. The RMS error of FXLMS is 0.0110.

7.5.3 Introducing sudden jerk and fault tolerant behavior

Faults or malfunctioning of mechanical components in spacecraft can introduce an abrupt impulse of jerk to the system. The sudden impulse introduced may cause complex control algorithms to become unstable. The following section will apply an impulse hammer to the optical platform of the TAS2 to evaluate jerk tolerant characteristics.

Figure 7-24 shows results of introducing impulses to the optical platform of the TAS2 addressing FXLMS with 1000 weights and a step gain of 0.003. Two impacts were made and FXLMS goes unstable after the second impulse. The impulse introduced is about five times the size of the disturbance after applying the PI control law. The bottom plot of Figure 7-24 shows that the weights go to infinity after the second impulse showing instability. Stability of the LMS algorithm is defined as

$$0 < \mu < \frac{2}{\lambda_{\max}} \tag{7.1}$$

where μ is the step gain and $\lambda_{\max}$ is the maximum eigenvalue of the autocorrelation matrix of the reference signal (Ref. [43]). The impact hammer introduces a larger signal to the system and results in increasing the maximum eigenvalue $\lambda_{\max}$ for that instance. This decreases the upper bound of Eq. (7.1) and can cause instability when the step gain is big enough to violate the stability condition. In order to be tolerant to such impulses we choose a smaller step gain by setting it as 0.0005. Figure 7-25 shows results of FXLMS with the same impulse tests. FXLMS with a small enough gain is able to maintain stability for the given impulse that was applied. The weights tend to shift higher after each impulse. It is possible that if the impulse being applied was larger, FXLMS with the selected gain of 0.0005 could become unstable yet again.

Figure 7-26 shows results of MPRC with the same impulse tests. Unless the impulse is large enough to saturate the actuator, MPRC will be stable for any type of impulse introduced to the system. The bottom of Figure 7-26 shows the DFT magnitude of the error after the second impulse and demonstrates that MPRC can maintain good disturbance rejection capabilities after jerk has been introduced.

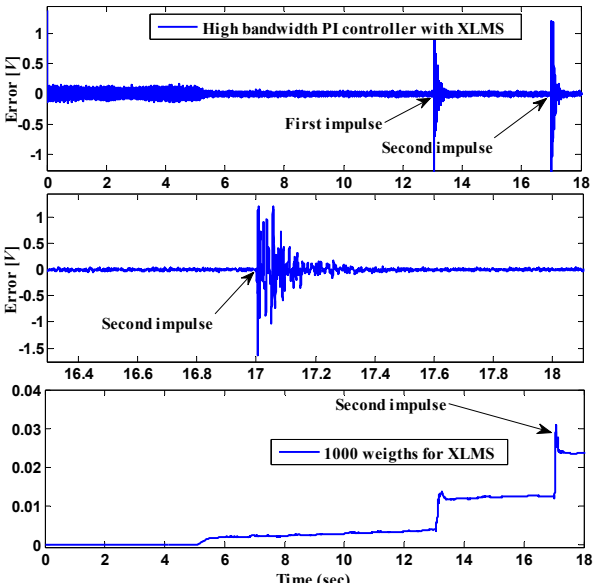

Figure 7-25. XLMS stability robustness to jerk increased by decreasing step gain to 0.0005

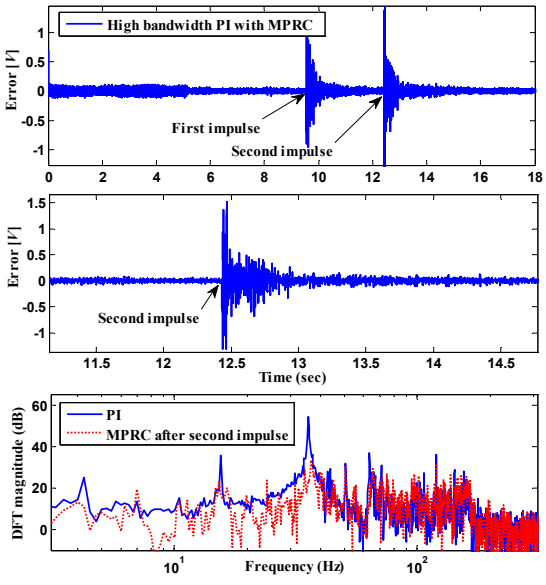

Figure 7-26. MPRC stable against jerk

7.6 CONCLUSIONS

The chapter demonstrates the effectiveness of the modifications made on the hardware which comply with a laser communication satellite scenario [59]. The target track loop successively provides means for target LOS-tracking within the optical scheme. The TAS2's optical scheme demonstrates significant error reduction at the target PSD which represents angular jitter correction within the interplanetary communication link of LCR.

Modal surveying was performed as an attempt to identify reoccurring optically significant vibration modes with the PULSE Multi-analyzer system type 3560D. The purpose of this was to treat the reoccurring modes as prior information for MPRC*i* addressing multiple periods that served as a representative case for non-adaptive type control laws.

A sequential start up method was newly introduced to eliminate high amplitude peaks within the transient response of MPRC*i*. The method was shown to be effective for MPRC*i* implementation in hardware.

Base case comparisons were made for MPRC and FXLMS with respect to jitter mitigation capabilities where the RMS error is displayed for both control laws in Table 7-1.

RMS Error	**Crudely designed PI controller**	**High bandwidth PI controller**	**Stability against jerk**
MPRC	0.0211	0.0136	Stable regardless of jerk
FXLMS	0.0220	0.0110	Use a smaller step gain

Table 7-1. Comparison of final RMS error between MPRC and XLMS

FXLMS is relatively simple to implement and shows substantial error mitigation performance. Although FXLMS does not explicitly aim for any particular peaks within the frequency spectrum of the disturbance, the error is reduced regardless. MPRC after prior identification of the frequency modes can be fine tuned to match the jitter mitigation performance of FXLMS by employing newly developed methods (Ref. [57]) within the complex environment of optical jitter induced by the mechanical vibration of the spacecraft. This newly developed method of MPRC was experimentally validated through these results.

FXLMS can become unstable when an abrupt impulse is introduced to the system, which is a concern for most adaptive-type control laws. The stability robustness to jerk can be increased by decreasing the step gain of FXLMS. However, this does not guarantee stability for a larger impulse applied to the system. MPRC on the other hand does not any significant issues with jerk.

CHAPTER 8

CONCLUSIONS

Multiple-Period Repetitive Control (MPRC) is ideal for situations where the disturbance within the system contains multiple unrelated frequencies and their associated harmonics. Such disturbances can exist in mechanical systems that consist of multiple rotating devices. Chapter 2 explains the underlying mathematics of Repetitive Control (RC) theory including MPRC and Higher Order Repetitive Control (HORC). Basic explanations were given for the design procedure of each RC algorithm as well as respective stability determination methods. The thesis work was progressed based on these mathematical foundations of RC. Chapter 3 analyzes stability robustness characteristics to investigate how model error can harm stability in MPRC. The results provide intuition to the designer for avoiding instability in MPRC or assessing the cause for a currently unstable MPRC system. Newly developed methods address the issue of model error by stabilizing the system with a small RC gain complying with the small gain stability theory for MPRC. Simpler methods were derived for determining stability of MPRC making the use of hardware data for stability determination more reasonable in RC practice. Chapter 4 shows a completely new performance feature within MPRC that produces robustness to period fluctuations or uncertainties when used to address identical periods (MPRC*i*). This feature is similar to that of the existing method of HORC, but is shown to have benefits over it. It was shown that the main advantage of MPRC*i* was that the width of the notch within the sensitivity transfer function could be adjusted by tuning the RC gain. This makes it more practical for producing robustness to period fluctuations when implementing RC within the presence of broadband disturbance. Chapter 5 acknowledges the issue of high peaking amplitudes within the transients of MPRC when addressing identical periods or periods that are

close together. After determining the cause of such anomaly a sequential start up method was introduced to remedy the problem. The method was shown to be very effective by experimental verification. Chapter 6 evaluates five control algorithms by addressing CMG induced jitter on the Naval Postgraduate School's (NPS) Three-Axis Simulator 2 (TAS2) testbed. All five algorithms successively rejected the primary frequency component within the disturbance. However the non-adaptive control laws showed sign of amplification at the unaddressed frequency components due to the waterbed effect. The adaptive control laws on the other hand were not able to completely reject the secondary peaks. The Adaptive Basis Method showed the best results for overall jitter mitigation for the TAS2 testbed. Chapter 7 demonstrates the effectiveness of the modifications made on the TAS2 testbed which comply with a laser communication satellite scenario. Reoccurring modes were identified by modal surveying analysis and DFT averaging. The identified modes were used as prior information for MPRC, and thorough comparison was made between jitter mitigation results of XLMS. All attributes of the theoretical developments made within this thesis were utilized to fully address the complex environment of optically jitter induced by mechanical vibration within the structure of the TAS2 testbed.

REFERENCES

[1] T. Inoue, M. Nakano, and S. Iwai, "High Accuracy Control of a Proton Synchrotron Magnet Power Supply," *Proceedings of the 8th World Congress of IFAC*, Vol. 20, 1981, pp. 216-221.

[2] R. H. Middleton, G. C. Goodwin, and R. W. Longman, "A Method for Improving the Dynamic Accuracy of a Robot Performing a Repetitive Task," *University of Newcastle, Newcastle, Australia, Department of Electrical Engineering Technical Report EE8546*, 1985. Also, 1989, International Journal of Robotics Research, Vol. 8, pp. 67-74.

[3] S. Hara, and Y. Yamamoto, "Synthesis of Repetitive Control Systems and its Applications," *Proc. 24th IEEE Conference on Decision and Control*, 1985, pp. 326-327.

[4] S. Hara, T. Omata, and M. Nakano, "Stability of Repetitive Control Systems," *Proceedings of the. 24th IEEE Conference on Decision and Control*, 1985, pp. 1387-1392.

[5] M. Tomizuka, T.-C. Tsao, and K. K. Chew, "Analysis and Synthesis of Discrete time Repetitive Controllers," *Journal of Dynamic Systems, Measurement, and Control*, Vol. 111, 1989, pp. 353-358.

[6] K. Chew and M. Tomizuka, "Digital Control of Repetitive Errors in Disk-Drive Systems," *IEEE Control Systems Magazine*, Vol. 10, 1990, pp. 1620.

[7] R. W. Longman, "Iterative Learning Control and Repetitive Control for Engineering Practice," *International Journal of Control, Special Issue on Iterative Learning Control*, Vol. 73, No. 10, July 2000, pp. 930-954.

[8] R. W. Longman, "On the Theory and Design of Linear Repetitive Control Systems," *European Journal of Control, Special Section on Iterative Learning Control*, Guest editor Hyo-Sung Ahn, Vol. 16, No. 5, 2010, pp. 447-496.

[9] R. W. Longman, K. Xu, and M. Q. Phan, "Design of Repetitive Controllers in the Frequency Domain for Multi-Input Multi-Output Systems," *Advances in the Astronautical Sciences*, Vol. 129, 2008, pp. 1593-1612.

[10] B. Widrow and S. C. Stearns, Adaptive Signal Processing, *Prentice-Hall*, Englewood Cliffs, New Jersey, 1985.

[11] S. J. Elliott, I. M. Stothers, and P. A. Nelson, "A Multiple Error LMS Algorithm and its Application to the Active Control of Sound an Vibration," *IEEE Transactions on Acoustics and Signal Processing*, Vol. 25, No. 6, 1977, pp. 484-491.

[12] S. G. Edwards, B. N. Agrawal, M. Q. Phan, and R. W. Longman, "Disturbance Identification and Rejection Experiments on an Ultra Quiet Platform," *Advances in the Astronautical Sciences*, Vol. 103, 1999, pp. 633-651.

[13] M. Nagashima and R. W. Longman, “Stability and Performance Analysis of Matched Basis Function Repetitive Control in the Frequency Domain,” *Advances in the Astronautical Sciences*, Vol. 119, 2005, pp. 1581-1612.

[14] B. Panomruttanarug and R. W. Longman, "Repetitive Controller Design Using Optimization in the Frequency Domain," *Proceedings of the 2004 AIAA/AAS Astrodynamics Specialist Conference*, Providence, RI, August 2004.

[15] B. Panomruttanarug and R. W. Longman, “Designing Optimized FIR Repetitive Controllers from Noisy Frequency Response Data," *Advances in the Astronautical Sciences*, Vol.127, 2007, pp. 1723-1742.

[16] B. Panomruttanarug and R. W. Longman, “Frequency Based Optimal Design of FIR Zero-Phase Filters and Compensators for Robust Repetitive Control,” *Advances in the Astronautical Sciences*, Vol.123, 2006, pp. 219-238.

[17] J. Bao and R. W. Longman, “Enhancing of Repetitive Control using Specialized FIR Zero-Phase Filter Designs,” *Advances in the Astronautical Sciences*, Vol. 129, 2008, pp. 1413-1432.

[18] W. Kang and R. W. Longman, “The Effect of Interpolation on Stability and Performance in Repetitive Control,” *Advances in the Astronautical Sciences*, Vol. 123, 2006, pp. 1163-1182.

[19] M. Yamada, Z. Riadh, and Y. Funahashi, “Design of Robust Repetitive Control System for Multiple Periods,” *Proceedings of the 39th IEEE Conference on Decision and Control*, 2000, pp. 3739-3744.

[20] M. Yamada, Z. Riadh, and Y. Funahashi, “Discrete-Time Repetitive Control Systems with Multiple Periods,” *Proceedings of 6th International Workshop on Advanced Motion Control*, 2000, pp. 228-233.

[21] R. W. Longman, J. W. Yeol, and Y. S. Ryu, “Improved Methods to Cancel Multiple Periodic Disturbances by Repetitive Control,” *Advances in the Astronautical Sciences*, Vol. 123, 2006, pp. 199-218.

[22] R. W. Longman, J. W. Yeol, and Y. S. Ryu, “Tuning and Performance of Robust Multiple Period-Repetitive Control,” *Advances in the Astronautical Sciences*, Vol. 124, 2006, pp. 687-705.

[23] M. Steinbuch, “Repetitive Control for Systems with Uncertain Period-Time.” Automatica. Vol. 38, No. 12, 2002, pp. 2103-2109.

[24] C.-P. Lo and R. W. Longman, "Root Locus Analysis of Higher Order Repetitive Control," *Advances in the Astronautical Sciences*, Vol. 120, 2005, pp. 2021-2040.

[25] C.-P. Lo and R. W. Longman, “Frequency Response Analysis of Higher Order Repetitive Control,” *Advances in the Astronautical Sciences*, Vol. 123, 2006, pp. 1183-1202.

[26] E. S. Ahn, R. W. Longman, and J. J. Kim, "Evaluating the Stability Robustness to Model Errors of Multiple-Period Repetitive Control," *Advances in the Astronautical Sciences*, Vol. 142, 2011, pp. 2581-2598.

[27] R. W. Longman and E. J. Solcz, "Small Gain Robustness Issues in the P-Integrator Repetitive Controller," *AIAA/AAS Astrodynamics Conference, A Collection of Technical Papers*, Part 2, Portland, Oregon, August 1990, pp. 537-551.

[28] E. S. Ahn, R. W. Longman, J. J. Kim, and B.N. Agrawal "Evaluation of Five Control Algorithms for Addressing CMG Induced Jitter on a Spacecraft Testbed," *Journal of Astronautical Sciences*. Under review

[29] P. LeVoci and R. W. Longman, "Frequency domain prediction of final error due to noise in learning and repetitive control," *Advances in the Astronautical Sciences*, Vol. 112, 2002, pp. 1341-1359.

[30] Y. Shi, R. W. Longman, and M. Nagashima, "Small Gain Stability Theory for Matched Basis Function Repetitive Control." *Proceedings of the First IAA Conference on Dynamics and Control of Space Systems*. Porto Portugal, March 2012, to appear in *Advances in the Astronautical Sciences*.

[31] R. S. Darling and M. Q. Phan, "Predictive Controllers for Simultaneous Tracking and Disturbance Rejection." *AIAA Guidance, Navigation, and Control Conference and Exhibit*. 16-19 August 2004, Providence, Rhode Island

[32] H.-J. Chen and R. W. Longman, "The Importance of Smooth Updates in Producing Good Error Levels in Repetitive Control," *Proceedings of the 38th IEEE Conference on Decision and Control,* Phoenix, AZ, 1999, pp. 258-263

[33] R. W. Longman and J. Bao, "On the Periodic Images of Start-up in Repetitive Control," *Advances in the Astronautical Sciences*, Vol. 127, 2007, pp. 1743-1762.

[34] S. G. Edwards, B. N. Agrawal, M. Q. Phan, and R. W. Longman, "Disturbance Identification and Rejection Experiments on an Ultra Quiet Platform," *Advances in the Astronautical Sciences*, Vol. 103, 1999, pp. 633-651.

[35] Jae J. Kim, Tim Sands, and Brij N. Agrawal, "Acquisition, Tracking, and Pointing Technology Development for Bifocal Relay Mirror Spacecraft." *Proc. of SPIE*. Vol. 6569, 656907-1, 2007.

[36] B. Agrawal, J. Kim, J.-W., and M. Romano, "Attitude Control and Determination of the NPS Bifocal Mirror Testbed," *presented at the 55th International Astronautical Conference*, Vancouver, Canada, October, 2004, IAC paper 04-A.4.09.

[37] M. Romano and B. N. Agrawal, "Acquisition, Tracking and Pointing Control of the Bifocal Relay Mirror Spacecraft," *Acta Astronautica*, Vol.53, No.4, 2003, pp. 509-519.

[38] B. N. Agrawal and C. Senenko, "Attitude Dynamics and Control of Bifocal Relay Mirror Spacecraft," *Advances in the Astronautical Sciences*, Vol. 109, Pt. 3, 2001, pp. 1703-1720.

[39] M. Romano and B. N. Agrawal, "Tracking and Pointing of Target by a Bifocal Relay Mirror Spacecraft, Using Attitude Control and Fast Steering Mirrors Tilting," *Proceedings of the AIAA Guidance, Navigation and Control Conference,* AIAA, Reston, VA, 2002

[40] B. N. Agrawal, M. Romano, and T. Martinez, "Three-Axis Attitude Control Simulator for Bifocal Relay Mirror Spacecraft," *Advances in the Astronautical Sciences*, Vol. 115, 2003, pp. 179-192.

[41] M. Nagashima and R. W. Longman, "The Effect of Averaging in Matched Basis Function in Real Time Repetitive Control," *Advances in the Astronautical Sciences*, Vol. 114, 2003, pp. 75-94.

[42] M. Nagashima and R. W. Longman, "Cancellation of Unknown Periodic Disturbances by PLL/Adaptive Matched Basis Function Repetitive Control," *Advances in the Astronautical Sciences*, Vol. 120, pp. 2041-2060.

[43] S. Haykin, Adaptive Filter Theory, Fourth Edition, *Prentice-Hall*, Upper Saddle River, New Jersey, 1985.

[44] K. W. Eure and J.-N. Juang, "Broadband Noise Control Using Predictive Techniques." *NASA Technical Memorandum* 110320. January 1997.

[45] R. W. Longman, J.-N. Juang, and M. Q. Phan, "On the Ill-Conditioning in MPC when used to Address the Repetitive Control Problem." *Proceedings of the AIAA/AAS Astrodynamics Specialist Conference*. Hawaii, August 2008.

[46] K. Chen, R.W. Longman, and M. Q. Phan, "On the Relationship Between Repetitive Control and Model Predictive Control," *Proceedings of the 2006 AIAA/AAS Astrodynamics Specialist Conference*, Keystone, CO, Aug. 2006.

[47] N. E. Goodzeit and M. Q. Phan, "System Identification in the Presence of Completely Unknown Periodic Disturbances." Journal of Guidance, Control, and Dynamics. Vol. 23, No. 2, 2000, pp. 251-259.

[48] M. Q. Phan, *Computed Basis Approach to Adaptive Tracking and Disturbance Rejection*. MAE Technical Report No. 3062, Department of Mechanical and Aerospace Engineering, Princeton University, July 1999.

[49] R. J. Watkins and B. N. Agrawal, "Use of Least Means Squares Filter in Control of Optical Beam Jitter." *Journal of Guidance, Control, and Dynamics*. Vol. 30, No. 4, July-August 2007.

[50] N. O. Perez Arancibia, N. Chen, J. S. Gibson, and T.-C. Tsao, "Adaptive control of jitter in laser beam pointing and tracking," in *SPIE Conference on Advanced Wavefront Control*, (San Diego, CA), SPIE, August 2006.

[51] M. D. Shuster and S.D. Oh, "Three-Axis Attitude Determination from Vector Observations." *J. Guidance and Control*. Vol. 4, No. 1, January-February 1981, pp. 70-77.

[52] Itzhack Y. Bar-Itzhack, "REQUEST: A Recursive QUEST Algorithm for Sequential Attitude Determination." *J. Guidance, Control, and Dynamics*. Vol. 19, No. 5, September-October 1996, pp. 1034-1038.

[53] Carl C. Liebe, "Accuracy Performance of Star Trackers – A Tutorial." *IEEE Transaction on Aerospace and Electronic Systems*. Vol. 38, No.2, April 2002, pp. 587-599.

[54] J. Tappe, J. Kim, A. Jordan, and B. Agrawal, "Star Tracker Attitude Estimation for an Indoor Ground-Based Spacecraft Simulator." *AIAA Guidance, Navigation, and Control Conference 2011*. Portland, OR, Vol. 1, pp. 1116-1122.

[55] J. N. Juang, L. G. Horta, and M. Phan, "System/Observer/Controller Identification Toolbox." *NASA Technical Memorandum* 107566, February 1992.

[56] B. Wie, "Space Vehicle Dynamics and Control." *AIAA Education Series.* 1998.

[57] E. S. Ahn, R. W. Longman, and J. J. Kim, "Comparison of Multiple-period and Higher Order Repetitive Control Used to Produce Robustness to Period Fluctuations," *Advances in the Astronautical Sciences*. To appear

[58] T. Stone, K. Freeman, R. Gilstrap, R. Hanel, P. Lencioni, J. Evanyo, and S. Burleigh "A Lunar Communication Satellite Network Architecture Employing Internet Protocol, Laser Communication Technologies and Small Satellites," *26th International Communications Satellite Systems Conference (ICSSC)*, San Diego, CA, June 2008

[59] E. S. Ahn, R. W. Longman, J. J. Kim, and B. N. Agrawal, "Improving Laser Communication between Formation Flying Satellites using Repetitive Control Jitter Mitigation," submitted to *Acta Astronautica* for journal publication.